The Dissertation Committee for Hrishikesh Vidyadhar Kelkar
certifies that this is the approved version of the following dissertation:

Towards the Creation of Fock States of Atoms

Committee:

Mark Raizen, Supervisor

Herbert Berk

Qian Niu

Charles Radin

Gennady Shvets

Towards the Creation of Fock States of Atoms

by

Hrishikesh Vidyadhar Kelkar, M.Sc.

DISSERTATION

Presented to the Faculty of the Graduate School of

The University of Texas at Austin

in Partial Fulfillment

of the Requirements

for the Degree of

DOCTOR OF PHILOSOPHY

THE UNIVERSITY OF TEXAS AT AUSTIN

August 2009

Dedicated to my parents Anupama and Vidyadhar Kelkar.

Acknowledgments

I would like to thank Mark Raizen for giving me the opportunity to work in his group. Mark is a great person to work with and is full of ideas. Every time he goes out of town, the whole lab is curious to know what new idea he is going to come back with. The atmosphere in the lab is very friendly and all my labmates deserve credit for that. I joined the lab in 2003 to work on the Sodium experiment. Robert Morgan helped me with machining during the first few weeks. Braulio Gutiérrez was the leader on that experiment and he had a many insights into physics and the practical implementation of solutions. We had innumerable discussion about physics, cooking, and more. Kevin Henderson was very helpful and patient in explaining things to me. His lab organization skills were excellent and have saved us a lot of time and energy over the years. Todd Meyrath worked on the Rubidium experiment but I learned a lot of electronics from him. We had a great time bowling on weekends and his spinning skills are very impressive. Florian Schreck was the postdoc in our lab who was extremely hard working and really a complete experimentalist. The control system for BEC experiments built together by Florian and Todd is very impressive and powerful. Chih Sung Chuu was the quietest person in the lab but his hard working nature was admirable. I was also helped by Jay Hanssen who was very methodical in his approach to solving problems.

The generation of students following me have been a valuable addition to the lab. I started work on the new Fock state setup with Tongcang Li and David Medellin. Tongcang has a lot of great (and sometimes as crazy!) ideas which were very helpful when we were trying to transport the BEC. David is extremely good at breaking down problems to their bare essentials and has a very good understanding of concepts. Soon after he joined the lab I have been trying to convince him (and I might have succeeded!) that he is actually a theorist. Kirsten joined our experiment as a Würzburg exchange student and later returned back and is now working full time on the experiment after hopping around on almost every experiment in the lab. She thinks like an experimentalist and is very solutions oriented.

Gabriel Price and Travis Bannerman worked together along with Kirsten on the single photon cooling experiment and I admire their focused and methodical approach. Adam Libson and Isaac Chavez started on the magnetic slower experiment and have worked very hard to get it to work in a short amount of time. Isaac is a big longhorn and a football fan and I probably know too much about football because of him (but I am still convinced that cricket is coming here in 20 years!). Adam has developed into a good bowler (though his spinning technique is the funniest and weirdest I have ever seen). Ed Narevicius joined as a postdoc on the slowing experiment and has some very good ideas and insights into problems. He was a big motivating force for their experiment and the lab in general. Tom Mazur is the latest addition to the lab on the slowing experiment. I found out only recently that he takes table tennis very personally. Melissa Jerkins and Charlotte Sanders are very

hardworking and friendly.

Max Riedel, Christian Parthy and Christoph Schaeff joined our lab as exchange students and were very enthusiastic and dedicated towards their projects. Julia Majors was a undergraduate student and responsible for hooking me to 'Atash', a Persian music band. Geneva White is a visiting undergraduate students who had many interesting stories to tell. Rob Clark joined us recently as a postdoc and I am sure he will be a valuable addition to the lab.

A number of people outside the lab were helpful in getting the experiment to its current stage. The physics machine shop deserves a lot of credit for their excellent work, especially, Allan Schroeder who is always ready to help with any mechanical and machining problems. Jack Clifford from the student shop is very friendly and I learnt most of my machining skills from him. I would also like to thank Jay Campbell for making the copper connectors and the phase masks and Richard Goodwin for modifying the science chamber. I would like to thank Sergio Muniz and Devang Naik from Chandra Raman's group in Georgia Institute of Technology. They provided useful information about the optically plugged trapped that helped us achieve a BEC in our setup.

I have been lucky to have the support and help of many friends including Dagim, Yafis, Sarp, Andy, Nacho, Paul, Spencer, Levent, Massimo, the rest of the Jabronis, Jenny and Antonia. I had a great time with them playing soccer, watching movies, bar hopping on 6th street and numerous sausage fests.

I would also like to thank Namrata, Apoorwa and my brother Mayuresh for keeping me connected to the real world (at times on a daily basis!).

I would like to thank Olga Vera and Elena Simmons for their administrative help and smooth processing of purchases. I would like to thank Norma Kotz for her help during the early days of graduate school that made me comfortable in a new country and the new system.

Towards the Creation of Fock States of Atoms

Publication No. _____

Hrishikesh Vidyadhar Kelkar, Ph.D.
The University of Texas at Austin, 2009

Supervisor: Mark Raizen

Ultracold atoms have been successfully used to study numerous systems, previously unaccessible, but a precise control over the atom number of the sample still remains a challenge. This dissertation describes our progress towards achieving Fock states of atoms.

The first three chapters cover the basic physics necessary to understand the techniques we use in our lab to manipulate atoms. We then summarize our experimental results from an earlier setup where we did two experiments. In the first experiment we compare the transport of cold atoms and a Bose Einstein Condensate (BEC) in a periodic potential. We find a critical potential height beyond which the condensate behavior deviates significantly from that of thermal atoms. In the second experiment we study the effect of periodic temporal kicks by a spatially periodic potential on a BEC in a quasi one dimensional trap. We observe a limit on the energy that the system can absorb from the kicks, which we conclude is due to the finite height of the trap rather than quantum effects.

The majority of the dissertation discusses our experimental setup designed to produce Fock states. The setup is designed to use the method of laser culling to produce Fock states. We are able to create a BEC and transport it into a glass cell 25 cm away. We tried different innovative methods to reduce vibrations during transport before finally settling to a commercial air bearing translation stage. We create a high confinement one dimensional optical trap using the Hermite Gaussian TEM_{01} mode of a laser beam. Such a trap gives trapping frequencies comparable to an optical lattice and allows us to create a single one dimensional trap. We creating the TEM_{01} mode using an appropriate phase object (phase plate) in the path of a TEM_{00} mode beam. The method for producing the phase plate was very well controlled to obtain a good quality mode. Once the atoms are loaded into this one dimensional trap we can proceed to do laser culling to observe Sub-Poissonian number statistics and eventually create Fock states of few atoms.

Finally, we describe a novel method to create a real time tunable optical lattice which would provide us with the ability of spatially resolved single atom detection.

Table of Contents

List of Tables

List of Figures

Chapter 1

Introduction

This thesis describes a scientist's adventures in the field of experimental atomic physics. The fact that light has an effect on particles (atoms) has been known for a long time. The advent of the laser allowed an unprecedented control over this interaction. Rather than study effects of this interaction, we could use this interaction to produce a desired effect. One example of such a process is laser cooling where the control over this interaction allows us to slow an atom using a laser beam (down to tens of micorkelvin). Cold atoms produced with this method have been used to study phenomenon that were previously not observable, especially, the ones predicted in condensed matter systems. Going to low temperatures prevents thermal fluctuations from washing out the interesting quantum mechanical behavior of atoms. Producing a Bose Einstein Condensate requires one to go even lower in temperature.

The various techniques (including laser cooling) used to create low temperatures are probabilistic in nature. This means there are huge fluctuations (typically 10%) in the final number of cold atoms obtained from one experimental run to another. This drawback prevents us from accessing a whole host of systems (and problems) that demand much more. This becomes obvious when we think of a simple problem like: *Can we create precisely N atoms in*

the ground state of a trap with 100% certainty every time we run the experimental sequence? where, N can be any number of our choice (this is also the definition of a N atom Fock state). Currently, the answer to this question is *no*. Having an affirmative answer to such a question is extremely crucial in experiments that hope to implement a quantum computation algorithm, for example. The initial state fidelity requirement for most quantum computation schemes is very severe. Apart from that, interaction between few atoms and few particle entanglement are interesting problems in themselves. So is the problem of atom number statistics in different atomic systems.

This thesis describes our efforts towards coming up with an affirmative answer to the above question at least for small values of N (N=1,2,3,...). The thesis is organized as follows:

- Chapters 2 reviews the interactions of an atom with external magnetic and electromagnetic fields. These interactions are used to produce cold atomic samples and manipulate them.

- Chapter 3 describes the basic steps to cool atoms and produce a BEC. The chapter is non technical and emphasizes the physical principles rather than mathematical rigor.

- Chapter 4 describes the experiments done with our first setup. This is a summary of results published in [1] and [2].

- Chapter 5 provides motivation for building our second setup which is designed to create Fock states.

- Chapter 6 describes the second experimental setup in extensive detail. It describes many experimental failures and successes and ends with the current status, en route to creating Fock states.

- Chapter 7 describes a novel method to produce a dynamically variable optical lattice with high mechanical stability. This is a summary of results published in [3].

The following publication have resulted so far from the work mentioned in this thesis:

1. "*Experimental Study of the Role of Atomic Interactions on Quantum Transport.*" K.C. Henderson, H. Kelkar, B. Gutierrez-Medina, T. Li, and M.G. Raizen. Phys. Rev. Lett. **96**, 150401 (2006).

2. "*A Bose-Einstein Condensate Driven by a Kicked Rotor in a Finite Box.*" K.C. Henderson, H. Kelkar, T.C. Li, B. Gutierrez-Medina, and M.G. Raizen. Europhys. Lett. **75**, 392 (2006).

3. "*Real-Time Control of the Periodicity of a Standing Wave: an Optical Accordion.*" T.C. Li, H. Kelkar, D. Medellin, and M.G. Raizen. Optics Express. **16**, 5465 (2008).

Chapter 2

Interaction of atoms with external fields

Atoms can be manipulated using external electric and magnetic fields. This chapter describes these interactions and the way they can be used to manipulate atoms.

2.1 Interaction of atoms with light

Consider a two level atom at rest in the presence of a laser field. The atom responds to the laser light in two ways. The atom absorbs the light if its frequency is close to the resonance frequency. If the frequency is far from resonance, the absorption is negligible but the atom still *feels* the presence of the electromagnetic field which is manifest by a shift in its energy levels[1]. In general, both these processes happen at the same time with different strength.

2.1.1 Near resonant light

If the laser frequency is near resonance the atom absorbs a photon and makes a transition to the excited state. Since the excited state has a finite lifetime, the atom decays back to the ground state by emitting a photon. It is

[1] An atom whose transition frequency is close to the laser frequency acts like an amplitude object (absorption dominated) for light. If its transition frequency is far from the laser frequency it acts acts like a phase object (dispersion dominated).

then ready to absorb another photon. The rate at which it scatters photons depends on the intensity of light, the detuning of laser from the resonance frequency and the lifetime of the excited state. The expression for the scattering rate is [4]:

$$R_s = \frac{s_0\Gamma/2}{1 + s_0 + 4\Delta^2/\Gamma^2} \tag{2.1}$$

Here, Γ is the natural linewidth of the transition, $\Delta = \omega_L - \omega_0$ is the laser detuning from the resonance frequency and $s_0 = I/I_s$ is the on resonance saturation parameter where I is the laser intensity and I_s is the saturation intensity. The saturation intensity is defined as:

$$I_s = \frac{\pi hc\Gamma}{3\lambda^3} \tag{2.2}$$

λ being the resonant wavelength. The saturation intensity for the Sodium D2 line is 6.3 mW/cm^2. From De Broglie's relation we know that a photon carries momentum equal to $p = h/\lambda$. During the process of absorption and emission there is a direct transfer of momentum between the atom and photons. Multiplying the scattering rate by the momentum carried by each photon gives us the radiation force on the atom:

$$F_{scatter} = R_s\frac{h}{\lambda} \tag{2.3}$$

This expression gives the momentum transferred during absorption. It is easy to see that this scattering force is not a conservative force since it depends on detuning Δ which in turn depends on the velocity of the atom via Doppler effect. If arranged cleverly, it can be used to slow down an atom. This is the principle of laser cooling. The Zeeman slower and the Magneto Optical Trap both rely on this principle.

2.1.2 Far detuned light

If the laser frequency is far from resonance the interaction can be modeled as one in which the electric field of the laser induces an electric dipole moment in the atom. The potential energy of this induced dipole in turn depends on the electric field and is given by:

$$H = -\mathbf{p} \cdot \mathbf{E} \tag{2.4}$$

where $\mathbf{p}$ is the polarization induced in the atom. This potential energy is the amount by which the energy levels shift in the atom. This shift is called the *ac Stark shift* or *light shift*. The induced dipole depends on the state of the atom and thus the ac Stark shift is different for different electronic states. The ac electric field of the laser is oscillating at a very high rate and is seen by the atom only as a time averaged electric field. For such a time averaged oscillating field, the potential energy of the dipole becomes:

$$H = -\frac{1}{2}\alpha\langle E^2\rangle \tag{2.5}$$

where α is the polarizability of the atom. The calculation of α is generally not a trivial task for multilevel atoms. For a two level atom the expression for the light shift in terms of experimentally measurable parameters is[5]:

$$U = \frac{\hbar\Gamma^2}{8}\frac{I}{I_s}\left[\frac{1}{\omega_L - \omega_0} - \frac{1}{\omega_L + \omega_0}\right] \tag{2.6}$$

The light shift depends on the detuning which implies that it can be positive or negative depending on whether the laser frequency is above or below the atomic resonance frequency. For frequencies above resonance (blue detuning) the light shift is positive which means the potential energy of the atom increases with the intensity of light. If the frequency is below resonance (red detuned) the light shift is negative meaning the energy of the atom decreases with intensity. This effect can be used to spatially trap an atom using a far red detuned laser beam that has a Gaussian intensity profile. It should be noted that though the laser frequency is far away from resonance, there can still be scattering of photons according to Eq. 2.1. For such a far detuned laser, the scattering rate is inversely proportional to the detuning and directly proportional to the peak intensity of the laser beam.

2.2 Interaction with a static magnetic field

We will now consider the case of an atom in a static magnetic field. If the atom has a permanent magnetic dipole moment $\boldsymbol{\mu}$ (paramagnetic atom) then its potential energy in the presence of a magnetic field $\mathbf{B}$ is given by

$$H = -\boldsymbol{\mu} \cdot \mathbf{B} \tag{2.7}$$

$\boldsymbol{\mu}$ depends on the internal Zeeman state of the atom. The energy in terms of this internal state is given by:

$$H = m_F g_F \mu_B |\mathbf{B}| \tag{2.8}$$

where m_F is the magnetic quantum number of the state, g_F is the Lande g factor and μ_B is the Bohr magneton. A sodium atom in the $|F = 1, m_F = -1\rangle$

state has $g_F = -1/2$ and the energy shift (divided by Planck's constant) as a function of the magnetic field is 0.7 MHz/Gauss. The corresponding force on the atom is given by:

$$\mathbf{F}_{mag} = -m_F g_F \mu_B \boldsymbol{\nabla} |\mathbf{B}| \tag{2.9}$$

If the magnetic moment is positive the potential energy increases with higher magnetic field. Such states are called *low field seekers*. If the magnetic moment is negative, the potential energy decreases with higher magnetic field. These states are called *high field seekers*. The magnetic interaction can be used to trap atoms in a magnetic field that has a local extremum in space. According to Wing's theorem [6], a local maximum in the magnitude of the magnetic field cannot exist in a source free region. Hence, only low field seeking states can be trapped using purely magnetic fields. We should note that we require a minimum in the *magnitude* of the magnetic field since the atoms will follow the field if the adiabaticity condition is satisfied (as discussed in the subsection). A quadrupole magnetic field that has a zero at the center and increases linearly in all directions is one configuration that can be used to trap atoms. However, the zero in the magnetic field at the center can cause serious problems for trapping very cold atoms as will be shown in the subsection. A Ioffee-Pritchard kind of trap is one that has a local non zero minimum in the magnetic field. These traps are very popular since they provide a harmonic confinement with a non zero field minimum allowing atoms of arbitrarily small temperatures to be trapped. A cloverleaf trap and the QUIC trap are two examples of traps that belong to the Ioffe-Pritchard category. It should be

mentioned that equation 2.8 is true only for low magnetic fields where F is a good quantum number. At high magnetic fields (in the regime of Paschen-Back effect) the energies behave differently with magnetic field.

2.2.1 Adiabaticity condition

In deriving the formulae in this section we assumed that $\boldsymbol{\mu}$ and $\mathbf{B}$ always point in the same direction and hence the potential and force depend only on the magnitude of $\mathbf{B}$. This is true only if the magnetic moment is able to follow the changing magnetic field adiabatically. The magnetic field of the trap is inhomogeneous in space. As the atom moves in the magnetic trap it sees a time varying magnetic field which can induce transitions in the internal state of the atom. To adiabatically follow the field (and avoid these transitions), the rate of change of the angle of the magnetic field should be much smaller than the Larmor precision frequency of the atom. This condition is derived from the idea that if an atom precesses enough times at each value of the magnetic field it is able to follow the field.

$$\omega_L = \frac{\mu|\mathbf{B}|}{\hbar} \gg \frac{d\theta}{dt} = \frac{\boldsymbol{\nabla}|\mathbf{B}|}{|\mathbf{B}|} \cdot \mathbf{v} \tag{2.10}$$

This gives the condition for adiabaticity as:

$$\frac{\hbar}{\mu} \frac{\boldsymbol{\nabla}|\mathbf{B}|}{|\mathbf{B}|^2} \cdot \mathbf{v} \ll 1 \tag{2.11}$$

Here $\mathbf{v}$ is the velocity of the atom and μ is the magnetic moment of the atom. From this equation it is easy to see that if the atom goes through a region where the magnetic field is zero the adiabaticity condition is never

satisfied and it induces a change in the internal state which typically results in the atom being ejected out of the trap. Such losses prevent the use of a purely quadrupole trap to create a Bose Einstein Condensate, where the temperature of the atoms is hundreds of nanokelvin and they all crowd around the central minimum where the magnetic field is zero. However, there is a way to prevent the atoms from going near the zero field region using the repulsive dipole potential created by a blue detuned laser beam.

Chapter 3

Creating a Bose Einstein Condensate

In this chapter we will review some basic techniques used in creating a Bose Einstein Condensate(BEC). These techniques have been developed over many years by a number of groups around the world. The efforts resulted in the creation of a degenerate Bose gas in 1995 [7], a degenerate Fermi gas in 1999 [8] and the Fermionic molecular condensate gas in 2003 [9]. The technical details and specifics of implementation are deferred to later chapters where we will understand our system in greater detail. This chapter focuses on highlighting the basic physical principles.

3.1 Basics of laser cooling

Consider a two level atom moving with a velocity v towards a laser beam of frequency ν. The frequency of light as seen by the atom is Doppler shifted to

$$\nu' = (1 - \frac{v}{c})\nu \tag{3.1}$$

where c is the velocity of light. If the frequency of light is such that $h\nu' = \Delta E_{eg}$, where ΔE_{eg} is the energy difference between the ground and the excited states, then a photon will be absorbed by the atom. Since the photon carries a momentum $p = h/\lambda$, this reduces the velocity of the atom by an

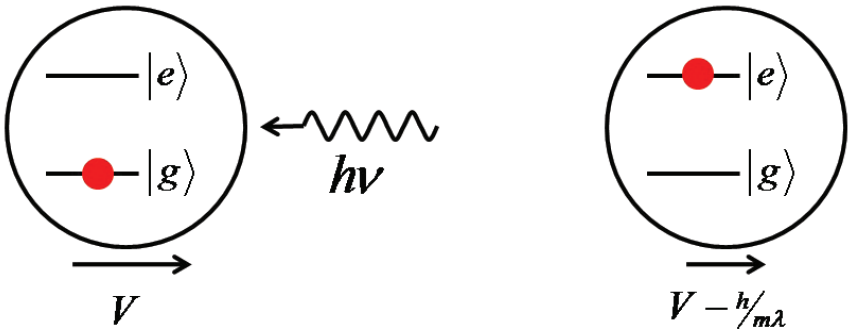

Figure 3.1: Illustration of laser cooling.

amount $\Delta v = h/(\lambda m)$ along the direction of the beam, where m is the mass of the atom.

We have thus managed to reduce the velocity of the atom but at the cost of putting the atom in the excited state. Since the excited state has a finite lifetime, the atom eventually falls back to the ground state and emits a photon and recoils by a momentum equal to the momentum of the emitted photon. If this process is allowed to happen a number of times, the total momentum imparted to the atom due to the spontaneously emitted photons averages to zero since the spontaneously emitted photons have no preferred directionality. The momentum kick due to the absorbed photons, however, is always in the direction of the laser beam. The atom is thus slowed along that direction while it performs a random walk in the transverse plane due to the random kicks from the spontaneously emitted photons. This is the basic principle of laser cooling where there is a direct exchange of momentum between photons and atoms giving rise to the so called 'radiation force'. It is important to understand the distinction between this force and other forces

(say due to a magnetic field). Radiation force depends on the Doppler shift and hence it acts only on those atoms that are traveling towards the laser beam at the specific velocity. A different velocity group of atoms can be targeted by changing the frequency of the laser beam.

3.2 The oven

If the element we would like to capture and cool happens to be a gas, it is easy to since we already have individual atoms. However, if the element is solid or liquid, then we have to rely on its vapor pressure to capture it in gas form. At room temperature, the vapor pressure of Rubidium (Rb) is high but Lithium (Li) and Sodium (Na) have a very tiny vapor pressure resulting in a very small number of gaseous atoms. Consequently, one needs to heat up these elements to get a higher yield. The common procedure is to heat them in an enclosed oven with a small aperture from which the vapor can escape. There are many oven designs currently in use, each one with its own advantages. Our oven can hold 15 grams of sodium and last for 700 hours whereas there are other designs that run on less than a gram a year [10]. There are other alternatives to ovens like a getter source [11] or light induced atomic desorption (LIAD) [12] which can be used to generate the gas. These are used primarily for Rubidium.

3.3 Zeeman Slower

Radiation pressure from a laser beam can be used to slow down a beam of atoms. However, as the atoms slow down the Doppler shift is no longer sufficient to keep the light in resonance with the atomic transition. To correct for this a spatially dependent magnetic field can be applied that uses the Zeeman effect to adjust the transition frequency so that a certain velocity group of atoms stays in resonance with the incoming light as they slow down. This arrangement is called a Zeeman slower and was developed in 1982[13]. Alternatively, one could ramp the laser frequency to constantly keep the light in resonance with a certain velocity group of atoms as they slow down. This method is called chirped cooling and was demonstrated in 1984[14]. One could use an electric field to shift the energy levels too. Such a slower is called Stark decelerator [15]. Zeeman slower is the most popular of all these techniques. Fig. 6.7 shows a typical magnetic field profile of a Zeeman slower.

3.4 MOT

The atoms exit the Zeeman slower with slow enough velocity to be captured in a Magneto Optical Trap (MOT). A MOT consists of 3 pairs of counter propagating laser beams aligned orthogonal to each other with specific polarizations in addition to a quadrupole magnetic field. Without the magnetic field, the configuration is called an optical molasses where the atoms are cooled in all directions. However, it does not act like a trap with a minimum in potential energy. The zero of the quadrupole field provides this minimum where

the radiation force from each set of counter propagating beams is balanced. The laser frequency in a MOT is red detuned from the atomic transition. An atom moving away from the center experiences a Doppler shift and also a Zeeman shift of its energy levels due to the increasing magnetic field. This causes the atom to absorb preferentially from one beam creating an imbalance in the radiation pressure. This forces the atom back towards the center of the MOT. A MOT acts like a dissipative trap because this restoring force depends on the the velocity dependent Doppler shift. The dissipative nature of the trap is what cools the atoms (not just trap them). This force is analogous to the frictional force which is also dissipative and velocity dependent. The typical temperature in a MOT is 100's of micro Kelvin. This low temperature has prompted a number of interesting experiments that have explored the quantum nature of atoms. It is important to note that the force in a MOT comes from light and the magnetic field merely acts like a knob to tune this force.

A MOT cannot be used to cool atoms to arbitrarily small temperatures because the cooling transition has a finite linewidth. In our discussion thus far, we assumed that the energy of the absorbed photon and the emitted photon (and hence the momentum kick in either case) is the same. However, there is a finite uncertainty in the excited state energy which can cause the emitted photon to be at a different energy than the absorbed one. The energy difference makes the momentum kick due to absorption and emission to be different. As a result, there is always an uncertainty in the final kinetic energy of the atom equal to the uncertainty in the excited state energy. The atom cannot be cooled any further. This limit is called the Doppler limit whose

value for sodium is 250 μK. There are tricks to avoid the Doppler limit and cool the atom further [16].

Another limit to laser cooling is the recoil limit where the lowest velocity an atom can attain is equal to the recoil velocity. Consider an atom moving with just enough velocity so that when it absorbs one more photon in the correct direction, it comes to rest. When this happens, the atom does come to rest but it is in the excited state. It decays to the ground state by emitting a photon. This gives a recoil kick to the atom and it starts moving again with the recoil velocity. The velocity of this atom cannot be reduced further (but of course, there are other techniques that can be used to reduce the velocity even further [17, 18]).

The phase space density of atoms in a MOT (typically 10^{-6}) is still orders of magnitude smaller than what is necessary to create a BEC. To go even lower in temperature (and higher in phase space density) a different method of cooling, called evaporative cooling, is used. Near resonant light, which helped in cooling so far, now acts as a source of heating since we want to go to temperatures below its limit. Thus all near resonant light must be turned off before further cooling .

3.5 Magnetic Trap

The atoms cooled in a MOT are loaded in a conservative trap usually created by a magnetic field, a far detuned optical field or a combination of both. If the atom has a permanent magnetic dipole moment, its motion can

be controlled using a magnetic field. In particular, one can create a trap for paramagnetic atoms by creating an inhomogeneous magnetic field that has a non zero minimum in the magnitude of the field. Such a trap, called the Ioffe-Pritchard trap, is a conservative trap for atoms if the magnetic field gradient is not very large (as discussed in section 2.2.1). If the temperature of atoms loaded into the magnetic trap is small, we can approximate the trapping potential by a 3D harmonic potential. By very nature of the harmonic trap, there is a correlation between the energy of the particle and the amplitude of oscillation. Atoms that have higher energy go further away from the center and see a higher magnetic field.

3.6 Evaporative cooling

Evaporative cooling relies on the fact that, in equilibrium, the gas has a wide distribution of velocities. The width of the distribution depends on the temperature. If the high velocity tail of the distribution is truncated, and the rest of the gas is allowed to reach equilibrium, then the average energy per atom will be smaller. Consequently, the gas will be cooler and more dense. One loses atoms in this process but the resulting gas has a higher phase space density. The initial velocity distribution of atoms in a magnetic trap is close to a Boltzmann distribution (it cannot be an exact Boltzmann distribution since the the very high velocity group of atoms cannot be trapped). To evaporatively cool the gas, we selectively flip the spin of the atoms that reach the highest magnetic field and eject them out of the trap. The remaining gas is then allowed to re-thermalize and reach a lower temperature. This process can be

repeated as many times as necessary to reach a phase space density above unity where the gas undergoes a phase transition to a BEC.

3.7 Bose Einstein Condensate

Imagine atoms at finite temperature held in a harmonic trap. The atoms fill the different energy eigenstates of the trap according to the Boltzmann distribution. For high temperatures, the population in the ground eigenstate of the trap is negligible compared to the total number of atoms. As we start evaporatively cooling the atoms, more and more atoms from the higher energy levels move to lower ones. If we keep cooling, the atoms eventually start filling up the ground state of the trap substantially. This is the onset of the phase transition to a BEC. Close to absolute zero, almost all the atoms will occupy the ground state.

An important concept in this process is the idea of cooling itself. Cooling is generally referred to reduction in temperature. A more correct definition for cooling would be *increase in phase space density*. For example, adiabatic expansion of a gas reduces its temperature but does not increase the phase space density. From a quantum mechanical point of view, an adiabatic process is one in which the the population of different eigenstates of the trap remains the same after the process. If we start with a trap holding atoms and adiabatically expand it, the energy levels will start moving closer during expansion, hence reducing the temperature. But since the process is adiabatic, the population in the different energy levels remains the same and we

can never create a BEC this way even though the temperature can be made arbitrarily small. Thermodynamically speaking, we cannot produce a BEC simply by adiabatic expansion because it conserves phase space.

The phase transition to a BEC occurs when the phase space density is greater than unity. This also corresponds to some critical temperature but it is not an absolute value. The critical temperature depends on a number of parameters including the number of atoms in the trap.

An important characteristic of a BEC is increased interaction among the atoms. This interaction can substantially change the behavior of the gas and is useful in providing detectable signatures of a BEC.

3.8 Detection

Light passing through a cloud of atoms gets absorbed if the frequency of light is close to an atomic transition. This absorption can be measured to detect the presence of atoms. A common way to detect atoms is to use absorption imaging where a laser beam travels though a cloud of atoms and the cloud is imaged onto a CCD camera. If there are atoms present, they absorb light from the beam and cast a shadow on the CCD. By measuring the contrast of this shadow the density of atoms can me deduced. The spatial extent of the shadow corresponds to the spatial size of the cloud.

For the image to produce a measurable contrast, each atom must absorb multiple photons from the beam. These multiple absorptions and emissions give momentum kicks to the atoms that heats them up and destroys their

state in the external trapping potential. This is thus a destructive imaging. If the frequency of the laser beam is far detuned from the atomic transition then the atoms do not absorb light. The laser beam sees the atomic cloud as a dispersive medium that induces a phase difference in the part of the beam that goes though the cloud. This phase difference can be measure by interfering it with a reference beam. This kind of imaging is called phase contrast imaging. This detection does not rely on absorption and hence does not destroy the state of the atoms in the external potential.

Both the above mentioned techniques are good only for clouds with a large number of atoms. They are not sensitive to detect a single atom, for example. To detect single atoms, one can use fluorescence imaging that relies on spontaneous scattering or cavity detection that relies on dispersion.

In fluorescence imaging, a single atom scatters many photons. These photons can be collected with a lens and counted with an avalanche photodiode. For small atom numbers, the rate of scattered photons scales linearly with number of atoms. One can thus see quantized steps in fluorescence level. The step size corresponds to the scatter rate due to each atom. Single atoms can also be detected by measuring the dispersion. The dispersion caused due to a single atom is too small to be measured directly. But the laser beam can be made to pass through the atom a number of times by putting a cavity around the atom that confines the laser beam. The dispersion due to the atom is now amplified by the number of round trips that the beam can make inside the cavity before it is leaks out of the cavity. If this total dispersion is large

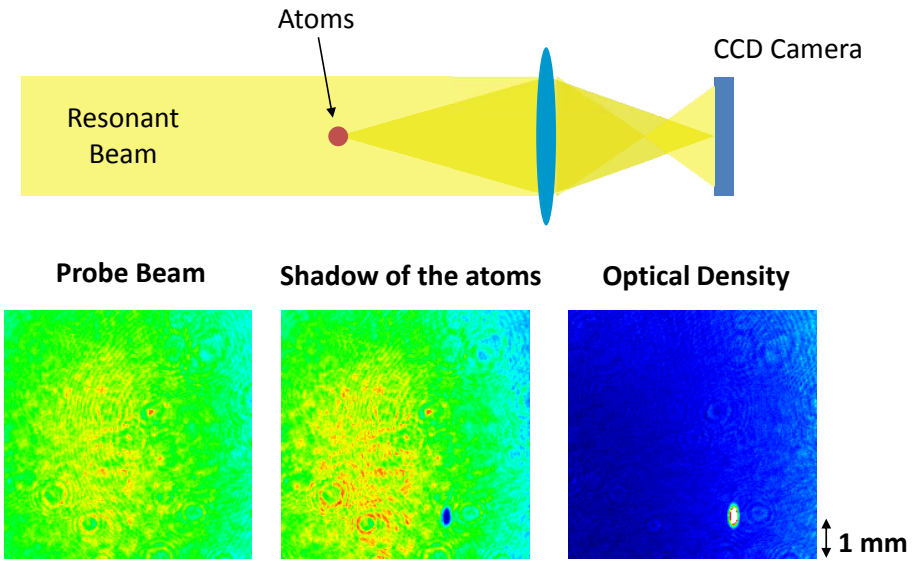

Figure 3.2: Absorption imaging.

enough to alter the resonance condition of the cavity then one can see sharp peaks in transmission corresponding to the presence of a single atom inside the cavity [19]. In our experiments we rely on absorption imaging to measure large atom numbers and fluorescence imaging for few atoms.

Chapter 4

Experimental Setup 1

I joined the group at a stage when we were working towards creating our first sodium BEC, which we did in November 2003. The first goal of the experiment was to transport transport a BEC vertically using a blue detuned optical lattice. Details about our efforts can be found in [20]. The next set of experiments was to study the behavior of atoms confined in a quasi 1D magnetic waveguide. The first experiment was to study the effect of interactions on quantum transport [1]. The second experiment was to study a kicked rotor of interacting atoms [2]. Both these experiment have been explained in great detail in the PhD thesis of Kevin Henderson [21]. Here I will present a brief summary of those results.

4.1 Theory of quantum transport in a periodic potential

A basic problem in condensed matter physics is to study the motion of an electron in a crystal. The problem is modeled as an electron moving in a periodic potential created by the lattice ions. The solution to the corresponding Schrodinger's equation gives the wavefunction and allowed energies of the electron. A similar problem can be constructed in the context of cold atoms by allowing an atom to move in a periodic potential created by an optical lat-

tice (a review of this problem and experimentally observed phenomenon can be found in [22–24]). In the absence of external forces, the time independent Schroedinger equation for the atom is:

$$\left[-\frac{\hbar^2}{2m}\frac{\partial^2}{\partial z^2} + \frac{V_0}{2}\cos(2k_L z)\right]\psi(z) = E\psi(z) \tag{4.1}$$

Here, V_0 is the well depth of the lattice, $k_L = \frac{2\pi}{\lambda_L}$ where, λ_L is the laser wavelength. This equation can be solved using Bloch's theorem which says that the wavefunction of a particle in a periodic potential can be written as a periodically modulated plane wave where the modulating function has the same period as the lattice. The wavefunction thus has a form:

$$\psi(z) = e^{ikz}u_{n,k}(z) \tag{4.2}$$

$u_{n,k}(z)$ is the modulating function with the property that $u_{n,k}(z) = u_{n,k}(z+d)$ where d is the lattice period. k and n are quantum numbers that arise due to the boundary conditions. k is the quasimomentum and n is the band index. Solving the equation for energy gives the famous band structure, only this time it is for atoms in an optical lattice. The solutions are Mathieu functions whose values can be obtained in Mathematica or most handbooks on mathematical functions [25]. Specifying the values of n and k, completely specifies the energy of the atom. It is interesting to note that in Newtonian mechanics, we calculate the velocity of an object, given the external force, and then its energy. In quantum mechanics, we solve the Schroedinger equation that directly gives the energy, or more precisely, the dispersion relation (E vs k). The group velocity v_g and the effective mass m_{eff} can be computed by

taking derivatives of the dispersion relation:

$$v_g(k) = \frac{1}{\hbar}\frac{\partial E}{\partial k}, \;\; m_{eff}(k) = \hbar^2 \left[\frac{\partial^2 E}{\partial k^2}\right]^{-1} \tag{4.3}$$

The band structure for typical experimental parameters is shown in Fig. 4.1. The conventional energy scale in this problem is recoil energy which is the kinetic energy gained by an atom if it absorbs a photon from the lattice beam. For a lattice created by retroreflecting a 532 nm laser beam, the recoil energy is $E_r = h^2/2m\lambda^2 = h\times 30.6$ KHz.

Our system is not an atom but an ensemble of atoms at finite temperature. The problem we would like to study is: *How does an atomic ensemble evolve in a periodic potential?* We would like to compare the results for thermal atoms with those for a Bose Einstein Condensate. This comparison would allow us to study the effects of interactions on quantum transport. To study the evolution, we need to know the behavior of group velocity in the band (v_g vs k). The group velocity of atoms in the lowest band is plotted in Fig. 4.2. Ultracold thermal atoms and BEC, both occupy only the lowest band (partially or completely) due to their low temperature. If the ensemble occupies a region very close to the center of the band, the group velocity behaves linearly which is similar to free space expansion. An initial Gaussian density distribution would retain its Gaussian nature as it expands in width. However, if the ensemble occupies a larger portion of the lowest band, it encounters a maximum group velocity resulting in the Gaussian wavepacket being distorted after evolution.

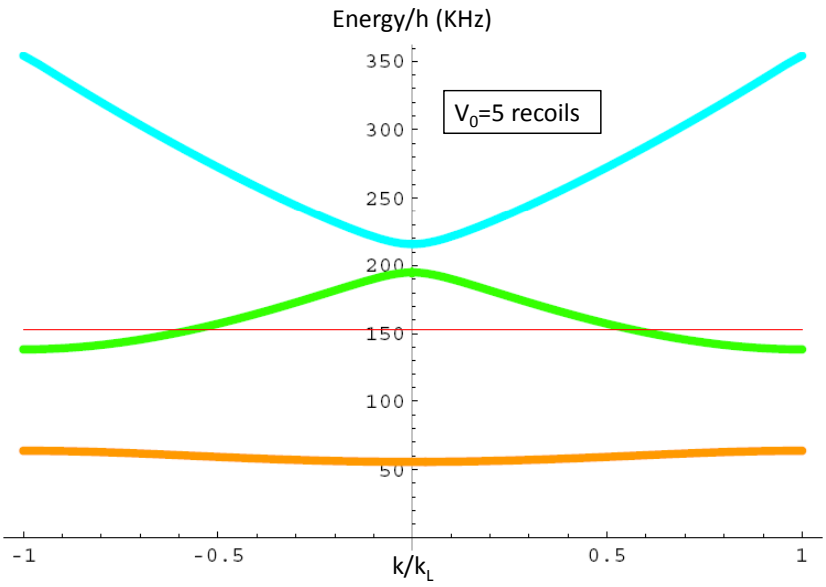

Figure 4.1: The plot shows the band structure for atoms in an optical lattice. The red line is the optical lattice depth. The lattice depth is 5 recoils corresponding to about 150 KHz. This is a reduced zone picture where all higher Brillouin zones are mapped on to the lowest one.

4.2 Quantum transport experiment

A ^{23}Na BEC is created by evaporatively cooling atoms in a cloverleaf magnetic trap [26]. The trapping frequencies in this trap are $\omega_{\perp}= 2\pi$ 324 Hz and $\omega_z= 2\pi$ 20 Hz. The trap is slowly transformed into a quasi 1D magnetic waveguide by turning off the curvature coils of the cloverleaf trap. The waveguide is flat with a trapping frequency of ω_z=0.8 Hz along its axis. The schematic for the experimental setup is shown in Fig. 4.3. A BEC of 2×10^6 atoms is loaded into the waveguide and held in a hybrid trap created by the waveguide (for transverse confinement) and an optical tweezer (for axial con-

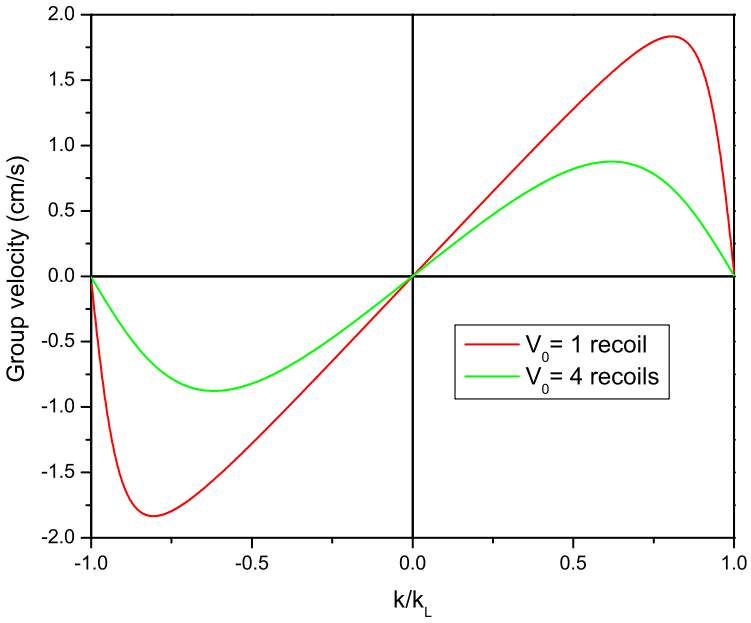

Figure 4.2: Group velocity in the lowest band of an optical lattice for two different lattice depths. λ= 532 nm and the lattice depth is 1 E_r(red) and 4 E_r(green).

finement). The optical tweezer has a wavelength of 1064 nm generated by a fiber laser [IPG photonics, Model: YLD-10-1064], carrying 6.35 W and focused to a $1/e^2$ radius of 180 μm. The trap frequencies in the hybrid trap are $\omega_\perp = 2\pi$ 317 Hz and $\omega_z = 2\pi$ 75 Hz. The periodic potential is created by a far detuned beam (λ=532 nm) which is retro reflected to create an optical lattice. The waist of the beam at the atoms is 120 μm and the power can be changed to vary the lattice depth as high as 18 E_r. Fig. 4.4 shows this ballistic expansion for two different well depths for both BEC and thermal atoms. The rate of

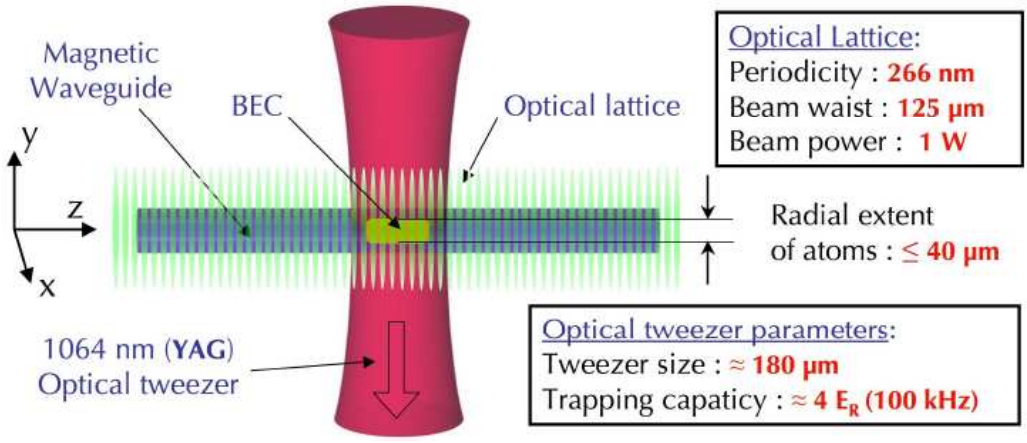

Figure 4.3: Setup to study 1D transport. Graphics rendered by Kevin Henderson.

expansion in the lattice was found to be linear (ballistic) in both cases. The cloud size in the plot is the root mean square value of the measured density distribution. The slope of the line gives the rate of expansion. The rate of expansion for different lattice depths is shown in Fig. 4.5(a). The red data points are for thermal atoms while the blue ones are for BEC. The solid lines are predictions using single particle theory as discussed below.

Assuming a Gaussian distribution in space z (in the tweezer) and quasi momentum k (which also assumes that the momentum of atoms in the tweezer maps into the initial quasi momentum with the lattice turned on), the initial phase space distribution of atoms is given by:

$$f(z, v, t = 0)dvdz = N\frac{\hbar\omega_z}{2\pi k_B T}e^{-m\omega_z^2 z^2/(2k_B T)}e^{-\hbar^2 k^2/(2mk_B T)}\,dkdz \qquad (4.4)$$

where $\omega_z = 75$ Hz is the trapping frequency due to the tweezer and T is the

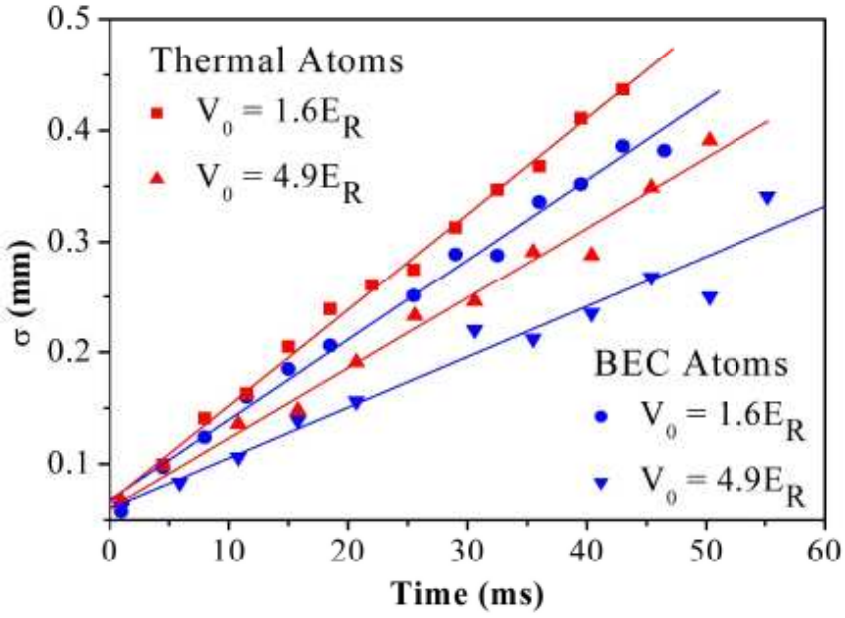

Figure 4.4: Ballistic expansion in a periodic potential.

temperature of atoms (which can be deduced from free expansion in the waveguide). The tweezer is turned off and atoms are allowed to expand. The experimentally measured parameter is the evolution of density distribution in space. This distribution at time t is given by $f(z,t) = \int_{-\infty}^{\infty} f(z - v_k, v, t = 0)\, dvdz$, where v_k is the group velocity of atoms at quasi momentum k and is derived from the band structure. This model assumes that the velocity distribution does not change with time (meaning,there are no external forces). The evolution of the distribution is written explicitly as:

$$f(z,t) = N\frac{\hbar\omega_z}{2\pi k_B T}\int_{-\infty}^{\infty} e^{-m\omega_z^2(z-v_k)^2/(2k_BT)} e^{-\hbar^2k^2/(2mk_BT)}\, dkdz \qquad (4.5)$$

The expansion rates and the density profiles are predicted using this equation

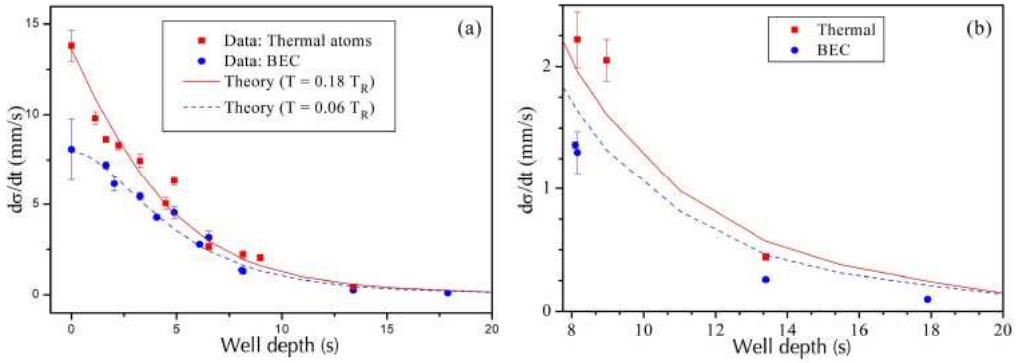

Figure 4.5: Expansion rate for different well depths.

for different lattice depths. The rate of expansion for zero lattice depth for thermal atoms is simply given by its temperature. For a BEC too, one can associate an "effective temperature" by measuring its free expansion in the waveguide. The expansion in this case is not due to a finite temperature but due to the interaction energy converting into kinetic energy. This measured "effective temperature" is used as an input parameter for the theory curve for the BEC. The initial temperature and lattice depth are the only parameters that characterize the evolution. For low lattice depths, both the thermal atoms and BEC fit well to the single particle model. Thermal atoms fit the theory very well, which is not a surprise. However, even the BEC seems to fit well for low lattice depths. The rate of expansion for low lattice depths is too large for interactions to have any effect on the evolutionary dynamics. The large expansion velocity causes the density (and hence the interactions) to drop off very rapidly during expansion. A few milliseconds into their expansion, the atoms basically act like independent particles. This is also corroborated by

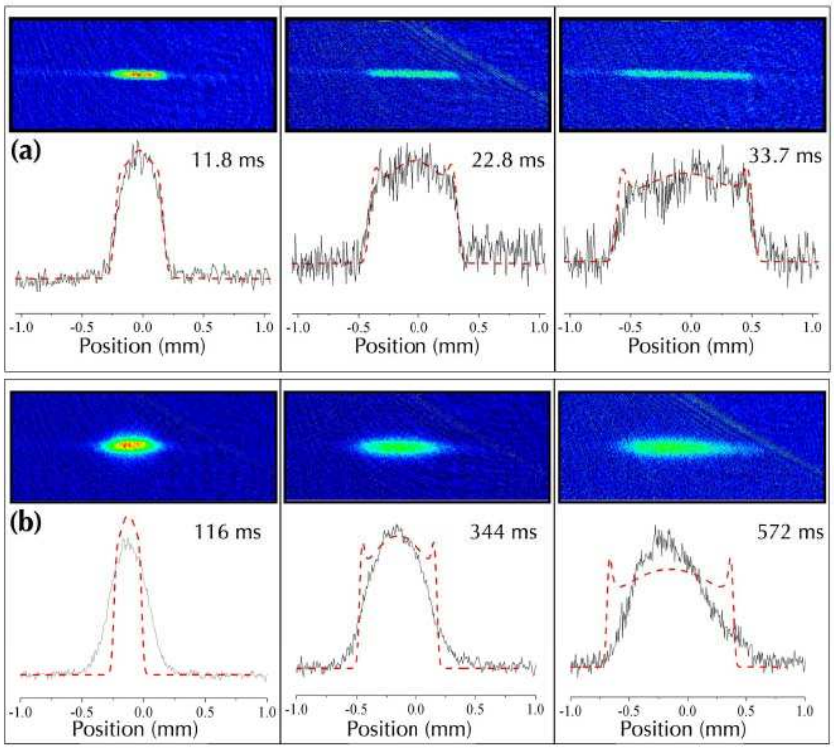

Figure 4.6: Density profile after expansion for a BEC and thermal atoms.

the fact that the rate of expansion is much larger than the speed of sound in the BEC (estimated to be $\sim$3 mm/s) which roughly characterizes the ability of atoms to "talk" to each other. For large well depths, the rate of expansion of BEC was slower than that predicted by the single particle model. The BEC atoms in this case have enough time to interact during expansion which causes this deviation. This is the region where interactions become important in the dynamics.

To further explore this phenomenon, we analyzed the density distribu-

tions for BEC and thermal atoms. Fig. 4.6(a) shows the expansion of thermal atoms. The dotted curve is the theoretical prediction using Eq. 4.5. The distributions fit beautifully to the predicted curves and there are no free fitting parameters. It is interesting to note the sharp edges that develop during the expansion of thermal atoms. In the lowest band, the group velocity has a maximum value for certain k beyond which it begins to fall sharply as seen in Fig. 4.2. Thermal atoms fill the lowest band almost completely. As time evolves, no atoms are allowed to travel faster than this maximum group velocity giving rise to this peculiar feature of a sharp moving edge in the density distribution. The BEC occupies a much smaller region in the lowest band and is always in the quadratic dispersion region. Hence, we were unable to see this feature for the BEC. Fig. 4.5(b) shows the density profiles as the BEC expands in the lattice. The dotted curves, again, are single particle predictions. The distributions do not fit the simple theory anymore. The suppression of expansion seen here is due to interactions. Atoms can move freely in an optical lattice due to resonant tunneling induced by the spatial symmetry of the potential. In the tight binding approximation, there is enhanced probability of tunneling from one site to the other if the energies at the two sites are degenerate (as is the case for a periodic potential). The interaction energy of a BEC (which depends on the local density) breaks the translational symmetry of the lattice causing a mismatch between the energy levels in adjacent sites. This suppresses tunneling as seen in our case. Higher the density gradient, larger is the energy difference between adjacent sites, causing greater suppression of tunneling. An extreme case is nonlinear self trapping where transport is

prohibited altogether [27].

4.3 Theory of the kicked rotor

The delta kicked rotor is a classic problem in nonlinear dynamics. The statement of the problem is:*A closed system of particles is kicked periodically with an external force (potential). How does the energy of the system evolve?*. The potential form studied extensively in theory [28] and experiments [29, 30] is the sinusoidal periodic potential. This potential is easy to create using an optical lattice and it gives good control over the kicking strength. The Hamiltonian of such a system is:

$$H(\rho, \phi, \tau) = \frac{\rho^2}{2} + K\cos\phi \sum_{n=1}^{N} f(\tau - n) \tag{4.6}$$

The variables here are scaled as follows:

$\tau = t/T$, where T is the period between kicks.

$\phi = 2k_L x$, where k_L is the lattice wave vector.

$\rho = \frac{\bar{k}}{2\hbar k_L} p$, where $\bar{k} = 8\omega_r T$ is also called the *scaled Planck's constant* because it satisfies the commutation relation: $[\phi, \rho] = i\bar{k}$. ω_r is the recoil energy divided by $\hbar$.

$K = \bar{k} t_p V_0/(2\hbar)$, is the stochasticity parameter. The pulse is assumed to be a square pulse of length t_p and V_0 is the well depth of the lattice.

In the limit that the pulse is a delta pulse, the problem is called the "δ-kicked rotor". Classically, the solution to this problem is the standard map characterized by the stochasticity parameter K. For small values of K the motion is largely bounded and for $K >\sim 4$ there is widespread chaos leading

to unbounded energy. This is the diffusive regime where the energy grows linearly with number of kicks. The evolution of squared momentum is linear with the number of kicks at a rate of $K^2/2$. The finite pulse corrections to these results can be found in [31, 32].

The quantum mechanical solution to this problem, has some interesting surprises. For $K > 4$ where we would expected unbounded energy growth, the energy of the system begins to saturate and remains bounded for large number of kicks. This behavior is called "dynamical localization". Dynamical localization was observed experimentally in our lab [33]. A peculiar characteristic of dynamical localization is the emergence of exponential distribution in momentum space. This behavior has been mapped to the famous Anderson localization problem [34] in real space where a density distribution transforms into an exponential distribution if it is allowed to evolve in a potential that is disordered above a critical value. Dynamical localization can be considered as momentum space analogue of Anderson localization. The disorder in momentum space is generated by the kicks and if they are above some critical strength, they localize the momentum distribution.

The goal of our experiment was to study the effect of atomic interactions on the process of dynamical localization. In previous experiments, the pulse width was hundreds of nanoseconds and the duration between pulses was microseconds. To study interactions, we need to give atoms enough time between pulses to interact. If the pulses come too fast, the behavior would be like that of a non interacting gas. An ideal experiment would be one where

dynamical localization for thermal atoms can be observed for pulses separated by many milliseconds. Once could then repeat the experiment for a BEC to study effects due to interactions. However, to allow for tens of milliseconds of evolution time, the atoms have to be confined in a box to prevent them from expanding and falling under gravity. Moreover, the interactions would quickly become insignificant as the cloud expands and loses density. In the previous demonstration of dynamical localization, the total duration of the experiment was hundreds of microseconds. The atoms were kicked in free fall. The dynamics was completely dominated by the kicks because they were very strong. No external confinement was necessary since the evolution time was very small. Another complication is created by the lattice used to kick the atoms. The momentum kick from a submicron lattice is so large that in order to see dynamical localization, the period between kicks would have to be very small. This would leave no hope of seeing the effect of interactions. In order to observe dynamical localization for large period between kicks, the lattice had to be of a longer wavelength. While we were able to overcome both of the above problems, we had other problems that prevented us from seeing the desired results. We did see a signal very similar to dynamical localization but due to a completely different classical effect as will be explained in the next section.

4.4 Kicked rotor experiment

The experimental setup for the kicked rotor experiment is shown in Fig. 4.7. The atoms are confined in a magnetic waveguide similar to the quantum

transport experiment. The confinement along the axial direction is due to two laser sheets (we call them billiard beams). The sheets are made of 532 nm laser beams that are focused at the atoms to a waist of 10.4 μm by 160 μm. The length of the resulting box was 127 μm. Each beam was capable of creating a potential barrier of height V_b= 18 μK. Since the barriers are so wide, the tunneling through the barriers is negligible. A BEC loaded into this box had a lifetime of more than 7.5 s. Both the billiard beams were derived using an AOM driven at two different RF frequencies. Each frequency creates a beam whose position can be controlled independently but their powers are coupled. To create the periodic potential, the same AOM is driven by 5 more frequencies to create additional beams between the billiard beams (we called these the interaction beams). The interaction beams had 5 spots with a spacing of 22.5 μm between adjacent beams. The power in these beams was typically much lower than the billiard beams. To kick the atoms, the interaction beams were pulsed on and off using an RF switch. The power in each interaction beam was set to be the same. After a certain number of kicks the temperature and atom number were measured.

Fig. 4.8 shows typical evolution of energy with number of kicks. The data is shown for two different kick periods, 10ms and 100 ms. There are a number of things to note in this plot. The blue squares represent the temperature measured in the axial direction of the waveguide while the red circles represent the temperature in the radial direction. For kick period T= 10 ms, the radial temperature is always lower than the axial temperature. The kicks are predominantly in the axial direction since that is the direction of strongest

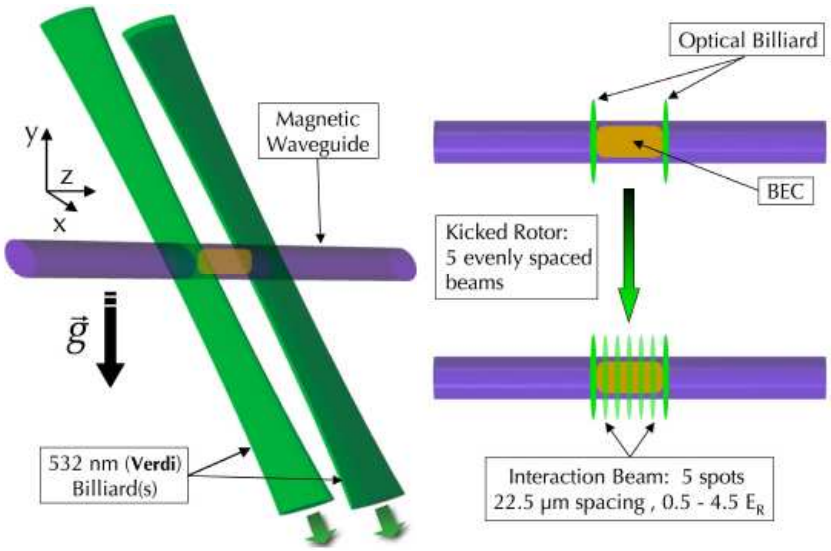

Figure 4.7: Setup for the kicked rotor experiment. Graphics rendered by Kevin Henderson.

energy gradient. However, we see that it increases the temperature even in the radial direction. There are two possible explanations for this. First, the axis of the box could be misaligned with respect to the interaction beams, which would then impart some kick in the radial direction. This misalignment, however, seemed very small and not very easy to quantify. The second and the more likely reason is the mixing of energies in the two dimensions. The waveguide is "quasi-1D" which implies that atoms can move even in the transverse direction. After giving kicks, both directions will thermalize after some time (depending on the collision rate) and the temperature along the transverse and axial directions will be the same. This extra degree of freedom essentially breaks the approximation of a 1D rotor. As seen from the data, the mixing is much more evident for longer kick period T= 100 ms where the

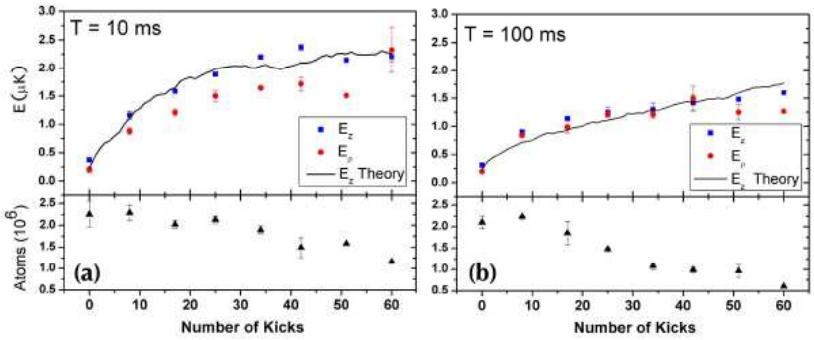

Figure 4.8: Evolution of energy with number of kicks for T= 10 ms and 100 ms. E_z (■) and E_ρ(•) are the energies measure in the axial and radial directions respectively. For this data: t_p= 200 μs, V_0= 35 KHz. The atom number data (▲) shows only the statistical uncertainty (excluding the calibration uncertainty of ∼10%).

axial and radial temperatures are essentially the same.

The most obvious observation from the plot is finite bound on temperature. It begins to saturate after about 40 kicks. This behavior looks very similar to dynamical localization where, the energy begins to saturate after a certain number of kick called the break time. However, the expected value of the saturation energy does not match the observed value. For example, for the parameters of the plot in Fig. 4.8(a), the stochasticity parameter K= 58 and the localization energy is 57 μK. The observed effect is not dynamical localization. The bottom of each figure shows the number of atoms as a function of kicks. It is clear that the atoms are being lost due to the kicking process. This provided us with the explanation for the observed effect. The hot atoms were simply being thrown out of the box since the box height was only 18 μK. The remaining atoms thermalized (or not) in the time between the kicks depend-

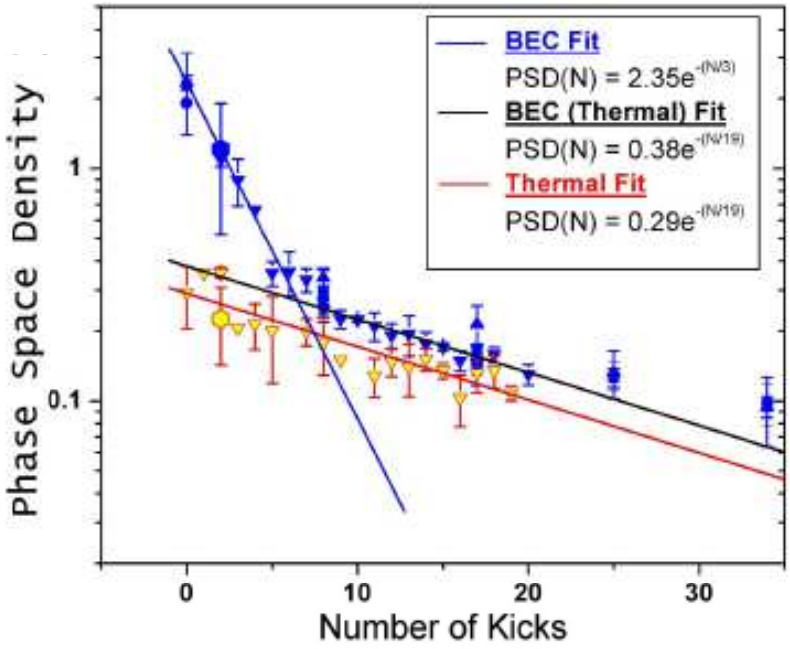

Figure 4.9: Phase space density evolution with the number of kicks.

ing on the collision rate. In either case, the system reaches a non-equilibrium steady state where the heating due to the kicks is the same as the cooling due to the loss of hot atoms. The continuous lines in the plot are numerical simulations where we assume a constant collision rate of 5 Hz, which is consistent with the measured density and temperature values. To keep track of the atom number and energy at the same time, we plot the phase space density (PSD) of the ensemble as a function of kicks in Fig. 4.9. The blue data points are for a BEC and the red ones for thermal atoms. The different shapes of the blue points correspond to different times between kicks. All those curves fall on top of each other showing that the evolution in PSD depends only on the

number of kicks and is independent of the kick period T. The evolution of PSD is exponential (for thermal atoms and BEC) with respect to the number of kicks. The PSD drops with a higher exponent for a BEC. As the BEC heats up due to the kicks, it releases the interaction energy stored in the form of chemical potential. This causes a sharper drop in PSD which continues till the BEC fraction is negligible. Once the BEC is destroyed, the PSD drops much slower and the rate is identical for a BEC and thermal atoms as can be seen from identical slopes for the two curves. Thermal atoms lose PSD at a fixed exponential rate.

In conclusion, the setup did not allow us to go into a regime to see interesting quantum effects. The height of the billiard beams was too small to confine the high energy tails of the distribution. The design of the chamber would not allow us to focus our beams any smaller. The limit was the laser power and, unfortunately, it is a very expensive problem to solve!

Chapter 5

Introduction to Fock states of atoms

Focks states are most commonly encountered in physics when we solve the quantum harmonic oscillator. The energy levels in that case are equally spaced and the eigenstates of energy are also the eigenstates of number of phonons (or photons) with energy equal to the energy spacing. Fock states for photons have been realized in a cavity [35], using entangled photons [36], controlling the emission from a single molecule [37], color center [38] or quantum dot [39]. A N photon Fock state in case of a cavity is defined as having N photons in a certain mode of the cavity. Photons can be created and destroyed. This freedom is used to create photons directly in some cavity mode (using an atom passing though a cavity, for example). The process can be repeated, in principle, to have N photons in the same mode of the cavity to produce the desired N-photon Fock state. A number of experiments have studied the properties of Fock states [40, 41] and their application in quantum information transmission and processing [42–44].

Fock state of N atoms can be defined, similar to photons, as having N atoms in a certain energy eigenstate of a trap (which could be harmonic but is not necessary). In principle, this state could be any state of the trap but experimentally, the ground state is most easily recognizable. Creating

atoms in the ground state (as in the case of a BEC) is much easier than, say, the second excited state. Another important difference between atoms and photons is, unlike photons, atoms can be Bosonic or Fermionic. As will be pointed out in chapter 7, creating Fock states using Fermionic atoms might be easier than Bosonic atoms. In our case, however, we had a ^{23}Na BEC setup and hence we used Bosons.

Photons can be directly created in a certain cavity mode. Atoms, on the other hand, cannot be created. We have to rely on a different method to precisely control the atom number. The original proposal to do this was the so called 'quantum tweezer', proposed in **??**. The original scheme evolved into a simpler scheme called "Laser Culling" [45] but only after initial experimental success with that method to observe sub Poissonian number statistics for small atom numbers [46]. This chapter highlights the physical principles involved in the creating Fock states of atoms.

5.1 Method for creating Fock states

A Bose Einstein Condensate begins to form when a significant fraction of atoms begin to occupy the ground state of the trap. This is done by cooling an atomic sample to a very small temperature (below the critical temperature for the phase transition) by evaporative cooling. This process of throwing away hot atoms and the rethermalization of the remaining ones is random and consequently the number of atoms left at the end is indeterminate. If no other factors contribute to fluctuations, the expected distribution is Poissonian

with an average of N atoms and a fluctuation of $\sqrt{N}$ (in experiments, typical fluctuation in number is 10% for 10^5 atoms, which is much larger than the poisson limit due to technical causes). As we produce a more pure BEC, we ensure that a higher fraction of atoms are in the ground state but the number still has a $\sqrt{N}$ uncertainty (at best). The method proposed to squeeze this number distribution is called Laser Culling [45]. The method exploits the fact that atoms in a BEC interact with each other. Though atoms in a BEC are in the ground state of the external trap, the precise energy depends on the interaction between atoms which in turn depends on the number of atoms present in the BEC (according to Eq. 5.1). If we create a finite height trap such that the energy of N atoms is just below the trap height but the energy of (N+1) atoms is higher than the trap height then the trap will be able to hold N atoms but not N+1. If we now reduce the height of the trap so that it goes just below the interaction energy of N atoms then, one atom has to leave the trap which will bring the energy just below the trap height and now (N-1) atoms will be left in the trap. The loss of atoms in this way is not random (unlike evaporation) and can be controlled by changing the trap parameters. This discussion neglects any tunneling out of the well (which will be finite since the trap is of finite height and size) but there are ways to reduce it as will be discussed later.

Consider the case of a BEC held in a finite size 3D harmonic trap as shown in Fig. 5.1. The trap has a height U_0 and the BEC fills the trap completely. The energy of the N-particle BEC is its chemical potential and

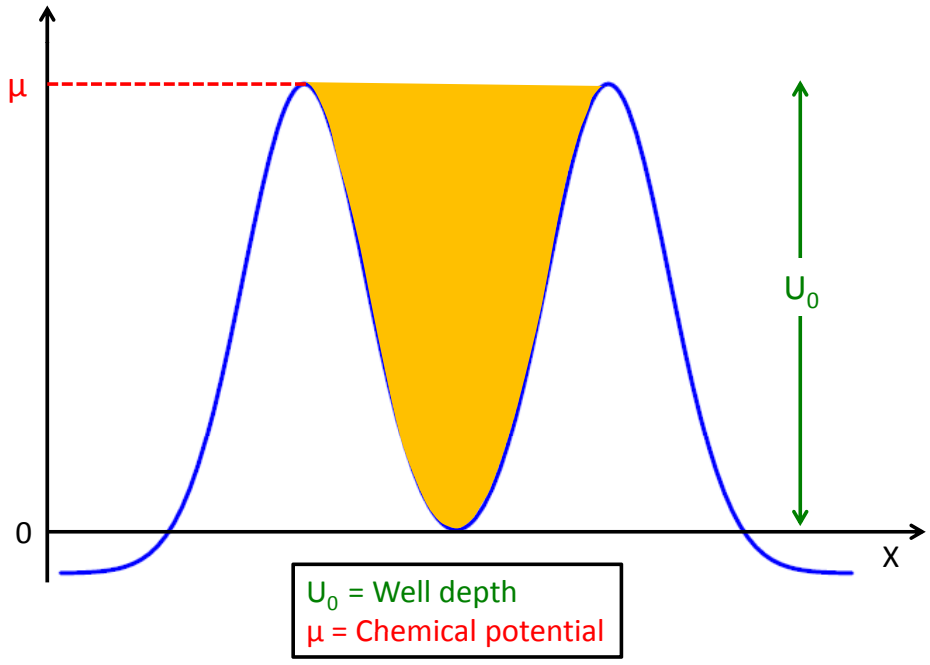

Figure 5.1: Principle of laser culling.

given by the Thomas Fermi approximation as:

$$\mu = \frac{15^{2/5}}{2}\left(\frac{a}{\bar{a}}\right)^{2/5}\hbar\bar{\omega}N^{2/5} \tag{5.1}$$

Here, $\bar{\omega} = (\omega_1\omega_2\omega_3)^{1/3}$ is the geometric mean of the trapping frequencies along the three directions,, $\bar{a} = \sqrt{\frac{\hbar}{m\bar{\omega}}}$ is the characteristic oscillator length and a is the s-wave scattering length of the atom. The quantity of interest while performing laser culling is the difference in energy for a N atom BEC and a N-1 atom BEC. This quantity is:

$$\Delta E_N = \frac{\partial\mu}{\partial N} = \frac{15^{2/5}}{2}\left(\frac{a}{\bar{a}}\right)^{2/5}\hbar\bar{\omega}\frac{2}{5}\frac{1}{N^{3/5}} \tag{5.2}$$

Using the constants for sodium ($a = 2.75 \times 10^{-9}$ m, $m = 3.82 \times 10^{-26}$

Kg) and moderate trap frequencies ($\omega_1, \omega_2 = 2\pi$ 300 Hz, $\omega_3 = 2\pi$ 30 Hz) and atom number (10^5), this gives an energy difference of ΔE_N= 0.6 pK. This energy is so small that the atom number fluctuation remains dominated by technical noise (noise in laser power, noise in currents, etc). For laser culling to work effectively, this energy scale has to be larger than technical noise. This could be achieved by going to smaller atom numbers (eg: for 100 atoms, the energy difference is 37 pK) and increasing the interactions using a Feschbach resonance, going to lower dimensions or some other method. While the above equation is not valid in 1D or for very low atom numbers, the basic method is still valid and the results are similar. The case for atoms in 1D has been discussed theoretically in [45] where the atoms are held in a 1D box of finite height. In the case of strong interactions (Tonks limit), the problem of N interacting bosons can be mapped to a problem of N non interacting Fermions [47]. This mapping provides a way of deducing the occupation of different energy levels. Fig. 5.2 shows the calculated energies for different atom numbers as a function of the box height. As the well depth is reduced, two curves intersect at a point where one particle is ionized and the system follows the N-1 particle curve. The energies are in units of $\hbar^2/mL^2$. For sodium atoms in a 10 μm wide box, the energy difference in the 4 and 3 atom ground states is about 10 nK which is in a range where the technical noise can be made smaller than this. There are a couple of issues not addressed in the above discussion. First one being tunneling out of the barrier and the second one that of adiabaticity of the process. The tunneling problem, in principle, is not very difficult to solve. In a previous experiment [46] the 1D box was

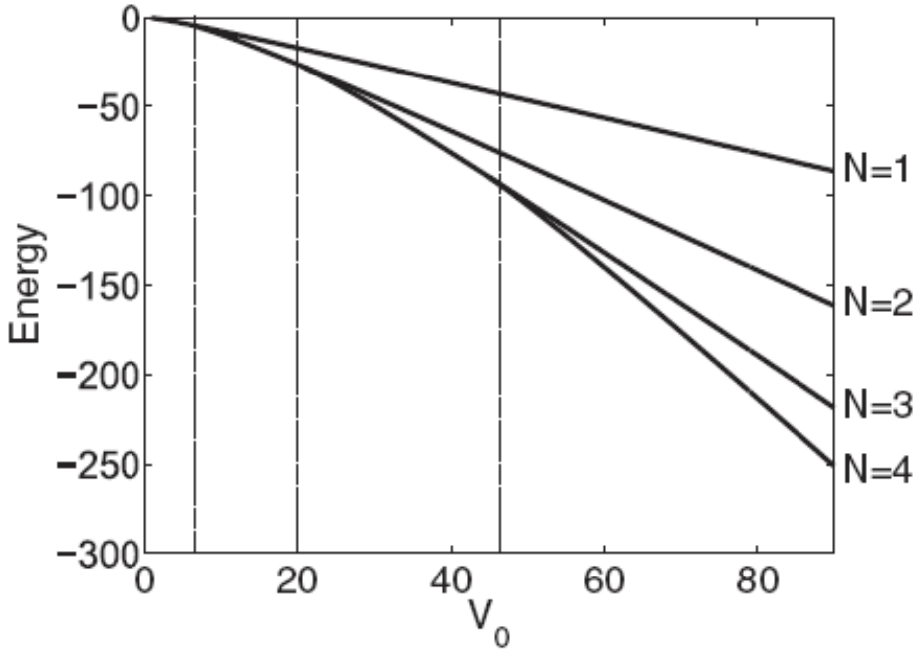

Figure 5.2: Ground state energies of N bosons in a finite well. Adapted from [45]

created using laser beams. The two walls were created by laser beams derived from a single AOM which was driven by two Rf frequencies at the same time. In order to minimize tunneling out of the barrier, the walls of the box could be made thicker by creating multiple overlapping spots by driving the AOM with even more frequencies, each one creating a spot whose position can be controlled by changing the RF frequency. The problem of adiabaticity has been addressed in [48] where they find that a combination of trap reduction and squeezing provides a robust mechanism for Fock state preparation.

5.2 Sub-Poissonian statistics

The energy spacing between N+1 and N atom ground states is very small for large numbers and a weak trap, as shown earlier. As the number is reduced, this spacing increases. Although it does not become large enough to be able to create Fock states, it was observed in [46] that it already begins to squeeze the number distribution below the Poissonian limit. The experiment was done with a ^{87}Rb BEC confined in a 3D gravito-optical trap with a mean trapping frequency of $\bar{\omega}$= 300 Hz. They observed number squeezing below N = 500 all the way down to 40 atoms beyond which the fluctuation increased again. The two main problems that prevented the creation of Fock states in that setup were (a) the trapping frequencies were not high enough, resulting in weaker interactions and smaller energy splitting and (b) the detection for low atom numbers had big uncertainty due to the capture of background atoms during fluorescence detection. The sodium experiment was designed to be an improvement over this by going to the 1D regime where the interactions are the strongest and the detection would be more reliable for low numbers, since sodium has much lower vapor pressure resulting is very little background capture, if at all. This would allow us to squeeze the distribution to a point of creating high fidelity Fock states.

Chapter 6

Experimental setup 2

This chapter describes the experimental setup devised to create Fock states. It describes all the important aspects of the experiment, including, laser systems, vacuum chamber and optical and the mechanical setups necessary in the experiment.

6.1 Laser system

The laser system and optics setup for near resonant light is shown in Fig. 6.1. We use two lasers:

1. A Coherent Verdi V-18 is a diode pumped solid state single frequency laser at 532 nm and is used to pump the dye laser and create dipole traps (optical plug and the 1D box).

2. A Coherent 899 dye laser at 589 nm , which is used for laser cooling and detection of atoms.

The Verdi V-18 turn-key system is a relatively new addition to our lab and was bought in September 2006. In just the first year, the laser failed twice. The laser spontaneously turned off and none of the routines in the manual

helped. In both cases, it was a manufacturing defect and the laser head had to be replaced. Since then, however, it has been working well. We cool the baseplate using an external chiller (Neslab, Model: Merlin M33) with a cooling power of 1.1 KW (much higher power than the manufacturer recommends) carrying water at 80 psi and set to 22° C. This allows us to run the laser at a lower power for a longer time which is crucial for alignment purposes. The water connections are stainless steel swagelok. We add some ethylene glycol to the chilling water to prevent rusting. The output of the laser is split using a 40/60 beamsplitter. The reflected beam is used to pump the dye laser and the transmitted beam is used for creating the optical plug and the 1D box beams. The area covering this optics and the laser is enclosed in a colored plastic box to prevent dust and air currents from distorting the beams and blocking all the stray light. The transmitted beam is split using a 50/50 beam splitter to create the plug beam and the 1D tube beam (the endcaps of the 1D box are created by the plug beam since it is not used during that stage of the experiment), details of which will be given later in this chapter. With the Verdi at 18 W, 7.27 W are used for pumping the dye laser, 5.47 watts for the plug beam and 5.13 Watts for the 1D tube.

The dye laser runs on Rhodamine 6G dye mixed with ethylene glycol flowing at a pressure of 40 psi and cooled to 5° C. The dye lasts for about 6-8 weeks after daily operation before it bleaches and has to be changed. We mix 1.2 g of dye and add ethlylene glycol ($\sim$ 1.4 L) until 85% of the pump power is absorbed by the dye. For 6.4 W of pump power, the laser outputs 1.1 W at 589 nm single frequency. Part of the beam is picked off by

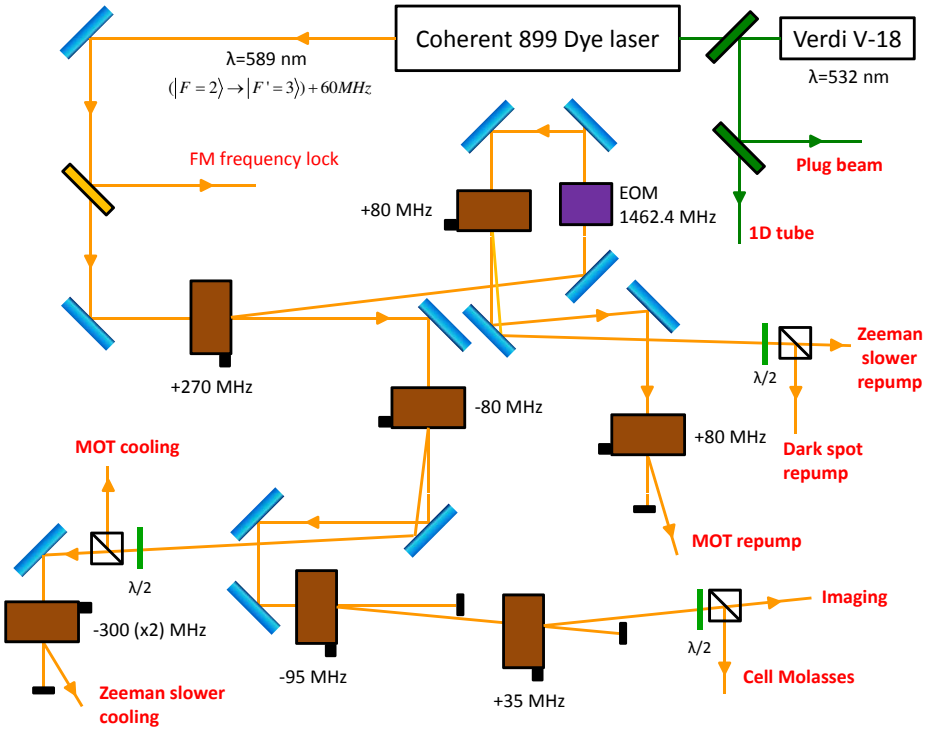

Figure 6.1: Laser setup.

a coated window and transported to a wavemeter through an optical fiber. The wavemeter measures the laser frequency with a resolution of 10 GHz relative to a HeNe standard laser. Once close to the transition, the absorption lines are seen using a saturated absorption scheme and locked 60 MHz to the blue of the $|F = 2\rangle \rightarrow |F' = 3\rangle$ transition as described in [49]. Before we proceed with the laser frequency manipulations, it is useful to know the different energy levels and their spacings for the sodium D2 transition as shown in Fig. 6.2. The cooling light for the MOT is detuned 20 MHz to the red of $|F = 2\rangle \rightarrow |F' = 3\rangle$ transition. The repump light is on resonance with

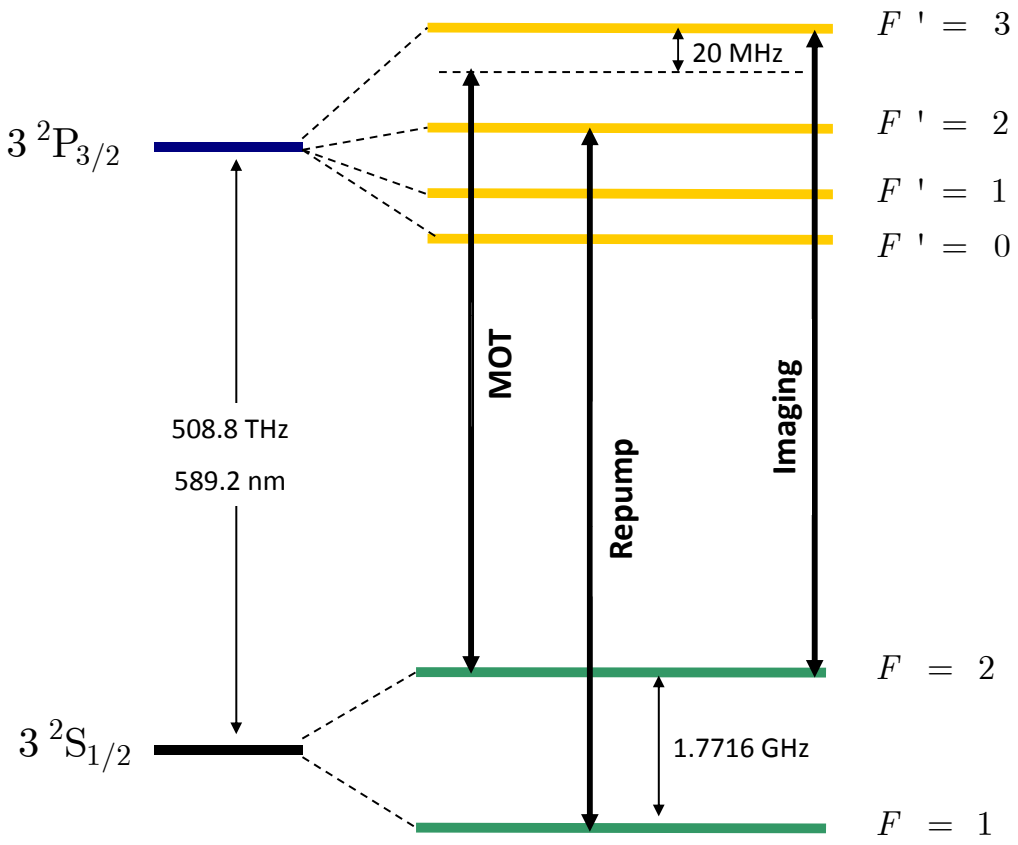

Figure 6.2: Energy levels in Sodium. (Graphics rendered by David Medellin)

the $|F = 1\rangle \rightarrow |F' = 2\rangle$ transition. The absorption imaging light is close to resonance with the $|F = 2\rangle \rightarrow |F' = 3\rangle$ transition. In addition to the above, we also have the Zeeman slower beam which is detuned 600 MHz below the MOT cooling light. All these beams are created as shown in Fig. 6.1.

The beam passes through a 270 MHz AOM whose first order is used for the repump beam and the zeroth order for the MOT cooling beam. The MOT light passes through a 80 MHz AOM (MOT AOM) that down shifts

the frequency by 80 MHz resulting in a detuning of 20 MHz to the red of the $|F = 2\rangle \rightarrow |F' = 3\rangle$ transition. The MOT AOM is used to lock the power in the MOT beam using a feedback circuit that regulates the power close to the chamber by modifying the RF power driving the AOM. The MOT beam is further split by a polarizing beam splitter cube. One of the beams goes towards the chamber and creates the six MOT beams while the other beam is double passed though a 300 MHz AOM to create the Zeeman slower beam. Prior to the double pass AOM, part of the beam is picked off and used for 2D molasses located just after the differential pumping tube (described in section 6.3). Some part of the 2D molasses beam is passed through a 600 MHz AOM and used as a secondary Zeeman slower beam. The zeroth order of the MOT AOM is used for the imaging beam after it passes through a 95 MHz AOM and then through a 35 MHz AOM. This AOM combination brings the beam on resonance with the $|F = 2\rangle \rightarrow |F' = 3\rangle$ transition. Part of this beam is split using a polarizing beam splitter cube and coupled into a fiber to be used for the 3D molasses beams in the glass cell. This is used for fluorescence detection and will be explained in section 6.13. The first order of the 270 MHz AOM is passed through an Electro Optic Modulator (EOM) driven at 1462.4 MHz that adds two sidebands to the beam. The beam passes through another 80 MHz AOM whose first order is used as the repump beam for the dark spot and the Zeeman slower cooling beam. The zeroth order of this AOM is used as repump for the MOT after passing through another 80 MHz AOM. This describes all the beams required for the experiment. The powers in each of these beams is summarized in Table 6.1. The total power in all the beams is

Beam	Power (mW)
MOT Cooling (total)	140
MOT Repump (total)	35
Dark Spot Repump	30
Zeeman Slower Cooling	40
Zeeman Slower Repump	11
2D Molasses (MOT+Repump)	50
Secondary Zeeman Slower (MOT+Repump)	50
Absorption Imaging	10
Cell Molasses (MOT+Repump)	2

Table 6.1: Powers in different near resonant laser beams before entering the chamber.

228 mW. A lot of power is lost at AOM's, spatial filters, and in stabilizing power in the beams.

6.2 Vacuum Chamber

The vacuum chamber consists of two main parts: the oven chamber region and the the zeeman slower with the science chamber region. The two regions are separated by a gate valve. Fig. 6.3 shows the design of the complete vacuum system.

6.2.1 Oven

The oven design was inherited from the previous experimental setup. It has a lot of extra provisions that, in the end, did not prove to be very useful and added to the complexity of the setup. Fig. 6.4 shows the oven and the chamber design. We load 15 grams of sodium into the cylindrical cavity of the oven that has a 4 mm aperture for the vapor to escape. The heaters

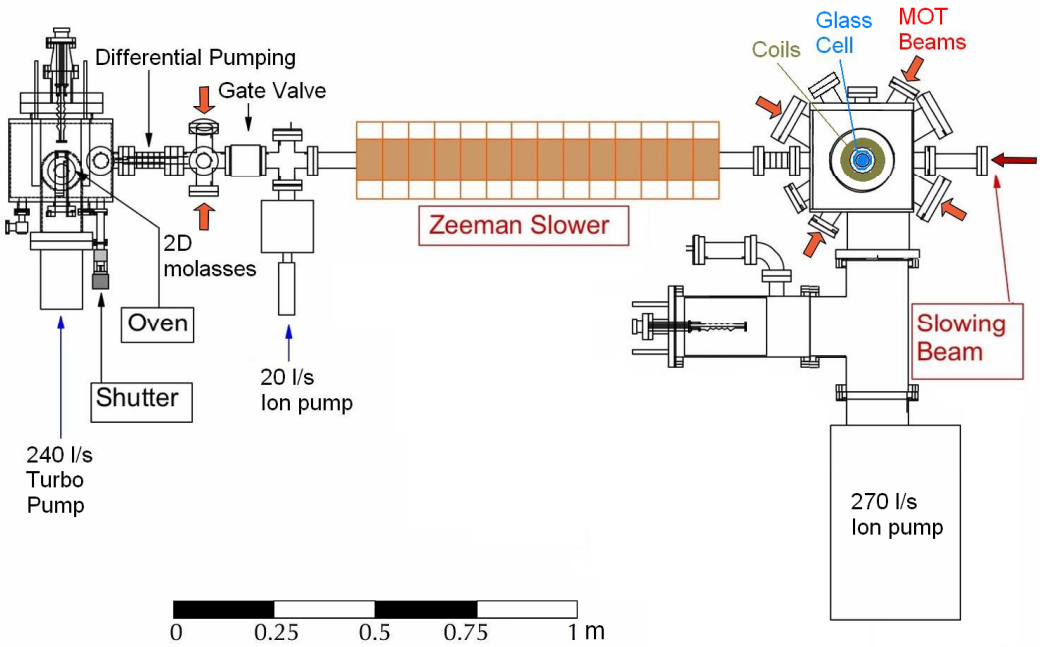

Figure 6.3: Vacuum system. The 20 l/s ion pump failed and had to be replaced with a different one in the 2D molasses region. (Graphics rendered by David Medellin.)

are installed from the outside to heat the cavity. The oven is installed inside the oven chamber with a 2-3/4" flange which was designed to be rotatable. This causes huge problems in aligning the aperture of the oven to the the differential pumping tube and the zeeman slower. The oven is surrounded by a cryoshroud which was intended to trap the excess sodium vapor coming out of the oven and prevent it from increasing the base pressure. We cooled the cryoshroud with liquid nitrogen but since it did not help much in reducing the background pressure, it was abandoned. The cryoshroud has a 0.5" hole so that the straight beam from the oven can escape. The chamber also has a titanium sublimation pump. This too is not very helpful since the base

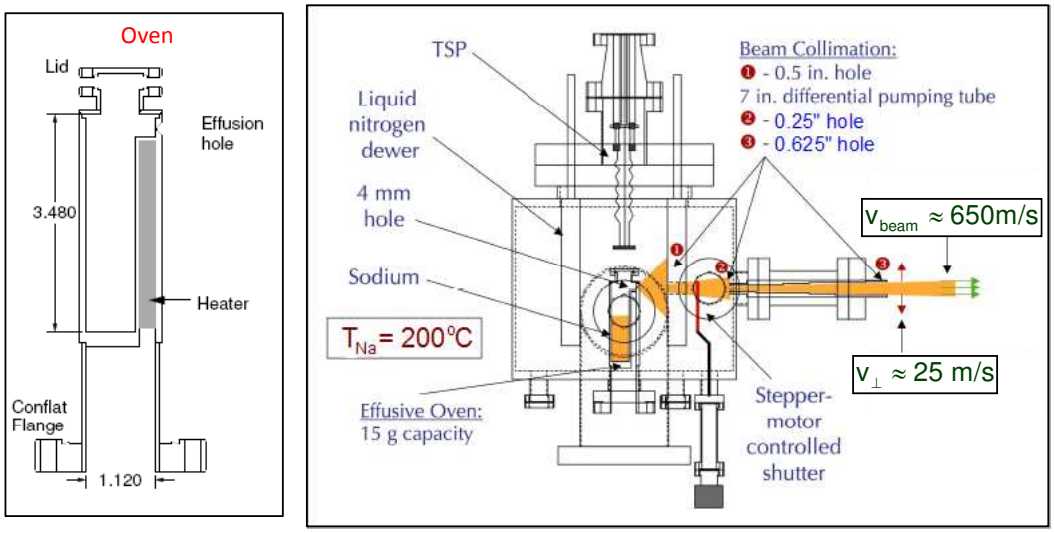

Figure 6.4: Oven chamber design. Adapted from [20, 21]

pressure increases to more than 10^{-9} Torr after heating the oven during the experiment. The oven chamber is pumped by a 240 l/s turbo pump (BOC Edwards, Model: EXT 255H). The pressure in the chamber is monitored by a Bayerd Alpert ion gauge. The oven chamber contains a metal flag that can be used to block the direct beam from the oven aperture. This is done after the atoms are loaded from the MOT into the magnetic trap to prevent the direct atomic beam from increasing the base pressure in the science chamber and reducing the lifetime in the magnetic trap. The oven chamber is separated from the rest of the system by a differential pumping tube. The tube is 7" long and conical in shape with a diameter of 0.25" at one end and 0.625" at the other. The tube was made conical to match the divergence of the atomic beam as it exits the oven. This differential pumping tube by itself turned out to be

insufficient and another 1" piece was added to it later with a diameter of 0.125" which fit snugly over the previous tube. The conductance of the tube is 0.15 l/s which is enough to maintain a pressure difference of three orders of magnitude between the oven chamber and the science chamber. The oven chamber is connected to the 2D molasses section with a flexible bellows. For optimum flux in the science chamber, the oven aperture, the cryoshroud hole and the differential pumping tube all have to be collinear. The only view to do this alignment was from a viewport on the oven chamber that is at right angles to the direction of the atomic beam. Through this viewport, we can see the hole in the cryoshroud, the end of the differential pumping tube and the flag used to block the atomic beam. We can also see the Zeeman slower beam when it makes all the way through the differential pumping tube. The alignment of all the parts mentioned earlier is not automatic and needs to be redone every time we changed sodium because of the rotatable flange for the oven which allows angular mislignment of the oven with respect to the differential pumping tube. In order to carry out this difficult alignment, the oven chamber is mounted on an aluminum platform raised above the supporting structure using four screws. The platform can be tilted or even moved around to optimize the atom number in the MOT. Having so many degrees of freedom is necessary for alignment but it makes the optimization very difficult and it typically takes weeks to get a satisfactory beam flux into the science chamber after every sodium change. The 2D molasses region consists of a 6 way cross with four coated viewports. This section is connected to a 20 l/s ion pump (Varian StarCell) for better pumping in the zeeman slower region.

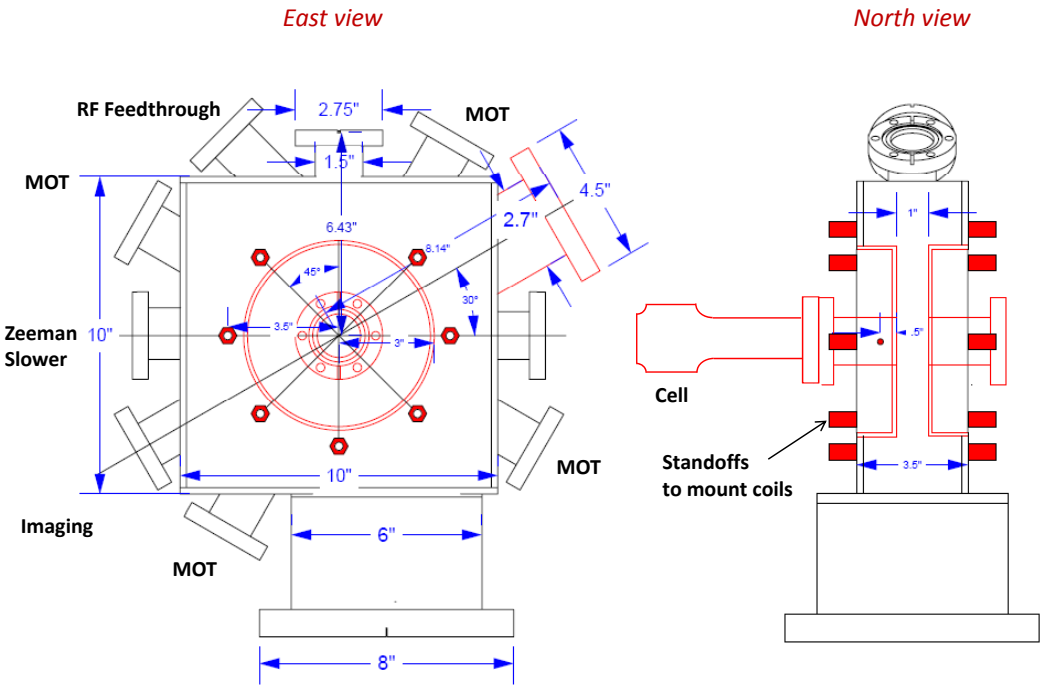

Figure 6.5: Science chamber design. The north view also shows the 8-32 screw, designed to hold the RF coils, that were dissolved during electropolishing (see section 6.6).

Under normal operating condition the temperature of the oven is 200° C. The oven lifetime is 750 hours at this temperature after which we have to break vacuum in the oven chamber to replenish the sodium. The gate valve (VAT, Model: 48132-CE01) between the 2D molasses region and the zeeman slower is crucial for this process to isolate the science chamber (10^{-11} Torr) from the oven chamber.

6.2.2 Science Chamber

The gate valve is connected to the zeeman slower tube which is about a meter long. The pressure in this region is monitored by an ion gauge. The end of the tube is connected to the science chamber shown in Fig. 6.5. It is a modification of the previous science chamber that was originally designed for a cloverleaf magnetic trap that gives full optical access in a plane perpendicular to the axis of the trap. The modified chamber was very similar in that respect except, that the cloverleaf coils were replaced by simple quadrupole coils for the optically plugged quadrupole trap. The buckets in the chamber allow for close proximity of the quadrupole coils giving higher magnetic field gradients. The distance between the inner walls of the buckets is 1". The science chamber has viewports for the MOT beams and an extra port for the plug beam. Elelctrical feedthroughs are connected on one of the flanges to enable connections to the RF coils mounted inside the chamber. The chamber is pumped by a 270 l/s ion pump located below the chamber. After the chamber was modified, it was electropolished from the inside (by Central Electropolishing Company Inc). This polishes the rough regions on the chamber surface and creates a chrome coating that makes it easier to achieve UHV.

6.2.3 Glass cell

The creation of optical traps for tight confinement requires that the focusing lenses be placed close to the atoms. This made it imperative to have a glass cell mounted on the chamber where the atoms would have to be moved in order to do experiments in the optical trap. There are a few options available

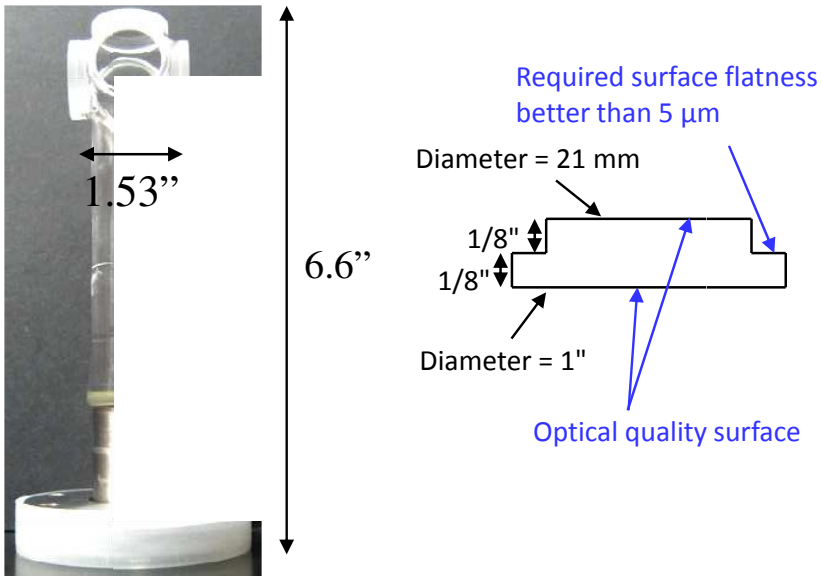

Figure 6.6: Glass cell and the modified window design.

to get a commercial cell. We decided to have it custom made by Ron Bihler of Technical Glass Inc. The cell is manufactured by fusing optical quality glass windows together to create a cell of desired style. The photograph of our finished cell is shown in Fig. 6.6. The cell design was fairly simple and the main requirements were to maintain the optical quality of the windows during the fusing process and have the smallest possible overall length. The fusing process utilizes a glass frit that needs to be heated to a very high temperature to fuse the window to the glass body. AR coatings do not survive this temperature so we had to use uncoated windows (CVI, Part: PW-1025-C). During the first few tries, there were problems with the frit sputtering onto the window during fusing. The problem seemed to be coming from a bad quality frit and

not easily solvable (apparently due to a lack of companies making frits). The solution we came up with was to machine the window edge to create a ledge so the seal would actually form below the level of the window surface which would make it hard for the sputtered material to land on the window surface. Fig. 6.6 shows the design of the modified windows. In order for the frit to work it is necessary that the mating surfaces have a surface roughness better than 5 μm. The windows were sent to Mindrum Precision Inc. to be modified. However, after were received the windows, we found that that the sealing surface had pits as big as 75 μm with extensive subsurface damage which, if not corrected, would result in a weaker seal or even leaks. The surface had to be lapped and 0.35 mm thick layer of material was removed to go below the subsurface cracks. This was done for all five windows and finally the parts were all sealed together. The results were satisfactory but the windows still had some spotting that was visible but not big enough to create problems (we thought). It took five and a half months and $6000 to get the cell.

6.2.4 Bakeout

Bakeout is a crucial part for attaining ultra high vacuum. The desired pressure for typical BEC experiments is 10^{-11} Torr or better. We did the bakeout in two part. The first part was the main chamber bakeout where the gate valve is kept closed. The oven chamber bakeout is much simpler and was done later. The magnets for the ion pumps were removed and the chamber connected to an external turbo station with a 70 l/s pump. The ion pumps were off during bakeout. The chamber was covered with cartridge heaters

or heater tapes. The zeeman slower tube has a heater that was installed when the zeeman slower was first setup. All heaters were covered with two layers of aluminum foil. One has to be careful to not let the heater elements come in direct contact with the foil or it can melt the foil. To avoid this, the heaters were covered with flexible steel or aluminum plates to disperse the heat before it reaches the foil. Thermocouples were placed at different locations like windows, the cell, and the zeeman slower tube. The electrical power needed for the heater comes from different circuits each of which can supply only 20 A of current at 120 V. We had to carefully manage the distribution of heaters (taking into account the power of each heater) on the different circuits to avoid overloading any circuit. The total electrical power at maximum temperature is 4 KW. Before the power is turned on we made sure that each heater was isolated and did not short with itself or ground. The electrical leads going up to the heaters should be arranged such that they are not exposed to very high temperatures (unless they have a high temperature protective sleeve). The heaters can sometimes fail at high temperatures so we had to carefully monitor the temperatures in different parts of the chamber and look for any cold spots. This could be an indication of a burnt out heater or that the power is not enough. Cold spots tend to minimize the effect of the bakeout since the gas accumulates at the cold surface rather than be pumped out.

The temperature and pressure is monitored continuously and logged about twice an hour. The average heating rate of the chamber is 10° C per hour. The glass cell is very delicate and sensitive to large temperature gradients. To prevent very large gradients we enclosed the cell in an oven made

of fire bricks (fire bricks were also used to cover the ion pump on the science shamber). Inside, there were two cartridge heaters with aluminum foil to disperse the heat evenly. Optical surfaces can develop spots if there is any residue left on them during installation. Especially after the bakeout, the spots become very clear but it is too late by then to rectify this if the spots are formed on the inside of the glass surface. For this reason, the cell was cleaned from the inside with acetone and dried with dry nitrogen to avoid condensation of water droplets on the surface that result in spots after bakeout. However, we did notice some spots on the cell after bakeout.

As the chamber temperature goes up during bakeout, the steel parts and gaskets expand and the seals become tighter than at room temperature. While cooling, however, the parts begin to contract and this creates a greater risk of leaks. It happens especially if there is torque on any of the flanges. We had leaks, twice, in our chamber during the cooling cycle. It was due to one extra vacuum connection that was inducing torque of a 8" flange. We had to modify the system to its current state (as shown in Fig. 6.3) which eliminated this problem. The maximum bakeout temperature was 175° C. The chamber was left at that temperature for 5 days at which point the rate decrease in the pressure was very small. The pressure in the chamber, before we started cooling, was 5.6×10^{-8} Torr. After reaching room temperature the pressure was 1.8×10^{-9} Torr. The ion pump magnets were installed and the 20 l/s pump was turned on first. The pump was turned on for a few seconds at a time which degases the ion pump and raises the pressure in the chamber (as high as 1×10^{-5} Torr). The pump was then left on for longer and longer times until

it started pumping rather than raising the pressure. The same was done for the 270 l/s ion pump. The ion gauges to monitor the pressure in the zeeman slower and the science chamber were turned on and degased to have a more accurate reading of the pressure. The ion gauge controller (Granville Phillips, Model: 350) has a built in setting to degas which passes a large current to clean the filament. The ion pump controllers were then set to protect mode that prevents the ion pump from damage in case the chamber pressure goes above 10^{-4} Torr. The pressure after one day of pumping was 3×10^{-10} Torr.

The next step was to seal the auxillary valve between the turbo station and the science chamber and disconnect the turbo station. In doing so, we found that the science chamber pressure went up almost an order of magnitude when we turned off the turbo pump, even with the valve closed. This indicated that the valve had a small leak. The leak, however, was small enough that we could disconnect the turbo station and the pressure would stay at 1.7×10^{-9} Torr. To fix this leak, we added a pinchoff tube at the open port of the valve and connected it to the turbo station. We then evacuated the pinch off tube and did a modest bake to 90° C for a day to remove any water. The pressure in the tube was 7×10^{-9} Torr. We pinched off the copper tube and effectively disconnected the chamber from the turbo station. This time, the pressure in the science chamber stayed at 2×10^{-10} Torr. Additionally, we put vacseal on the pinchoff region for extra sealing.

The pressure even further by using a titanium sublimation pump. 50 A of current is passed through a titanium filament (installed in the chamber)

for 1 minute. This sublimates titanium and releases the vapor that coats the chamber within its line of sight. Titanium has the property of sticking to other types of molecules. Sublimated titanium thus acts like a pump and eventually reduces the pressure in the science chamber down to 2×10^{-11} Torr. The high current driver for our Ti-sub pump was broken and we had increase the current manually. Care should be taken to increase and decrease the current slowly (0.25 Amp/sec) to avoid breaking the filament (which is like an incandescent bulb). Vacuum in the chamber typically only becomes better over time, if there are no other degassing sources present. If we do not run the experiment for a few days we see the ion gauge reading "zero Torr" which means that the pressure is below 10^{-11} Torr. When we run the experiment with the gate valve open, the typical pressure in the science chamber is 2×10^{-11} Torr.

6.3 Pre-Cooling

The atoms making it through the differential pumping are first cooled in the transverse direction by a 2D molasses. The 2D molasses beams are perpendicular to the atomic beam, making the configuration Doppler insensitive. The molasses beam is thus derived before the last double pass AOM for the zeeman slower. This cooling in the transverse direction increases the atom number in the MOT by about a factor of two.

6.3.1 Zeeman slower

The atomic beam is further slowed down using a Zeeman slower. The details of the Zeeman slower construction and testing can be found in [50].

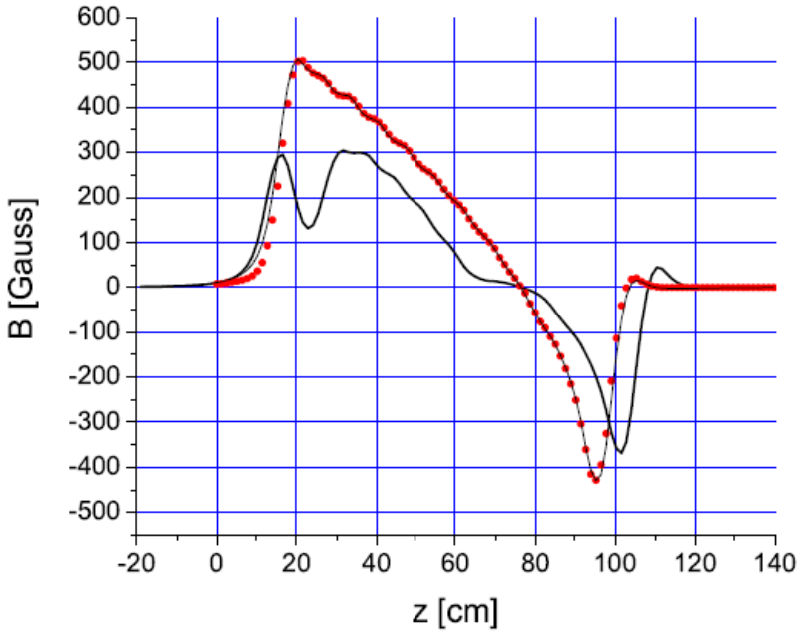

Figure 6.7: Field profile of the zeeman slower. Red dots form the measured profile after the slower was completed. Thick line is the calculated profile for actual currents used in the experiment (adapted from [20]).

The Zeeman slower is a multi coil (modular) spin flip slower. It consists of 13 coils, each one carrying a specific current to create a magnetic field profile as shown in Fig. 6.7. This particular design of the slower has its advantages and disadvantages. The multi coil design gives flexibility in tailoring the magnetic field profile to get the best loading rate in the MOT. However, since it has so many coils, it adds to the number of instruments and hence increases the chances of failure. After 5 years of operation, we had to replace all the power supplies for the coils because they degraded and produced too much noise in the current which the current regulator was unable to correct. To debug such

Coil	Current (A)	Coil	Current (A)
1	3.84	8	0
2	2.25	9	0
3	2.84	10	0.4
4	2.27	11	1.16
5	1.80	12	4.43
6	1.18	13	1.98
7	0.8		

Table 6.2: Currents in different zeeman slower coils.

a problem is not easy since the slower still has an effect but not as big when it works well. We had to eliminate all other, more likely, problems before we finally narrowed it down to the noise in the currents. The slower was built many years ago and the best way to optimize it was to directly look at the loading rate and atom number inn the MOT. In principle, the currents in the coils should never have to be touched after initial optimization. This was true for the most part. Table 6.2 shows the values of currents in different coils. We found that coils at the beginning and end of the slower had the largest effect. The intermediate coils had some effect but not as dramatic as the ones on the ends. The Zeeman slower beam counter propagates the atomic beam. The beam size is about 1.5" at the viewport of the chamber and focuses as it approaches the oven to match the atomic beam divergence. The beam is 620 MHz red detuned from the $|F = 2\rangle \rightarrow |F' = 3\rangle$ transition and carries 40 mW of power. The repump beam, carrying 10 mW of power, is mixed into the slower beam. The polarization of the beams is circular and is optimized by looking at the atom number in the MOT.

6.3.2 MOT

The atoms enter the science chamber where they are captured in a MOT. The MOT consists of three pairs of counterpropagating beams aligned orthogonal to each other and a weak quadrupole magnetic field. The beams are derived from a 1 mm beam that spatially filtered with a pinhole at the focus of a telescope. The exiting beam is expanded by a 63:500 telescope to create a 1" diameter beam. The beam is first split into three beams and then each beam into two more (to create the counterpropagating pairs) using polarizing cube beam splitters. We end up with six beams that are all linearly polarized and the powers in each beam are the same (within 10%). The power in the incoming beam is about 140 mW. As will be explained in later sections, the direction along the cell is heavy with optics due to a number of dichroic mirrors. We thus had to distribute the power in that pair of beams unevenly when it is split so that the powers at the atoms are similiar. This was optimised by looking at the number in the MOT and molasses expansion. Before the beams enter the chamber they pass through a quarter wave plate that makes the polarization circular. The schematic of the MOT beams and the magnetic field is shown in Fig. 6.8.

Getting a MOT for the first time can be tricky at times. Here are a few pointers on how to achieve this:

1. The powers in all the beams should be measured just before they enter the chamber. They should be within 10%. Typically, the intensity of the MOT beams should be twice the saturation intensity of the transition.

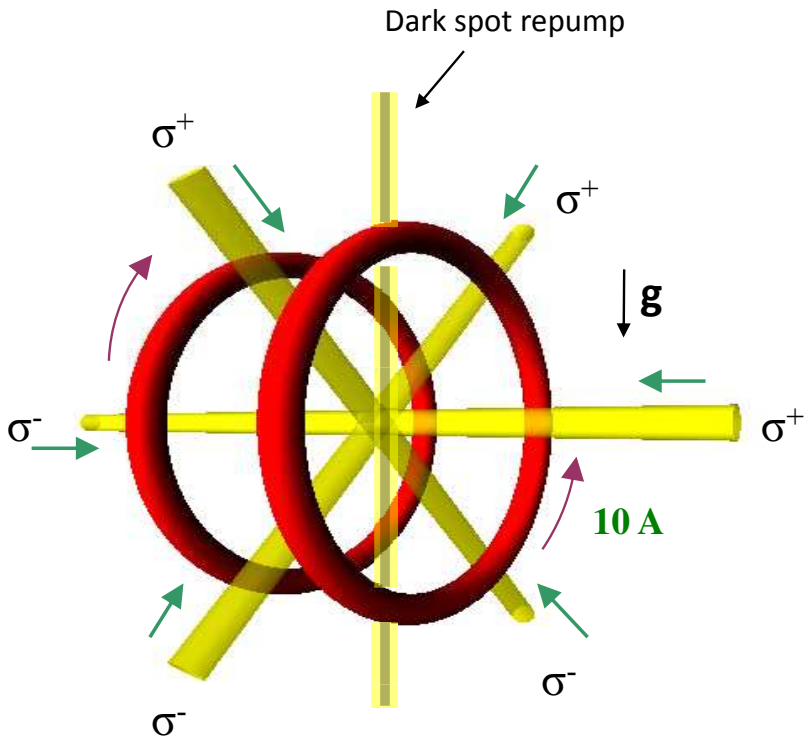

Figure 6.8: Schematic of the MOT.

We had about 20 mW per beam.

2. The polarization of all the beams should be circular with the correct helicity.

3. The repump beam (either co propagating with the MOT beams or a single repump beam) should have the correct frequency. The power for the copropagating repump beam was 30 mW and the beam size was similar to the MOT beam. We found the MOT to be insensitive to the polarization of the repump beam. Our copropagating repump was circularly

polarized whereas our single beam repump was linearly polarized and we did not see any noticeable difference in the MOT.

4. The anti-Helmholtz coils had a gradient of 18 Gauss/cm.

5. The MOT beam are aligned so that the counterpropagating beams are exactly overlapping. This can be achieved by placing a card with a hole at the center on the opposite viewports. The mot beam size is reduced with an iris and the beams aligned so they clear the holes on both the cards. Aligning all the six beams using this method gets us quite close to seeing a good molasses.

6. A laser locked to the atomic transition might not be at the exact transition frequency (only that it is at a very well defined detuning from it) due to the FM lock and saturated absorption setup which add a frequency shift. The AOMs after the laser are set to certain frequencies assuming a particular detuning of the laser from the transition. To account for possible uncertainty in this detuning, we scan the laser by about 300 MHz around the transition (instead of locking the laser). We see a blinking MOT that appears and vanishes as the laser crosses the transition frequency. It is much easier to see a blinking signal in the background of scattered light than a stationary signal. This technique is especially useful to look for molasses in the previous step which is harder to see than a MOT. A detuning of a few MHz from the expected detuning can increase the atom number in the MOT. We do this by changing the offset on the lockin amplifier.

7. Another thing to try, if there is still no MOT, is to flip the direction of current in the quadrupole coils. The direction of the magnetic field has to be set relative to the polarization of the MOT beams and it is much easier to flip the field rather than rotate the polarizations of the six beams [51].

We optimise the zeeman slower beam and MOT beam alignment by looking at the fluorescence from the MOT. To do this, we use a lens close to one of the free viewports (or a viewport through which the MOT is clearly visible even with the presence of other optics around it) to create an image of the MOT. An avalanche photodiode [Hamamatsu, Model: C5460-01] is placed at the image plane to record the fluorescence. In principle, an ordinary photodiode can work but depending on the collection angle of lens. We used both kinds of photodiodes. Before the image falls on the photodiode, we introduce a beam splitter and the reflected image falls on a CCD camera. This is a cheap webcam CCD and its main purpose is to guide us to the position of the MOT that gives best transfer into the magnetic trap.

We would like the MOT beams to be aligned such that the MOT does not get pushed away when the magnetic field turns off during optical pumping ie: the molasses is balanced. This is done by forming a MOT and suddenly switching off the magnetic field. The expansion of the molasses should be symmetric. If the molasses is pushed in some direction it indicated a misbalance of the powers in the MOT beams. If the molasses swirls around it indicates a misalignment of the MOT beams.

After the bright MOT is fully loaded we switch to the dark MOT [52]. The dark MOT has two advantages, it increases the density of atoms and makes the loading into the magnetic trap more reproducible. The density in a normal MOT is limited by reabsorption of photons scattered by the MOT atoms. Consider two atoms, one on the left in the excited state and one the right in the ground state. Lets asssume the atom on the left decays to the ground state by emitting a photon to the right. This gives the atom a momentum kick in the left direction. If this photon is absorbed by the atom on the right, it gets a momentum kick to the right. Thus the process of reabsorption between atoms creates an effective repulsive interaction between atoms and prevents atoms from coming too close to each other. The dark spot addresses this problem by creating a region in the center of the MOT where repump light is absent. The atoms in this region fall into the "dark state" ($|F = 1\rangle$) and do not scatter photons[1]. As a result, they can be more closely packed thus increases the density. The setup for the dark spot is shown in Fig. 6.9. The dark spot is created by gluing a black plastic disc on an AR coated window. To align the dark spot, the dark repump is turned off and the copropagating repump is turned on. This creates a MOT that is imaged by the last lens in the dark spot telescope. The window with the dark spot on it is placed at the position where the image is in focus which, in turn, creates a 1:1 image of the dark spot on the MOT. The dark repump is then turn on and the copropagating repump turned off to get the dark MOT. The correct

[1]The atoms actually do scatter photons at a very low rate (∼10 KHz) from the cooling beam and can be repumped.

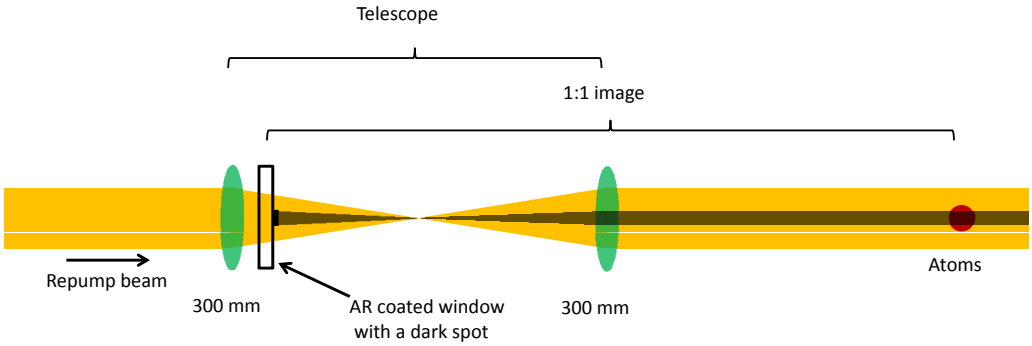

Figure 6.9: Optics setup for the dark spot repump beam.

dark spot size was determined by looking at the difference in the fluorescence level with the dark spot repump always on and blocking and unblocking the copropagating repump. With the copropagating repump off, the atoms are loaded in the dark spot MOT. If the copropagating repump is then suddenly turned on, we can see a jump in the MOT fluorescence level. If the jump is to a value larger than what one would get in the steady state with both repumps on, then the dark spot is having the desired effect of holding more atoms at a higher density. We tried a number of dark spot sizes ranging from 3 mm to 10 mm. We found the best size to be 4 mm.

6.4 Magnetic Trap

The optical plug trap (OPT) was first used by the Ketterle group in MIT for the creation of their BEC in 1995 [53]. It was abandoned by them but was later revived by the Raman group in Georgia Tech where they were successful in producing a sodium BEC with a large number of atoms [54]. Our

trap design is based on theirs and they were very helpful in providing useful information which made it work.

6.4.1 Construction of the coils

The quadrupole coils needed for the trap are the same ones that we use for our MOT. They are made from 1/8" square copper refrigerator tubing with a bore size of 1/16". The tubing was coated with fiberglass for electrical insulation. The inner diameter of each coil was 2.92" and was chosen to be just big enough so it can pass over a 2-3/4" flange (our glass cell was smaller than that so it would easily pass over the glass cell too). The coils were wound on an aluminum cylindrical form which was machined to have the desired ID for the coil. The cylinder was coated with kapton tape to prevent any damage to the fiberglass insulation. After every layer, the windings were hammered in place with a teflon piece to make them compact. The design of the coil form is shown in figure 6.10.

Each coil consisted of 8 layers with 7 turns per layer. The inner 6 layers were used for the magnetic trap and the outer two layers were extra coils in case we needed them later. The coils were made from 15' long pieces of tubing. Each piece was long enough for two layers and was connected independently to the cooling water. The electrical connections were made externally for the different pieces in the desired configuration. After every two layers of tubing, a thin layer of hot epoxy was applied. The epoxy helped in keeping the windings tight and made the whole coil monolithic. The face of the coil touching the chamber was covered with kapton tape for electrical insulation. The coils were

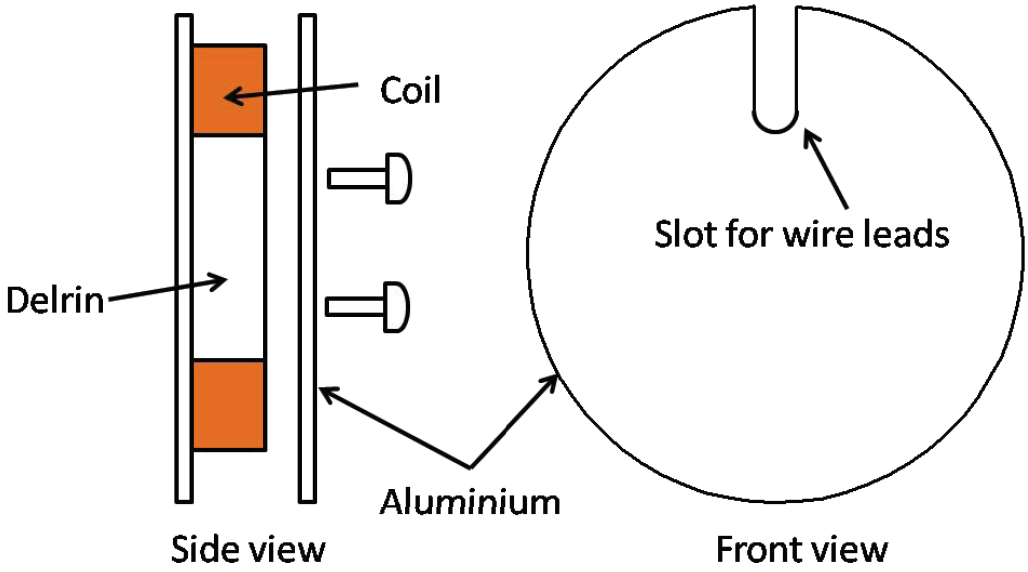

Figure 6.10: Aluminum form used for winding the coils.

mounted on the chamber with 1/2" long standoffs, with 1/4-20 inner threads, that were welded on the chamber. The mounting of the coils for the test setup is shown in figure 6.11.

6.4.2 Water cooling

During normal operation, more than 10kW of heat is dissipated into the coils. To remove this heat the coils were water cooled. The source of cold water is a university supply line at 7°C. An Affinity heat exchanger (Model: EWA-04AA-CE56CB) was used to cool a closed water line which ran through the coils. The flow rate through each of the four segments of wire in a coil was 0.5 L/min at 80 psi water pressure. During normal operation the pumps are on which increase the pressure to 100 psi. The segments are connected in parallel

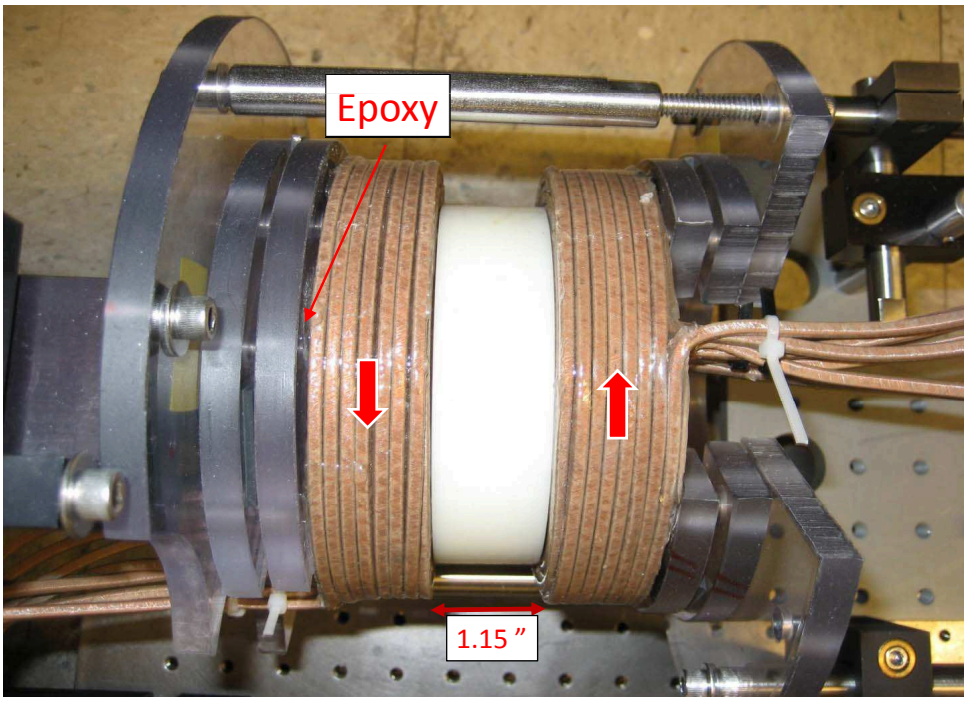

Figure 6.11: Quadrupole coil mounted for testing.

to each other in the water circuit. Part of the cooling water also goes to cool the IGBT and diodes that are part of the electrical circuit and dissipate many tens of watts of power. The closed circuit was filled with distilled water and some ethylene glycol to prevent rusting and clogging of the tubes. Since the coil tubing has such a narrow bore, one has to be careful during construction to avoid any foreign pieces from entering the bore and clogging it. We also included a water filter in the circuit to filter out any particulate impurities. After few years of operation, we can actually see small copper particles stuck in

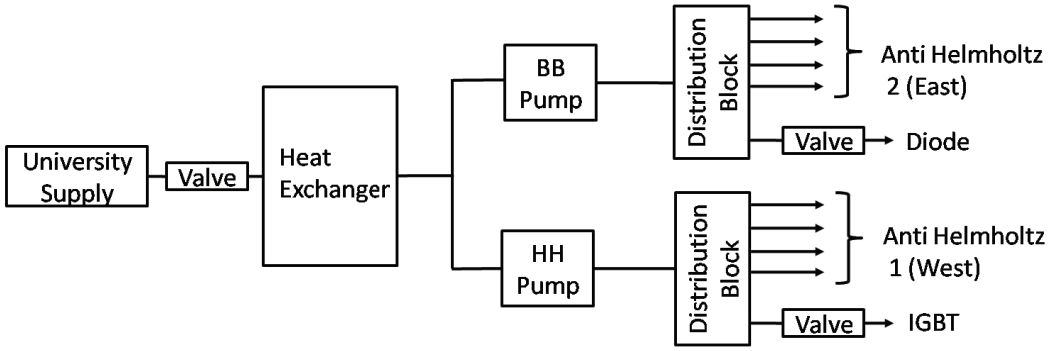

Figure 6.12: Water cooling circuit.

this filter which indicates that the coil does get eroded over time by the flowing water. The flow rate of the university water was very high which caused the temperature of the coils to drop significantly since the water is on even when the magnetic trap is off. To solve this problem, we had a voltage controlled valve in line with the supply water to change its flow rate. In principle, we could have used a PID to regulate the flow rate and keep the coils at a constant temperature. However, at some setting of the valve the water temperature of the coils was always between 18°C and 35°C after continuous operation. This did not seem to affect the performance of the magnetic trap and thus we never implemented the PID.

6.4.3 Electrical Connections

The circuit for the electrical connections to the coils are shown in Fig. 6.13. A high current power supply manufacture by Lambda electronics (Model: ESS 30-500-2-D) is used to drive the coils. It can supply 500 A of current at 30V and regulates the current to 0.1%. The power supply has been very

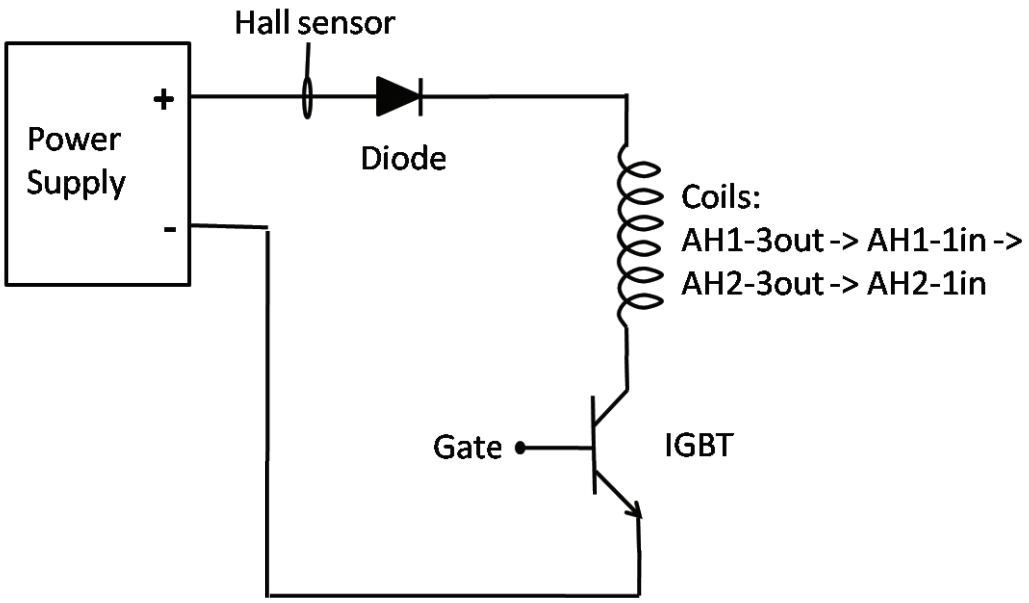

Figure 6.13: Magnetic Trap circuit.

reliable even after daily operation for 6 years without any deterioration in performance. An IGBT (Model: PXR CM600HA-24H) is used to turn off the current quickly. The gate of the IGBT needs to be driven by +24 V when on and -8V when off. A home made circuit was used to achieve this and drive the gate. The forward biased diodes (Model: PXR CS-64-1230 with two in parallel) are for safety and they prevent the back emf of the coils from damaging any electronics during fast turn off. The IGBT is very sensitive to static electricity so we connected a 200 V varistor across the terminals to prevent any high volatge spikes from damaging it. The wires connecting the different components are 3/0 GA welding cables with two cables connected in parallel. The coils and power supply are floating with respect to ground. The

resistance of one coil (plus diode, IGBT and connectors) was 42 mΩ which limited the maximum current to 330 A at 29 V.

6.4.4 Testing of the magnetic trap

Testing the magnetic trap was done prior to installing it on the chamber. The two coils were mounted in a similar geometry as they would be on the chamber. The spacing between the coils was 1.1" which corresponds to the actual spacing between the chamber wall buckets. The magnetic field measurement was done by mounting the Hall probe on a stepper motor and measuring the magnetic field with a Teslameter (F. W. Bell, Model: 9550). The Teslameter had an analog output that was used to record the magnetic field using a computer which made the data acquisition computer controlled. The coils were setup as shown in Fig. 6.14.

The measured magnetic field as a function of distance along the axial direction is shown in Fig. 6.15. The calibration of the field gradient was found to be 1.8 Gauss/cm/Amp. The maximum gradient we could achieve along the axial direction was 615 Gauss/cm at 330A, 30V. At this current, the temperature of the coils increased to 67° C after more than 30 seconds of continuous operation. The switching times of the coils, once mounted on the chamber, were measured as shown in Table 6.3 for the case of switching with the IGBT and the analog input to the power supply. It was important to measure these times after final installation since the vacuum chamber could alter the inductance and hence the switching times.

The turn on time is limited by the power supply and induction of the

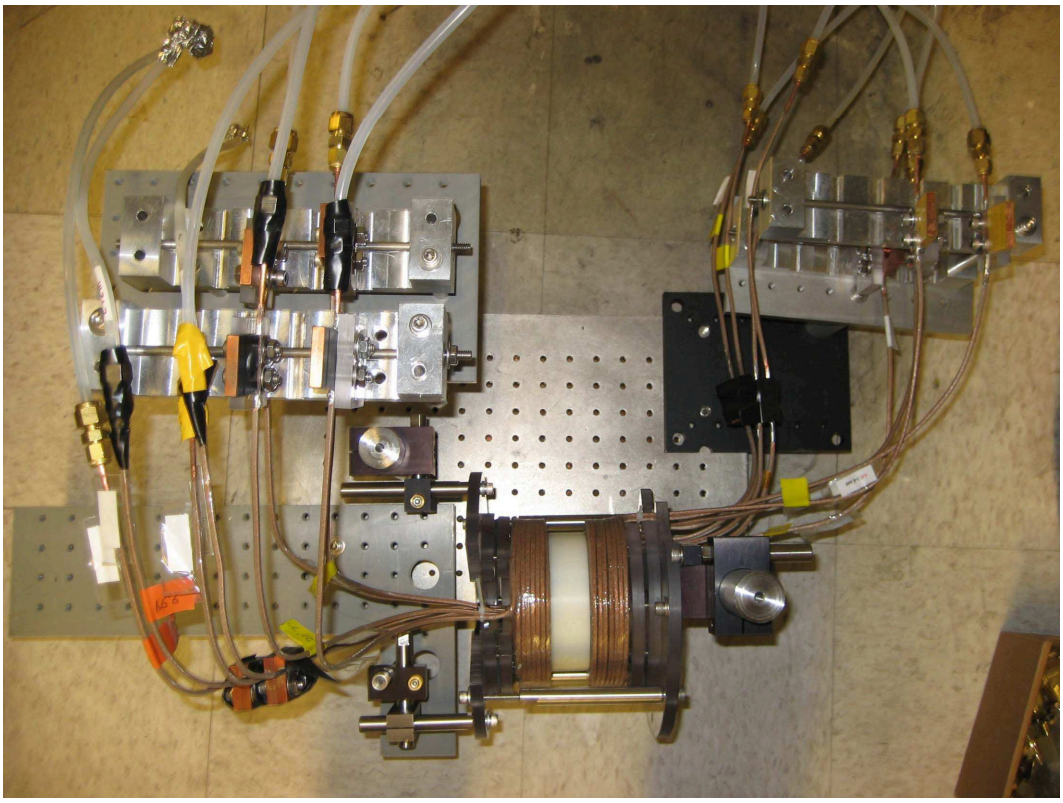

Figure 6.14: Magnetic trap test setup.

coils. The way we improved the turn on time was to to raise the current to twice the desired value for a few milliseconds and then put it to the desired value. This gave a turn on time of 5 ms but it did have some ringing in the current for more than 10 ms. The turn off time with the IGBT was limited only by the coil inductance. When the coils are suddenly turned off using the IGBT, they tend to move axially due to the magnetic force. During tests, the coils jerked by about 1 mm by sudden turn off from 330 A. The rigidity of the test setup was less than what it would be once the coils were mounted on the chamber. The jerking is much less for longer turn off times or smaller

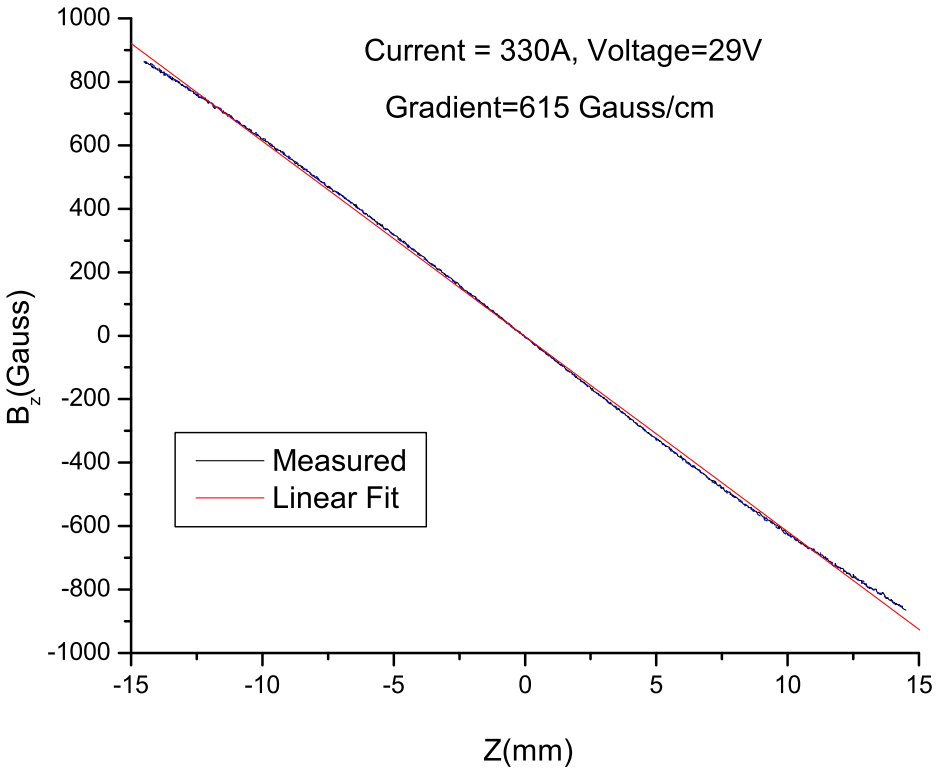

Figure 6.15: Field gradient of the quadrupole trap.

currents. After installation on the chamber the coils still moved during rapid turn off causing a loud clicking sound as they bang against the chamber. We tried to avoid this by decompressing the trap below 150 A before fast turn off (which is necessary for temperature measurements). We could extrapolate the temperature at higher currents assuming an adiabatic decompression which retains the phase space density. Knowing the temperature and number at lower currents allows us to calculate the temperature for higher currents.

In conclusion, the magnetic trap indeed turned out to be as easy to construct as we had thought. The field gradients that we measured were acceptable for a fast evaporation.

6.5 Optical Plug

The quadrupole trap has a zero magnetic field at the center that causes large trap loss (Majorana loss) due to non adiabatic spin flips especially at low temperatures (as explained in section 2.2.1). This "hole" needs to be "plugged" to prevent atoms from reaching the center. This is done using a blue detuned (532 nm) laser beam focused at the center of the trap. We made an initial unsuccessful attempt at doing this and then a successful one.

6.5.1 Initial (unsuccessful) setup

The optical plug in the MIT setup was created using an Argon Ion laser. Argon ion lasers are known to have very bad pointing stability. Any relative motion between the plug beam and the zero of the magnetic field is detrimental to creating a stable trap. In our setup, we used a Coherent Verdi laser that has a much better pointing stability than an Argon Ion laser. However, our laser was located on a different table and the beam traveled for about 6 meters in air before reaching the atoms. This made the pointing worse

	Turn ON	Turn OFF
IGBT	10 ms	120 μs
Analog Input	20 ms	40 ms

Table 6.3: Switching times of the Quadrupole coils.

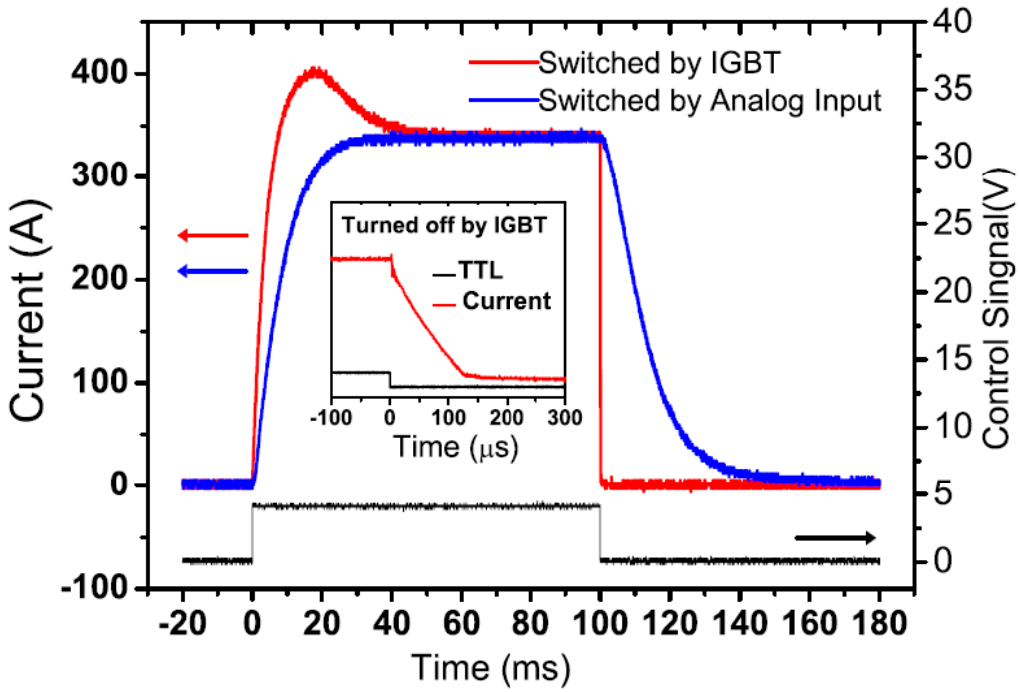

Figure 6.16: Switching time of the quadrupole trap. The curves show the turn on and turn off times for switching with an IGBT or with an analog input that regulates the current.

(probably not as bad as an Aron Ion laser) as will be discussed later. In our first setup, the beam came in the direction perpendicular to the axis of the quadrupole coils. The beam waist at the atoms was 40 μm and the power was 3.5 W. Using Eq. 2.6 for the dipole potential, this gave a well depth of 4.6 MHz, corresponding to 220 μK.

The signature of the plug in this geometry was neither clear nor reproducible. Even 1 μm misalignment of the plug beam would make the plug

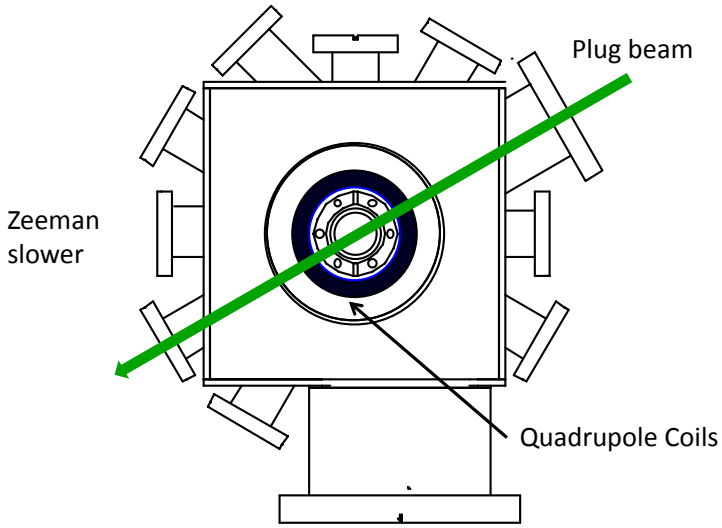

Figure 6.17: Initial direction of the plug beam.

ineffective. There were two main reasons why, we think, the plug along this direction did not work.

1. The plug is perpendicular to the axis of the quadrupole coils and hence it has to counteract the highest magnetic field gradient with its waist which makes the effective well depth along that direction much smaller. Fig. 6.18 compares the effective potential along the weakest direction for the case when the plug is along the axis and perpendicular to the axis (all other parameters being the same). For the same plug power, one creates a trap with 500 KHz depth, away from the center, if the plug is along the axis and no such trap if it is perpendicular to it. This is not a serious problem if one has a lot of laser power to spare (which is rarely the case!).

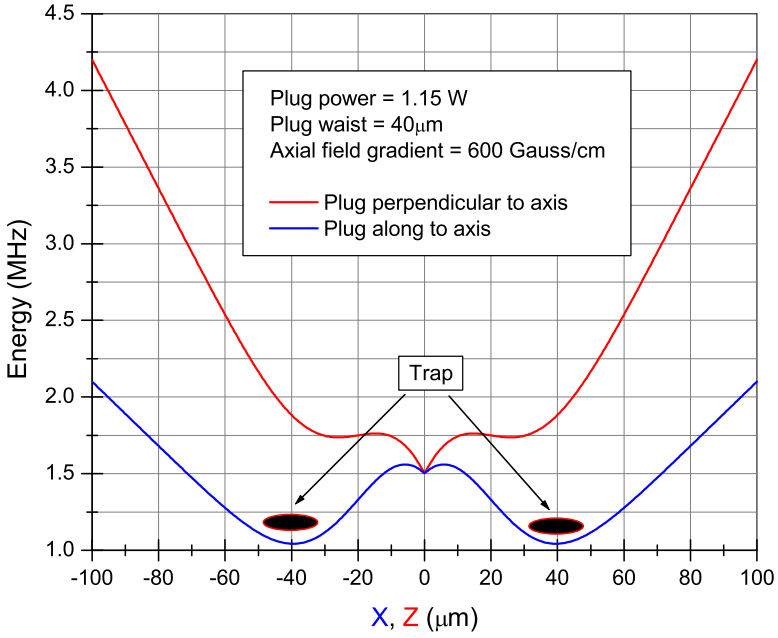

Figure 6.18: Effective well depth of the optically plugged trap with the plug along (blue) and perpendicular to (red) the quadrupole trap.

2. The plug beam laser was 6 meters from the location of the atoms. The beam traversed in air over two different optical tables. We measured the vibration of the plug beam to be $\pm$ 8 μm at the location of the atoms. This was a big problem since it would mean that the plug was moving around the magnetic field zero and not always plugging the hole effectively. The way our vacuum chamber is mounted, vibrations along the axial direction of the trap were more likely than the other two directions. We measured the vibrations of the chamber using an accelerometer and

found it to be 1 μm at 400 Hz. The accelerometer was not sensitive enough at lower frequencies which limited a more precise measurement in the few Hertz regime which is more likely to have higher amplitude for a vacuum chamber.

Having the plug beam coming along the axis of the trap would have definitely solved the first problem. It would also help in solving the second problem since the vibrations of the chamber would now be along the direction of the laser beam. The effectiveness of the plug along this direction extends over almost its Rayleigh length of 9.4 mm. The chamber vibrations would not cause any misalignment between the plug beam and the zero field point along that direction. The pointing stability of the beam itself could have been improved by using a smaller focal length focusing lens or by using an optical fiber. We were limited by our chamber design and the smallest focal length lens we could use was 500 mm. Single mode optical fibers in the visible region for many watts of power are not available and one has to resort to photonic crystal fibers which might be a viable option.

6.5.2 Final setup of the plug beam

The final orientation of the plug beam is shown in Fig. 6.19. While this made the optical plug trap (OPT) work much better, it caused some other complications during our attempt to transport the atoms to the cell (see section 6.10.3). The optics setup for the plug beam is shown in Fig. 6.20.

The beam passes though a 80 MHz Acousto Optic Modulator (IntraAc-

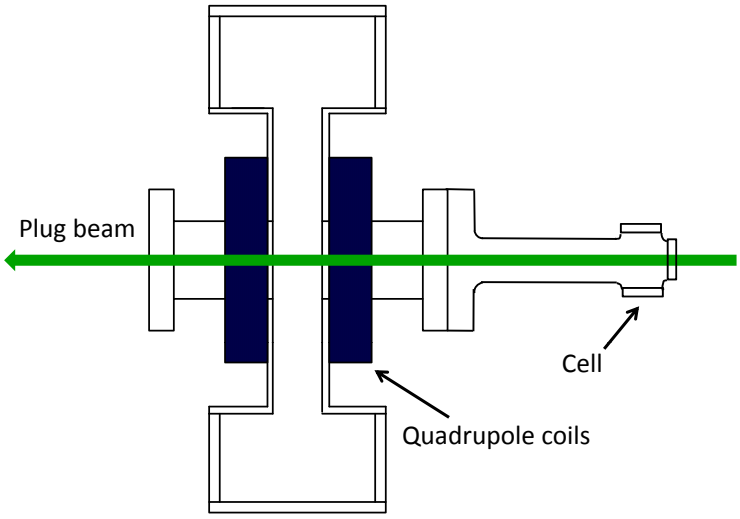

Figure 6.19: Final direction of the plug beam.

tion, model: ASM 702-8) which is used to control its power (the zeroth order of the AOM is used for creating the endcaps of our 1D box which are described in section 6.11.2). The beam then passes though a shutter and a 63:350 telescope. A 200 mm lens is used to focus the beam and the focal spot is imaged onto the atoms using a 100 mm lens. The reason this setup, eventually, became so complicated was because we use that direction for the MOT beams, the plug beam and the tweezer for transporting the atoms to the cell. Mixing all these wavelengths together with each beam creating a different spot size at the atoms was a challenge in itself. The plug waist at the atoms was 42 μm. With 3.5 W of power it gives a well depth of 4.2 MHz (corresponding to $U/k_B = 200$ μK. The combined potential in the optical plug trap is shown in figure 6.21. The potential is cylindrically symmetric with a minimum at a magnetic field of 1.5 Gauss. A BEC in such a trap would be toroidal in shape

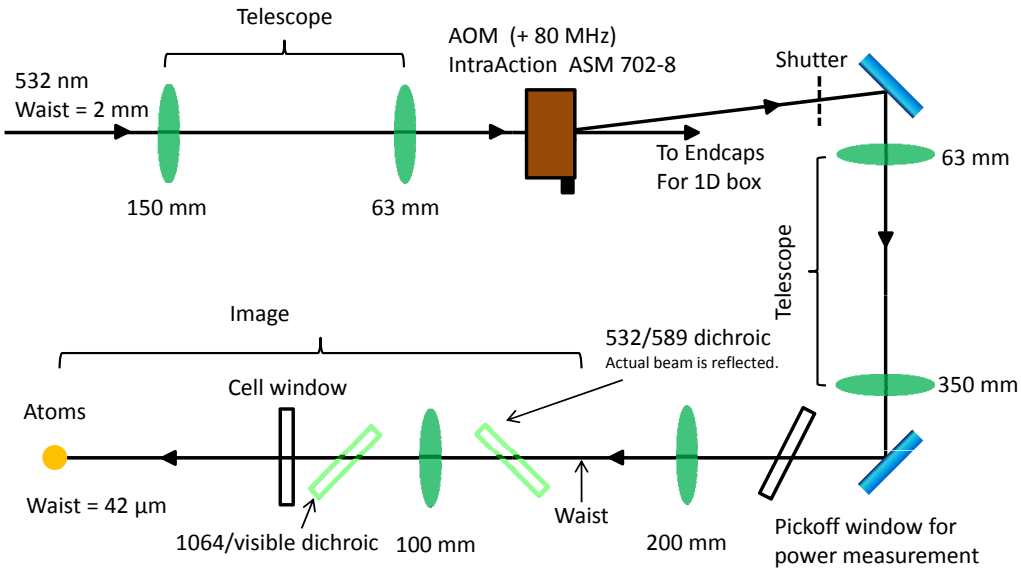

Figure 6.20: Optics setup for the plug beam.

but gravity breaks the cylindrical symmetry causing most of the atoms to stay below the plug. The precise shape of the plug beam at the atoms affects this potential significantly.

6.5.3 Alignment of the plug beam

Prior to aligning the plug beam, it was important that the evaporation (section 6.6) be working. The plug is not strong enough to have a visible effect on atoms at MOT temperature. The first step was to evaporate the atoms to 1760 MHz (equivalent to 3.8 MHz if doing evaporation within the same hyperfine manifold) and taking a picture with the trap on. We note the position of the center of the cloud. We then take a picture of the plug beam on

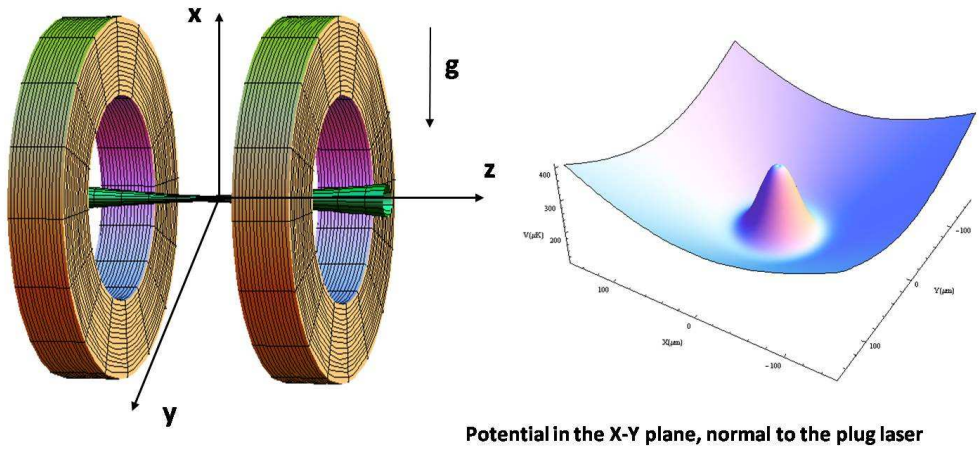

Figure 6.21: Potential along the radial direction of a OPT. The trap parameters are: B'= 300 G/cm, plug beam waist = 40μm and plug beam power = 3.5 W.

the camera and put it at the same position as the center of the cloud. One has to be careful at this stage and block all the light from the plug beam before it reaches the camera to avoid damaging the camera. This was done by first using two dichroic beam splitters that transmit 589 nm (imaging beam) and reflect 532 nm (plug beam). The only company we found that could make dichroics for such close wavelengths for a reasonable price and lead time was CVI (part no: LWP-45-Rs-532-Tp-589-PW-1025-C). In addition, we also put a Schott color glass filter (CVI part no: CG-OG-590) to block out the remaining green light. In all, this gives us more than 8 orders of magnitude attenuation of the plug beam and a factor of 2 attenuation of the imaging beam. If we want to see the plug beam on the camera we change the power in the plug beam and

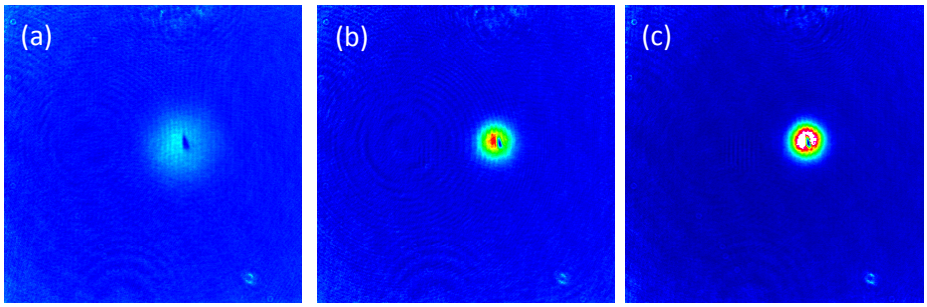

Figure 6.22: Absorption image of the plug beam piercing through the cloud of atoms. (a) shows the initial sign of the plug as seen after 3 ms expansion of the cloud. The image of the cloud after 1 ms expansion is shown when the plug is away (b) and close to the center (c) of the quadrupole trap. The field of view is 6 mm.

replace the last filter by one with less optical density for 532 nm (CVI part no: CG-OG-570). Next, we do the same evaporation sequence but take a picture of the atoms with the plug beam on at full power. The last image should have a clear sign of the plug beam pushing away the atoms and creating a hole in the cloud as shown in Fig. 6.22 (a). We expand the cloud for 3 ms before taking the picture to increase the search area. Once the plug beam is located, we can maximize the number by tweaking its position as shown in Fig. 6.22 (b) and (c). It is clear from the pictures that the shape of the plug does not look circular at the atoms. This is because the plug beam comes at an angle of about 3.5° with respect to the trap axis. The beam falls off center on the 100 mm 2" diameter achromatic lens which distorts the beam profile. We had to align the plug at an angle to keep the central region of the optics and cell window free, so it does not distort the tweezer beam that enters the chamber

through the same port (see Fig. 6.41). The focus of the plug beam can be aligned by minimizing its size on the camera. This works only if the camera is precisely (within a distance much smaller than the Rayleigh length of the plug beam) at the image plane of the atoms. Generally, this is not the case and it is necessary that the plug focus be optimized to get the maximum atom number.

6.6 Evaporative Cooling

In a magnetic trap, evaporative cooling is done by forcing RF transitions that put the high energy atoms in the anti-trapping state and are thus removed from the trap. The remaining atoms re-thermalize and reach a new lower temperature. Repeating this process allows one to reach lower and lower temperature and higher phase space density. The energy levels of the different magnetic sublevels in both the hyperfine ground states of ^{23}Na are shown in Fig. 6.23.

The atoms in the OPT are in the $|F = 1, m_F = -1\rangle$ state. Most commonly, evaporation is done by inducing transitions between the Zeeman levels of the same hyperfine state (blue transitions) using radio frequency (RF) photons. The atoms absorb two photons to reach the $|F = 1, m_F = +1\rangle$ state, which is anti-trapping, and are ejected out of the trap. For a certain RF, only atoms at a specific magnetic field are in resonance and undergo this transition. The hotter atoms explore regions of higher magnetic field in the trap and thus one can tune the RF to selectively target those atoms to be ejected from the

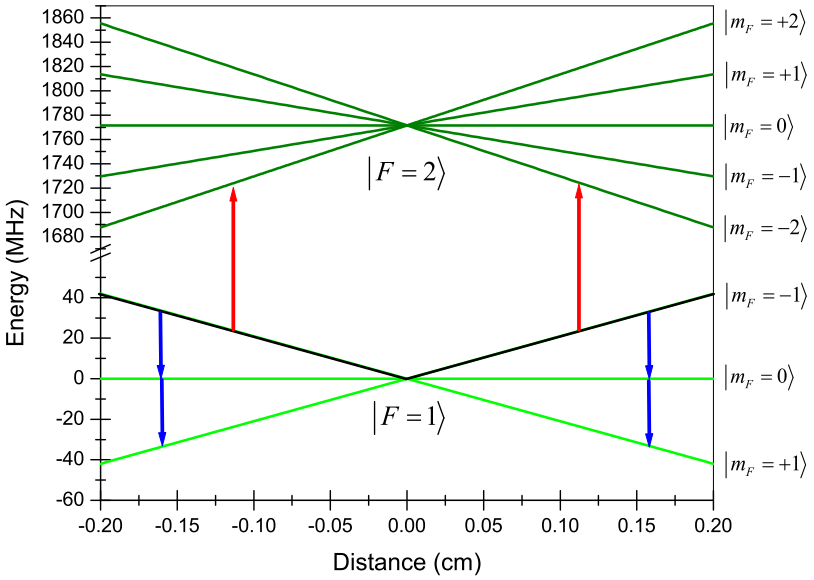

Figure 6.23: Energy dependence of the ground state Zeeman levels of ^{23}Na in a quadrupole trap with a gradient of 300 Gauss/cm. Blue arrows represent the transitions for RF evaporation and the red arrows for microwave evaporation.

trap. To do this, one needs radio frequencies of the order of 10's of MHz. At these frequencies, RF radiation is extremely notorious. A lot of RF power gets reflected back from the RF antenna and the part that does get radiated, interferes with other electronic equipment. Fig. 6.24 shows the measured reflected power as a function of frequency. We found that more than 50% of the incident power was reflected back from the antenna. The fact that the coupling is bad is not surprising since there is a big mismatch in impedance going from the BNC cables to the RF antenna inside the vacuum chamber.

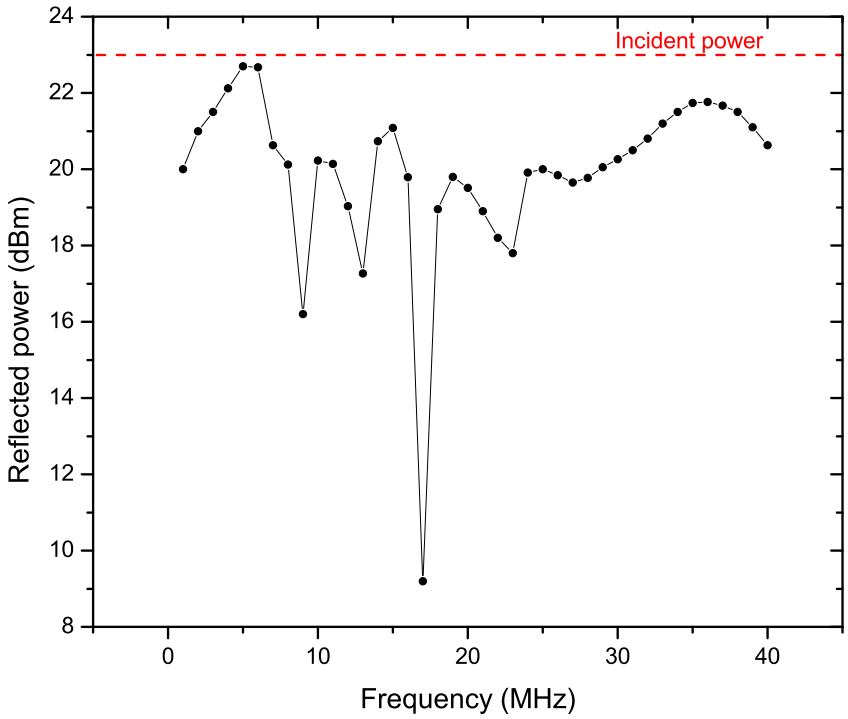

Figure 6.24: Measured reflection of RF power from the coils.

The wavelength of 10 MHz radiation, for example, is 10 meters which is much larger than our antenna size. For maximum radiative output the antenna size should be of a similar order as the wavelength. Consequently, one needs to put many watts of RF power to have suffucient radiation in the chamber for evaporation. In addition to this, the metallic chamber acts like a shield around the antenna making its behavior even more complicated. The leaking radiation affects many devices. Some of the effects that we have have seen because of this RF are:

- False triggering of the interlock circuit that turns off the power supply.
- Noise in the current of the magnetic trap.
- Flickering of ion gauges.

Some of these problems can be eliminated by introducing a RF filter circuit inside the device to prevent it from false triggering. The filter circuit is shown in Fig. 6.25. This filter is used before the input terminals of an OpAmp to prevent the RF from reaching the OpAmp. The RF that reaches the OpAmp can get rectified and appear at the output as a voltage offset. This voltage offset is difficult to eliminate. At certain resonance frequencies (17 MHz) we saw an abrupt loss of most of the atoms from the magnetic trap. Such resonances are known to occur and typically you can skip these resonance frequencies during the evaporation ramp. We found too many of these resonances and decided to find an alternative to conventional RF evaporation. Our approach was to use microwaves to drive a transition between zeeman levels of different hyperfine states. In Fig. 6.23 these transitions are marked in red. The atoms are driven from the $|F = 1, m_F = -1\rangle$ state to $|F = 2, m_F = -2\rangle$ state which is anti-trapping. Such inter-hyperfine state transitions have been used previously to carry out evaporation [8, 55]. The wavelengths for these transitions are much smaller resulting in a higher coupling efficiency. We couple more than 90% of power into the antenna. The radiating microwaves have almost no effect on nearby electronics and since the transition to the anti-trapping state happens in just one photon, it is more efficient.

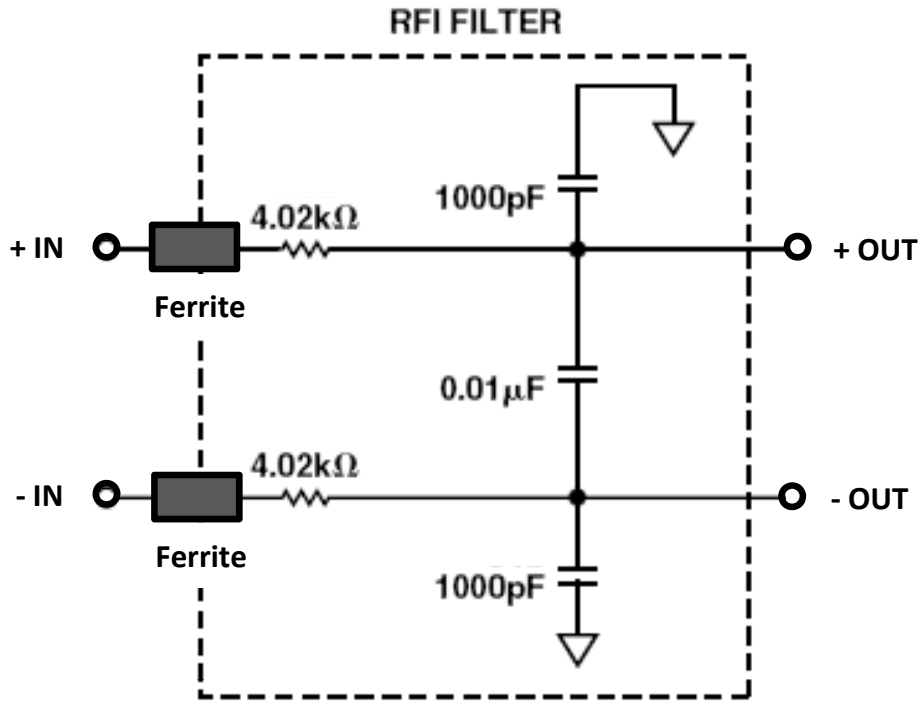

Figure 6.25: Filter circuit used to remove RF interference at the input pins of OpAmp (adapted from Analog Devices Application Note: AN-671).

The RF coils for evaporation are installed inside the vacuum chamber. The original design for holding the coils consisted of threaded 8-32 screws welded inside the chamber on which the wire would be wound and kept in place using nuts. However, during electropolishing the threading on the screws was completely dissolved. We had to come up with a new design which is shown in Fig. 6.26. We have two coils each with 6.5" x 1.5" rectangular shape and a single turn. Each coil is made from 0.01" OD kapton coated wire and wound on

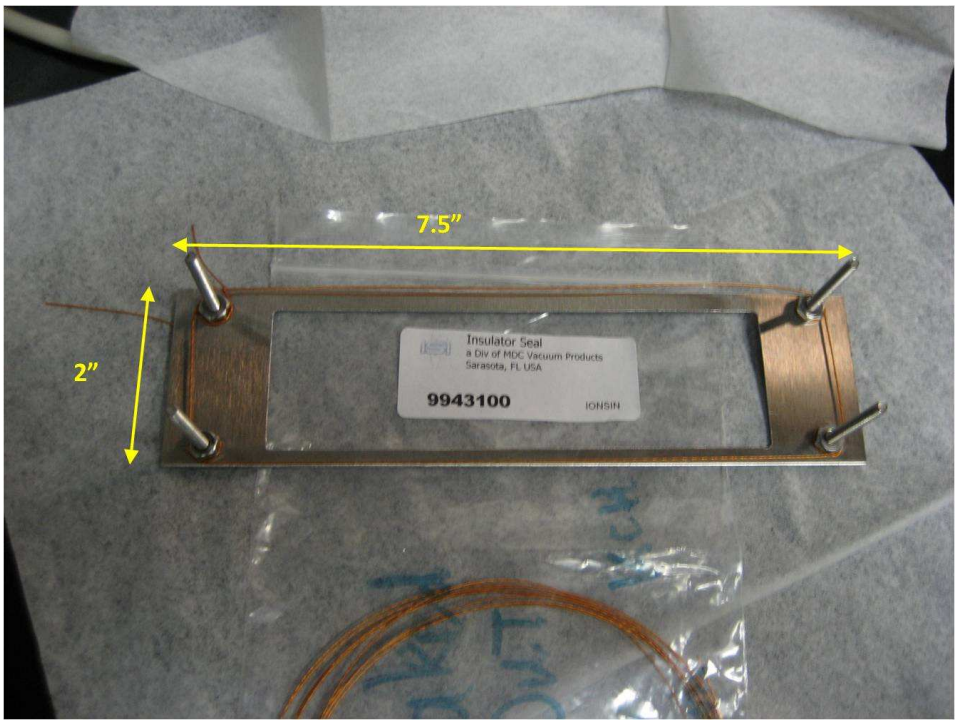

Figure 6.26: Picture of the RF coil and holder.

a rectangular stainless steel frame. The two frames are held together using long threaded screws. The holder had two protrusions at the center and it stayed in place when these clicked into the center bucket ports of the chamber. The holder was held in place by the elasticity of the 304 stainless steel. The coils were connected to electrical feedthroughs with barrel connectors. All parts of the assembly were UHV compatible. While the design itself worked, it would have been better to have more turns of wire and a thicker wire for better impedance matching.

Microwave evaporation requires the RF frequency to be swept around 1771.6 MHz, which is the hyperfine splitting in the ground state. Unlike

ordinary RF evaporation, the frequency has to be swept *up* during microwave evaporation (as can be seen in Fig. 6.23). Also, the frequency range has to be 3 times that used for ordinary RF evaporation to have similar results since the slope for the $|F = 2, m_F = -2\rangle$ state is twice that of the $|F = 1, m_F = -1\rangle$ state. Typically, the RF is swept from 80 MHz to 1 MHz. For microwaves we have to sweep from 1530 MHz to 1770 MHz. In addition to this, we would need a programmable sweeper which would allow us to change the ramp time, add more ramps, etc. Programmable frequency sweepers in this range are very expensive. Luckily, we found an old frequency sweeper (HP, Model: 8340B) that could do the job, however, it could not do more than one ramp. So we decided to use that as our first evaporation ramp and then switch over to a DDS and mix it with a local oscillator to finish the evaporation. Our DDS could go only up to 130 MHz so we could not use it for the complete evaporation sequence. The circuit used to drive the RF coils is shown in Fig. 6.27. Using a frequency mixer to generate microwaves had one disadvantage that it created sum and difference frequencies. For example, mixing the local oscillator at 1640 MHz and the DDS at 100 MHz created two equally powerful frequency components at 1540 MHz and 1740 MHz. The higher frequency component acted like the leading evaporation knife and the lower frequency accompanied it but did not do any evaporation since those frequencies were already swept by the leading frequency. In addition to this, the mixer also produces higher order frequencies. These frequencies and the relative amplitudes are shown in Table 6.4. The higher orders were too weak to cause any problems.

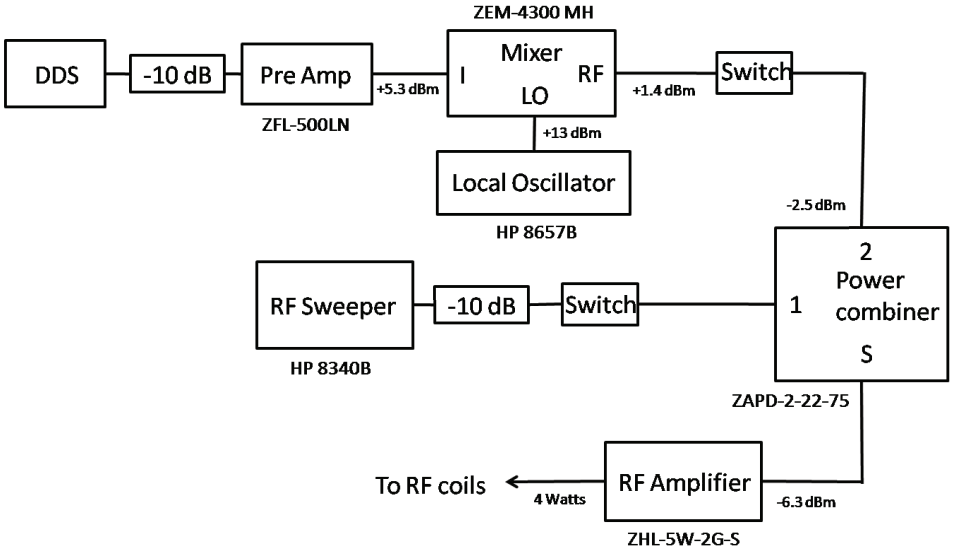

Figure 6.27: Circuit for microwave evaporation.

Frequency (MHz)	Relative Amplitude
1640	-15 dB
1630, 1650	0 dB
Higher Order	-22 dB

Table 6.4: Amplitude of different modes after the frequency mixer. The local oscillator was at 1640 MHz and the DDS at 100 MHz.

6.7 Absorption Imaging

Towards the end of the experimental sequence, the atoms are detected using absorption imaging. The absorption imaging beam is on resonance with the $|F = 2\rangle \rightarrow |F' = 3\rangle$ transition. To get a high optical density, each atom needs to scatter multiple photons from the imaging beam which means that the atoms that fall into the $|F = 1\rangle$ dark state need to be pumped back to the $|F = 2\rangle$ state. We thus need repump light to be on during imaging. This

repump comes from the six directions of the MOT beams. It is better to have the repump not come along the imaging beam and hit the camera since it makes the signal to noise worse. After the first image is taken, all trapping potentials are turned off and the atoms leave the trap. Following this, another image is taken without atoms. Finally, the last image is taken with the camera shutter closed to get the dark image. All images are recorded as bitmaps and false color is added during processing. The last image is subtracted pixel by pixel from the previous two images and the the second image is subtracted from the first to extract the signal due to absorption. This procedure cancels out the common mode noise from spatial inhomogeneity of the plug beam intensity. The optical density can be obtained by taking the logarithm of each pixel in the absorption image. The optical density is proportional to the atomic density of the cloud. This along with the distance calibration on the CCD and the probe beam detuning allows us to calculate the spatial density profile of the atomic cloud and the total atom number. During imaging, the direction along the imaging beam gets integrated and we end up with a 2D density profile (also called the column density).

The imaging system setup is shown in Fig. 6.28. The imaging beam has a power of 10 mW and is about 0.5" in diameter. The first 150 mm lens (achromat, 2" OD) creates a 1:1 image of the atoms which is relayed on to the CCD camera (Apogee, Model: AP7P) with unit magnification by a 75 mm lens (achromat, 1" OD). The focal length of the first lens decides the resolution of our imaging system. It is easy to magnify the image by using a different lens before the CCD but that does not always improve the resolution. For the

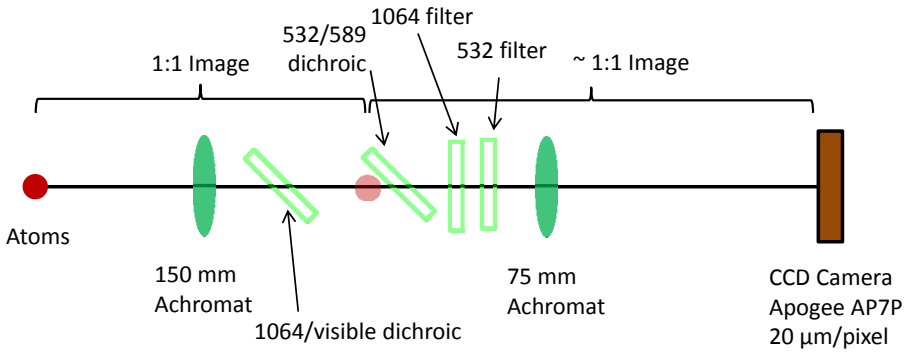

Figure 6.28: Setup for the imaging beam in the chamber.

most part we worked with a resolution of 20 μm/pixel.

6.8 Bose Einstein condensate

A gas of cold atoms undergoes a phase transition to a BEC when the phase space density is close to unity. An important question to ask as we optimize evaporations is: *what is the signature of a BEC?* In order to answer this we first need to understand how a BEC can be modeled and then derive the observable effects from it. A BEC can be described as an interacting gas with two-particle contact interactions (it costs some energy to put two particles at the same position). This would be a terribly complicated problem to solve, since we would have to take into account all the million or so atoms to obtain the complete description. In order to make life simple, we make the mean field approximation where we take a representative particle in a BEC and assume that it sees an average potential energy due to rest of the atoms in the BEC. The Schroedinger equation for the BEC (called the Gross-Pataevskii equation)

is written as [56]:

$$\left[-\frac{\hbar^2}{2m}\nabla^2 + U(\mathbf{r}) + U_0|\psi(\mathbf{r})|^2\right]\psi(\mathbf{r}) = \mu\psi(\mathbf{r}) \tag{6.1}$$

The atomic interaction strength is $U_0 = 4\pi\hbar^2 a/m$ where a is the s-wave scattering length of atoms and m is the mass of the atom. μ is the chemical potential of the BEC. The interaction energy term is proportional to the modulus squared of the wavefunction which is the probability density. In the limit of a pure BEC, the kinetic energy term is negligible and Eqn. 6.1 can be solved easily for the density as:

$$n(\mathbf{r}) = |\psi(\mathbf{r})|^2 = (\mu - U(\mathbf{r}))/U_0 \tag{6.2}$$

In a harmonic trap, the density profile looks like an inverted parabola which is the shape of the trapping potential. Substituting $U(\mathbf{r})$ with energy in a harmonic trap gives:

$$n(\mathbf{r}) = (\mu/U_0)(1 - \sum_{i=1}^{3} \frac{r_i^2}{R_i^2}) \tag{6.3}$$

where the cloud size in a particular direction defined as the Thomas Fermi radius is:

$$R_i^2 = \sqrt{\frac{2\mu}{m\omega_i^2}} \tag{6.4}$$

The chemical potential in a harmonic trap can be shown to be [57]:

$$\mu = \frac{1}{2}\hbar\bar{\omega}\left[15\frac{N_0 a}{(\hbar/m\bar{\omega})^{1/2}}\right]^{2/5} \tag{6.5}$$

where N_0 is the number of atoms in the BEC and $\bar{\omega}$ is the geometric mean of the trapping frequencies. Since the mean field energy is a form of potential

energy, its derivative gives a force which is essentially proportional to the density gradient. If the trap is anisotropic, which is usually the case in a magnetic trap, the force due to the mean field energy is anisotropic too. Moreover, if the trapping frequency is higher, the cloud size along that direction is smaller creating a larger density gradient and a larger force. Consider the case of a BEC in such a trap where we suddenly switch off the trap to let the BEC expand freely. The direction that was tightly confined expands with a larger force compared to the direction that was weakly confined. Thus during expansion one can see the aspect ratio of the cloud changing from one direction in the trap to the opposite direction after expansion. The equations that govern this expansion when released from a cigar shaped trap (cylindrical symmetry) are given by [58]:

$$\begin{aligned} R_{x,y}(\tau) &= R_{x,y}(0)\sqrt{1+\tau^2} \\ R_z(\tau) &= R_z(0)(1+\lambda^2(\tau \mathrm{arctan}(\tau) - \ln\sqrt{1+\tau^2})) \end{aligned} \tag{6.6}$$

where $\tau = \omega_\rho t$ and $\lambda = \omega_z/\omega_\rho$. This anisotropic expansion is an important signature to look for when creating a BEC.

Another signature of a BEC is the appearance of a bimodal density distribution. Thermal atoms have a Gaussian velocity distribution which is reflected in the density distribution after free expansion. As seen above, the shape of a BEC remains parabolic even after expansion. If the BEC fraction in the trap is very small, this appears as a central parabolic peak due to the BEC surrounded by a background Gaussian distribution due to the thermal atoms.

6.8.1 Sequence optimisation to produce a BEC

The bright MOT captures about 3×10^9 atoms in 5 seconds. This is followed by a 50 ms loading time into the dark MOT where the copropagating repump is turned off. We pump any residual atoms into the F=1 state via optical pumping where all repump light is turned off and only the cooling light is on for 0.5 ms. After this stage, all the lights are turned off and the atoms are loaded in the magnetic trap. We transfer about 8×10^8 atoms to the magnetic trap. The catching current is 100 A (corresponding to 186 G/cm). The trap is then compressed to 320 A (600 G/cm) in 0.5 sec. The temperature of the atoms at this stage is 600 μK, the collision rate is 85 Hz and the phase space density is 1.1×10^{-6}. The phase transition to Bose Einstein condensation occurs when the temperature of the atomic sample falls below the critical temperature. This critical temperature is of the order of 100 nK and depends on the confinement parameters and the number of atoms in the trap. To reach this temperature, it is necessary that evaporative cooling enters the so called 'runaway evaporation' regime. Two things happen during evaporation. First, the temperature of the cloud decreases, increasing the density and hence the collision rate (which is important for rapid rethermalization). Second, some atoms are lost, reducing the density and decreasing the collision rate. These two competing processes have to be optimized such that the former dominates the latter. We are then in the runaway regime. The critical temperature is not absolute and depends on the number of atoms itself and hence a good number

to monitor during evaporation is the phase space density which is defined as:

$$PSD = n\lambda_{DB}^3 \tag{6.7}$$

where n is the density of atoms and λ_{DB} is the thermal De Broglie wavelength defined as $\lambda_{DB} = \sqrt{2\pi\hbar^2/mk_BT}$ where m is the mass and T is the temperature of the atoms. In a 3D harmonic trap, the gas undergoes the phase transition when the phase space density exceeds 2.7 [57]. The initial phase space density in the magnetic trap is 1.1×10^{-6}. As a rule of thumb, one should approximately gain two orders of magnitude in phase space density for every order loss in the atom number. In magnetic traps, the collision rate is in the 10's of Hertz and typical evaporation times in 10's of seconds. This requires the lifetime in the magnetic trap to be long. Fig. 6.29 shows the measurement of lifetime of atoms in our magnetic trap. The lifetime is about 120 seconds and is limited by the background gas pressure in the vacuum chamber which is in the low 10^{-11} Torr region. As we change the temperature of the atoms in the oven (as the oven begins to empty out), this pressure can change and affect the lifetime but it is always more than 60 seconds.

During first few tries of measuring the lifetime we found that the lifetime was only about 15 seconds. On evaporation, we were expecting the number and temperature to go down as we increased the microwave frequency. Instead, we found that evaporation actually happened when we go down in frequency. The frequency values did not match the ones we expected. This was a big surprise and also an indication that the atoms might not be starting in the correct magnetic state. After more investigation we found some part of

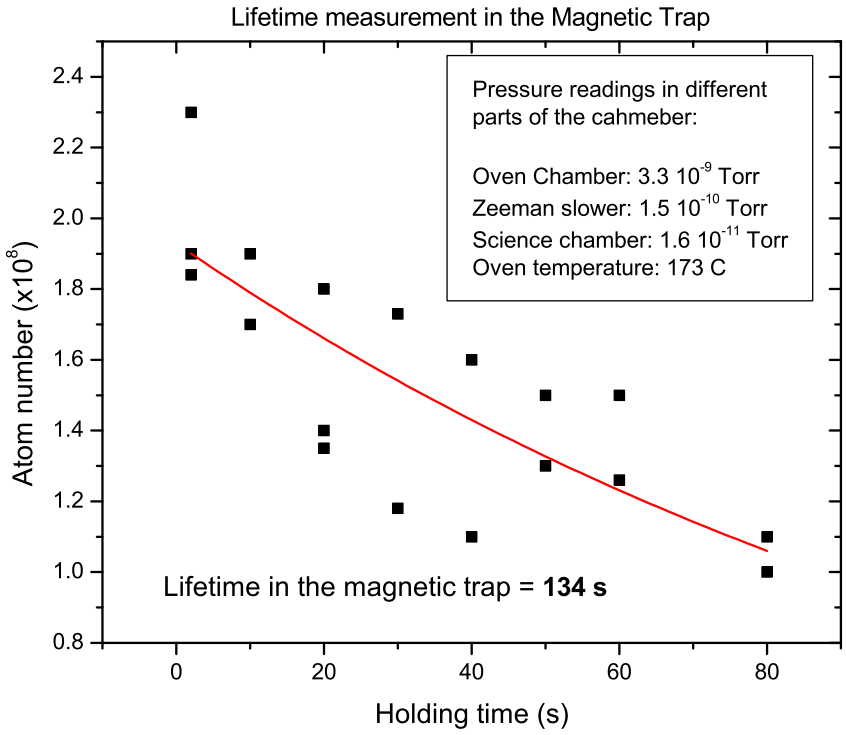

Figure 6.29: Lifetime of atoms in the magnetic trap.

the repump light leaking during the optical pumping stage. As a result, we were capturing atoms in the $|F = 2, m_F = +2\rangle$ and $|F = 2, m_F = +1\rangle$ states in our magnetic trap. The lifetime of these two states, if trapped together, is very small due to strong (two-body) spin relaxation [59]. The evaporation was caused due to the $|F' = 2, m_F = +2\rangle \rightarrow |F = 1, m_F = +1\rangle$ transition. The leaking repump problem has been talked about in many theses before and almost everyone seems to have done this mistake at least one. It is a very common problem because the optical pumping typically lasts for a millisec-

	Atom number	Phase Space Density
Initial value in Magnetic trap	8×10^{8}	1.1×10^{-6}
After 1^{st} stage	4.5×10^{7}	2.6×10^{-2}
After 2^{nd} stage	2×10^{6}	> 1 (BEC)

Table 6.5: Cloud properties after different stages of evaporation.

ond. The repump should be completely off before this which. While this is easy to do when controlled by a computer, it still has to be checked very carefully. The TTL gate on the AOM driver, typically, does not turn off the RF to the AOM completely (attenuation is typically 40 dB). The leaking RF is enough to let out some repump light which can cause problems. One needs to put a shutter to physically block the beam. The delay of this shutter has to be taken into account to make sure the repump is off in time.

Once these problems were fixed we saw a beautiful signal of evaporation by microwaves. To optimize the evaporation we used a number of ramps at first. If we obtained 2 orders of magnitude in PSD for every order of magnitude in number (or scaled accordingly), we moved on to the next step. Finally, however, we settled with just two linear ramps in frequency. The frequencies and cloud parameters after every ramp are shown in Table 6.5.

The two knobs we used to optimize evaporation were the ramp time and the start and end frequencies of the ramp. Having a long lifetime in the magnetic trap helps enormously since you can do longer ramp times to make the evaporation work better. As we go lower in temperature the density of the cloud increases enormously. If left unchecked, it causes a big loss in atom number due to inelastic three body collisions. This happens when three atoms

Evaporation	Ramp Time	Frequency	Quadrupole current
Before Evaporation			320 A
1^{st} stage	20s	1531 $\rightarrow$ 1759.6 MHz	320 $\rightarrow$ 120 A
2^{nd} stage	7s	1759.6 $\rightarrow$ 1768 MHz	120 $\rightarrow$ 100 A

Table 6.6: Parameters during different stages of evaporation.

collide together (three body process) forming a weakly bound dimer of two molecules and the third atom taking away the excess kinetic energy. All three atoms are lost in this process. An important criterion for evaporative cooling to work is high rate of elastic (good) collision and low rate of inelastic (bad) collisions. Inelastic losses prevent many magnetic sublevels in atomic species and almost all molecules from being evaporatively cooled. To overcome these losses the magnetic field gradient is reduced during evaporation so as to keep almost a constant collision rate and moderate densities ($\sim 10^{12}$ atoms/cm^3). The magnetic field gradient and the evaporation frequency are both changed simultaneously. The values of these for different ramps are shown in Table 6.6.

The experimental sequence tracking a few main parameters is shown in Fig. 6.30. The plug beam is turned on after the optical pumping stage and stays on for the rest of the sequence. The total evaporation time is 27 s. As can be seen, a large chunk of time is taken up by our camera which takes 8 seconds to transfer each picture. We take the dark picture (with the camera shutter closed) only once and store it since it is almost constant over time. We then have to take only the first two pictures which reduces our per shot run time.

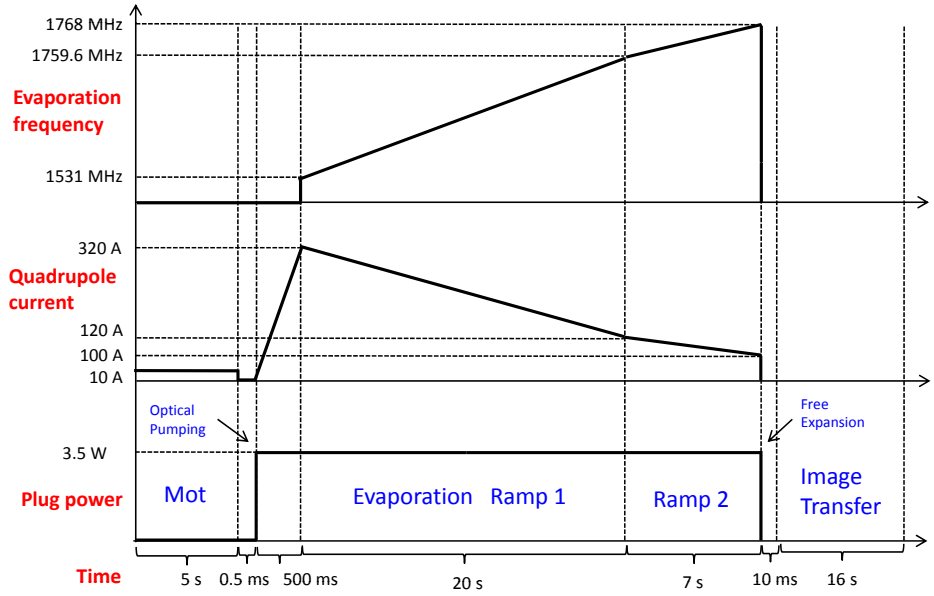

Figure 6.30: Experimental timing sequence.

Continuing evaporation with the optimized sequence allowed us to reach the critical phase space density to create our first BEC of 5×10^5 atoms on September 30^{th} 2007 . We found that a reliable method to look for a BEC was to allow longer and longer expansion times after the trap is turned off. Thermal atoms have a lot of kinetic energy and in a few milliseconds the cloud becomes too sparse to be seen by absorption. As the temperature decreases, the absorption image can be taken for longer expansion times since the cloud does not spread as much and retains it density. Beyond 15 ms of expansion (which depends on the specifics of the imaging setup) we could barely image the cloud only if it was a BEC. For nearly pure BEC's we could expand for as long as 20 ms after which point the atoms went out of our field of view. We

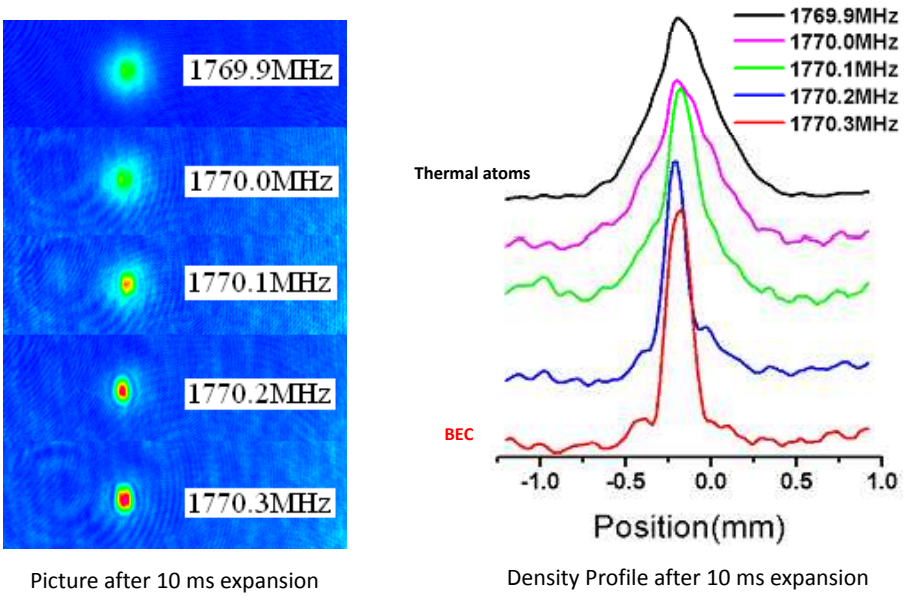

Figure 6.31: Formation of Bose Einstein Condensate.

saw both signs of BEC very clearly, the bimodal distribution and anisotropic expansion. Fig. 6.31 shows the absorption images of the cloud as we cross the phase transition. The pictures are taken after 10 ms expansion time. These are a few things we found important to optimize as we started looking for the signs of BEC:

- The power in the repump beam during imaging should be as small as possible. If the power is too high, the repump can heat up the cloud during picture taking and wash away the signs of a BEC.

- The optical plug might need to be tweaked towards the end (or the magnetic field zero moved using 3 pairs of Helmholtz coils in three directions) since the zero of the magnetic field can shift when the trap is decompressed.

The shape of the BEC on expansion can change considerably depending on the position of the plug beam. We could see the BEC expanding vertically all the way to expanding horizontally, simply by moving the plug beam. We routinely produce BEC's with 2×10^6 atoms with this setup. The largest we have seen was with 5×10^6 atoms. In Georgia Tech, they are able to produce larger BEC's with smaller gradients. We think we are limited to this number by the lack of control over the zero field point after decompression. We have single coils (unlike their Helmholtz pair) to move the trap center. These are not as effective and behaves in a more complicated fashion because of the field gradient in addition to the bias field.

6.9 The YAG tweezer

The BEC is created inside the steel vacuum chamber that has very limited optical access. In order to create the optical potentials required for laser culling we would need to put optics much closer to the atoms. To achieve this, we wanted to transport the BEC over a distance of 25 cm into a glass cell with very good optical access. The method we use is similar to one used by the MIT group [60]. The BEC is first transferred from the magnetic trap to a red detuned optical tweezer. The focus of the tweezer is then moved by

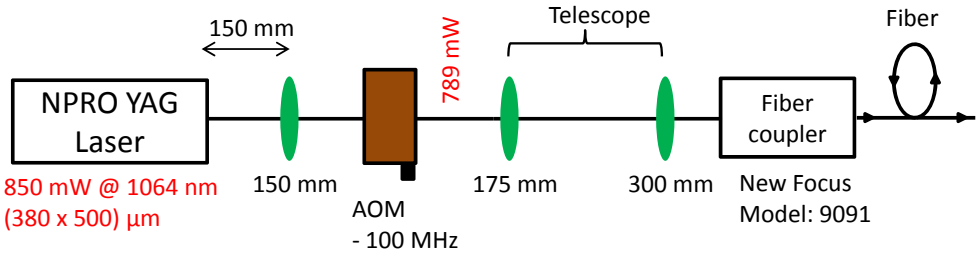

Figure 6.32: Final tweezer setup.

moving the focusing lens which is placed on a translation stage. If the process is done adiabatically, the atoms follow the motion of the moving focus.

The first step was to transfer the atoms to an optical tweezer. Our first attempt was with a 1064 nm multimode fiber laser (IPG Photonics, Model: YLD-1064). The power in the tweezer beam was 3 W after an AOM and was focused down to 28 μm. This should create a well depth of 12 μK with trapping frequencies of 21 Hz and 2.4 KHz in the axial and radial directions respectively. We were able to transfer 100% of the atoms into the tweezer but the measured lifetime was never longer than 2 seconds. We had heard of other groups (including the Rubidium experiment in our lab) having problems with the IPG multimode fiber lasers in that, they too saw very short lifetimes. We were not able to pinpoint the precise problem but we decided to switch to a ultrastable laser (Lightwave Electronics, Model: 126-1063-700) at 1064 nm. Though the maximum power from this laser was only about 800 mW, it immediately gave us a lifetime of 12 seconds in the tweezer with a similar waist and 450 mW of power. We later found out that this lifetime was not limited

by vacuum and had to do with distortion of the plug beam profile (details about this problem will be discussed in the later section on transport). At the time, however, it seemed long enough for us to transport the atoms. Fig. 6.32 shows the setup of the tweezer laser. The beam goes through an AOM which is used to control the power and is coupled into a fiber after a suitable telescope. We used a pinhole spatial filter at first but later switched to a fiber because of its superior spatial filtering performance. The coupling efficiency into the fiber was about 70% Which was limited by the fact that the beam passes through an AOM that distorts the mode and that the output beam from the laser itself is a little elliptic. We used a New Focus (Model: 9091) fiber coupler with a 20x objective lens to couple the beam into a fiber (Newport, Model: F-PM980C-1FCAPC). The lifetime in the tweezer (after solving the beam distortion problem) was more than 40 seconds as shown in Fig. 6.33

The trapping frequency in the tweezer was measured by parametrically exciting the atoms. The radial trapping frequency is 100's of Hertz and can be measured by this process. The idea is to modulate the trap depth by changing the laser power at some frequency and amplitude (much smaller than the total power in the beam). This periodic kicking imparts energy to the atoms which is maximum if the modulation frequency is twice the trap frequency. The energy absorbed by the atoms can be measured in the form of heating of the cloud. Fig. 6.34 shows typical data for the measured size of the cloud after 5 ms expansion (which can be converted to temperature) as a function of the modulation frequency.

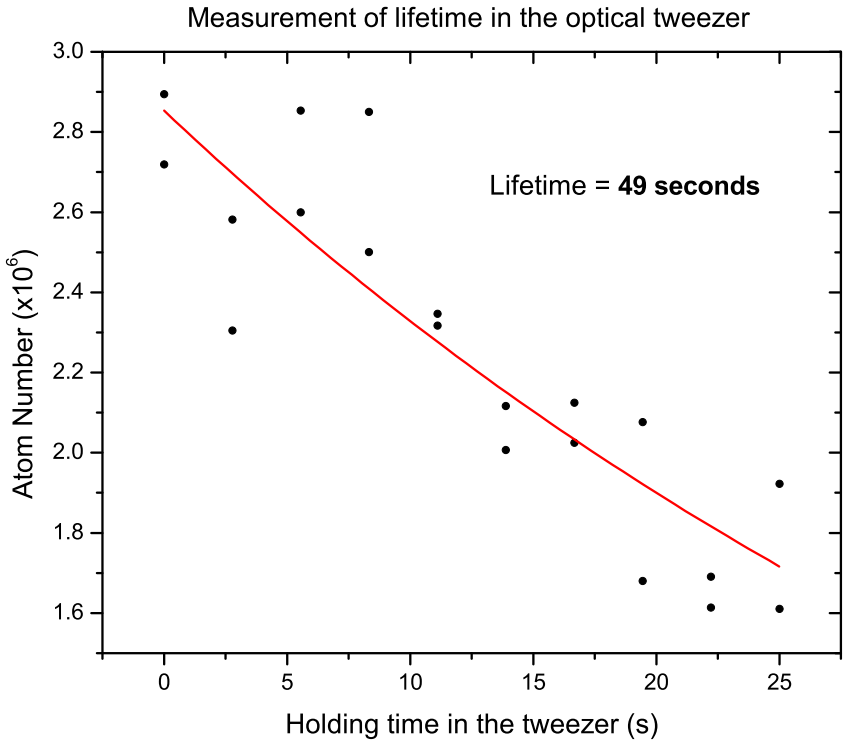

Figure 6.33: Lifetime measurement in the optical tweezer.

We can see two resonances in the plot. The one at $2\omega_{radial}$ being the strongest and another one at ω_{radial}. Knowing the power in the beam and the radial trap frequency, we can calculate the waist of the beam and the axial trapping frequency. The modulation, created electronically by modulating the RF driving the AOM, was on for a few seconds and had an amplitude of 3% of the average power. The circuit to do this is shown in Fig. 6.35.

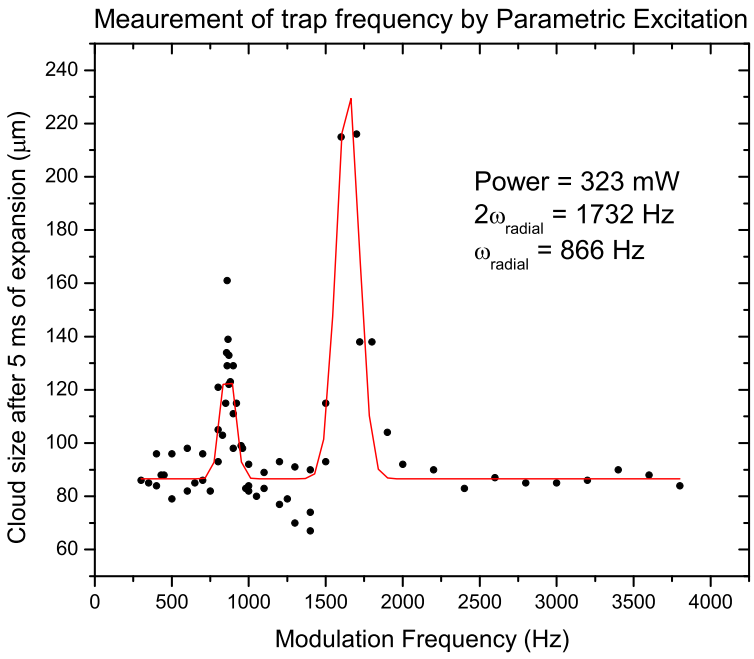

Figure 6.34: Parametric excitation to measure the trap frequency.

6.10 Transporting a BEC

A BEC is an extremely delicate object. Transporting it from one place to another poses a number of challenging problems, most importantly, vibrations. Vibrations during motion can heat up the BEC and destroy it. After their first setup to move the BEC, the MIT group switched over from a ball screw kind of translation stage to an air bearing stage which is known for its ultra low vibration performance and high position accuracy. We had a number of ideas about minimizing vibrations which we tried first and are described in the first two subsection. Eventually, we too had to switch to an air bearing

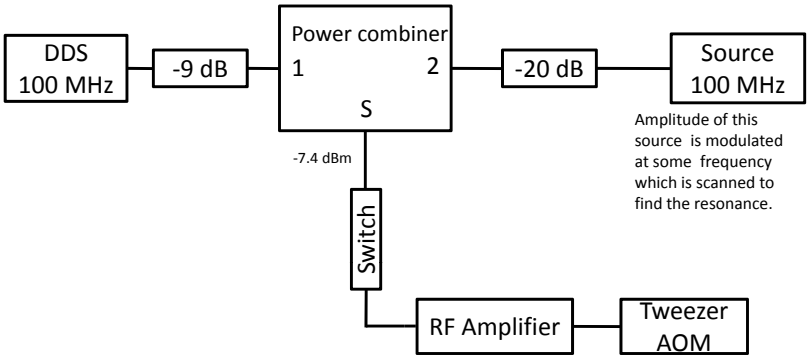

Figure 6.35: Circuit to induce parametric excitation of atoms in the yag tweezer.

stage.

6.10.1 Corner cube (retro reflector)

A corner cube retro reflector is made of three mirrors all mutually perpendicular to each other forming three faces that meet at the corner of a cube. A laser beam incident on any one mirror undergoes multiple reflections (due to the geometry of the mirrors) and returns back parallel to the incident beam, irrespective of the orientation of the corner cube. Due to this unique property, corner cubes can be seen in a number of objects we come across in daily life including bicycle retro reflectors, road signs, field survey instruments and there is even one on the moon that helps us measure the distance between the earth and the moon. A corner cube can also be made of solid glass that uses total internal reflection from the internal glass surfaces to produce the same effect. The ones with mirrors are called hollow retro reflectors and are much lighter than glass ones. Fig. 6.36 shows the working principle of a corner

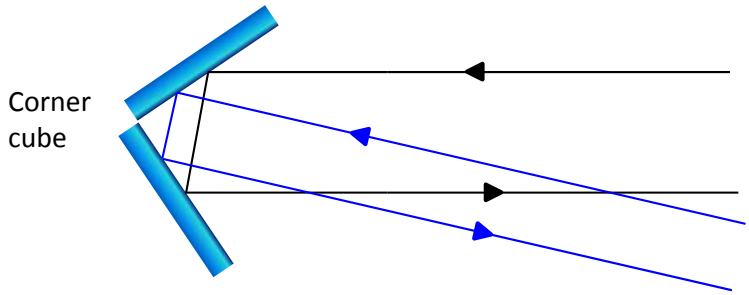

Figure 6.36: Principle of a corner cube retro reflector.

cube.

The transport setup using a corner cube is shown in Fig. 6.37. After the spatial filter, the beam is focused by a 300 mm (2" OD) lens just before the corner cube. The beam is initially polarized such that it goes straight through the polarizing beamsplitter cube. The corner cube reflects back the beam which is retro reflected by a mirror onto itself. The beam travels twice through a $\lambda/4$ waveplate and is then reflected from the polarizing beamsplitter cube. The last 300 mm (2" OD) lens creates the image of the focus at the position of the atoms. In order to translate the focus, the corner cube is mounted on a translation stage. This is not the best setup since the size of the focus would change as we translate it but the change in the spot size was not significant to cause problems. Due to the geometry of the setup, the corner cube has to be moved only 1/4 times the distance through which the focus needs to be moved. The translation stage (Thomson Model: MS33LGBL) is a ball screw type stage driven by a servo motor (Galil Model: BLM-N23-50-

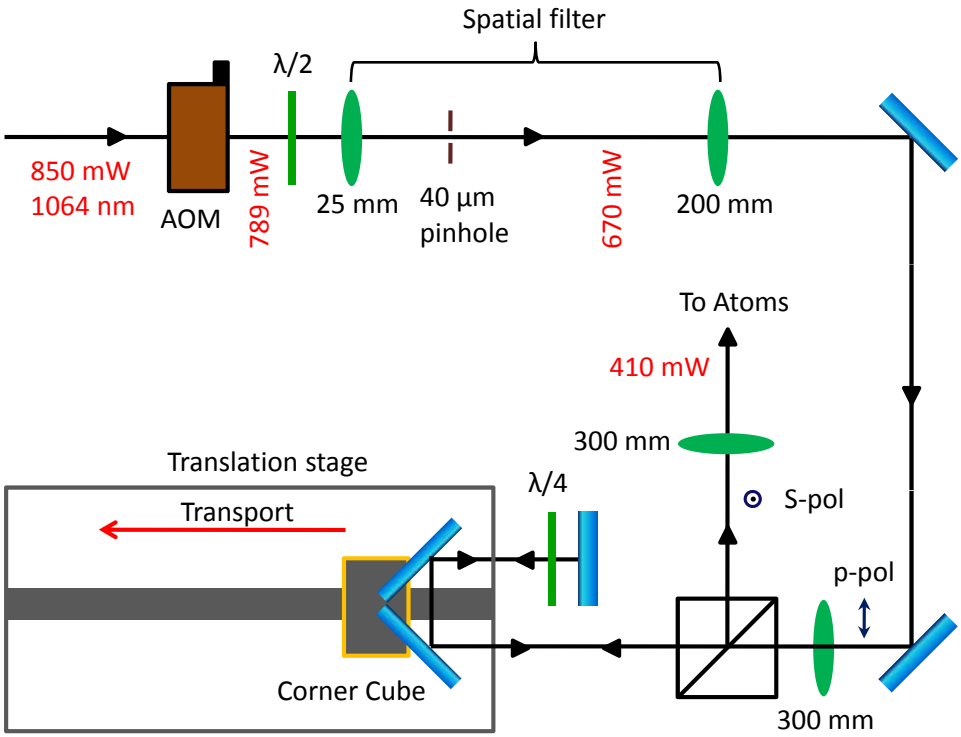

Figure 6.37: Initial setup of the tweezer for transporting a BEC.

1000). The pitch of the screw is 1/4" and the servo motor has a step size of 4000 steps per revolution. Since the final waist of the beam has to be less than 30 μm, the beam size at the corner cube is more than an inch. The corner cube had to be big enough to accommodate such a big beam. Many companies can manufacture big hollow retro reflectors but are very expensive for the accuracy we needed. We decided to make our own corner cube by assembling three 2" OD silver mirrors, two of which are glued to adjustable mirror mounts and the third one is glued directly to the metal mount. In order to use the corner

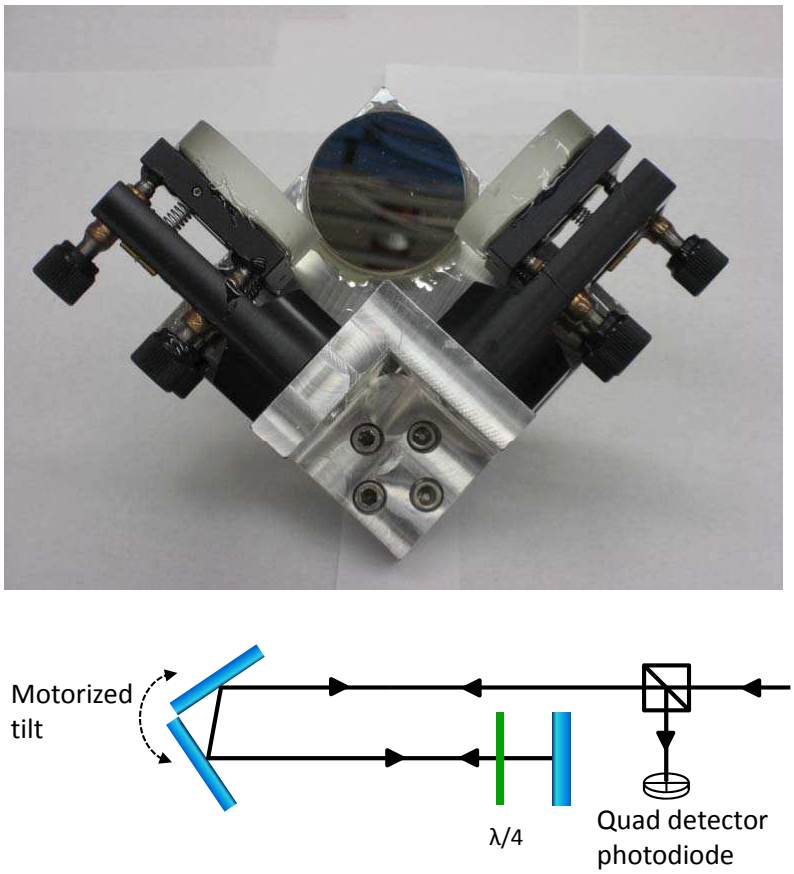

Figure 6.38: Corner cube and the test setup used to align it.

cube to a maximum effect, it is necessary that the angle between the mirrors be very close to 90° (within 1 μrad). We did this by mounting the corner cube on a test setup where we tilted the corner cube in a controlled manner by a large amount (∼10°) and looked for the deflection of the returning beam. We used the mirror mounts to adjust the angle between the mirrors to minimize this deflection. Fig. 6.38 shown the picture of our corner cube along with the setup use for its alignment. We compare the observed deflection angle ϕ,

	Commercial corner cube (Φ/ϕ)	Our corner cube (Φ/ϕ)
Horizontal tilt	5136	11700
Vertical tilt	2627	1027

Table 6.7: Test results of our corner cube compared to a commercial one.

to what it would be if the corner cube was just an ordinary mirror, Φ. Once we found the best position, the screws on the mirror mounts were glued so they never move again. A corner cube assembled crudely by gluing mirrors on three faces of a machined aluminum piece already reduces the deviation of the returning beam by a factor of 20. Table. 6.7 summarizes the best performance of our corner cube and a commercial solid corner cube (which we use one in a wavemeter for wavelength measurement).

We can see that our corner cube was at par with the commercial one, if not better. We expected that the vibration of the slide would be reduced at least by 3 orders of magnitude by this setup. For translations of the corner cube perpendicular to the direction of the beam, the deviation of the returning beam is even smaller. However, when we tried this setup with the atoms the results were not encouraging. We lost all atoms in a few centimeters of travel. We measured the transport efficiency by moving the atoms towards the cell by some distance, wait for 1 second, move them back to the original place and then take a picture to measure the atom number. At first it was difficult to understand why the transport would not work even after such a high suppression of vibrations. Looking at our vibration measurements more carefully, we came to the conclusion that the behavior of the corner cube might be different for high frequency vibrations. We tested the corner cube

by vibrating it at 1 Hz. Because of its heavy mass, it was difficult to measure its response at 100's of Hertz which would be the frequencies of interest since the trap frequency in the tweezer was of that order. We estimated that the reduction in vibrations would still be 50-100 times. It became imperative that we reduce the absolute vibrations of the slide itself. This meant either increasing the load on the slide (the slide was rated to a maximum load of 15 Kg) or come up with some other solution.

6.10.2 Wire coupling vibration isolation

The vibrations of the slide come from two sources. The first being the driving mechanism which is the servo motor. It is easy reduce these vibrations by tuning the PID for the servo loop. The second problem was coupling the motor to the slide which in our case was done with a ball screw mechanism. We believed that we had minimized the first source of vibration as much as possible and were limited mainly by the second source. Our next idea for improving the coupling was inspired by the vibration isolation used in precision measurements experiments, namely, suspending the optical table using steel wires to effectively damp high frequencies. In our case, we intended to use a low vibration crossed roller slide on which the corner cube is mounted and use the ball screw slide to drive it using a wire[2]. The wire sets a cut off frequency above which the transmission falls dramatically. The longer the length of the wire, more would be the suppression of higher frequencies. The elasticity of

[2]We also tried coupling with a ball bearing and with magnets but the results for both cases were worse than the wire.

the wire could have caused problems in the precise positioning of the slide but since the Rayleigh length of the tweezer was more than 2 mm we did not think that would be a problem. Fig. 6.39 shows the test setup we used to measure the vibrations for this setup. During transport, the corner cube is pulled to the right by the spring as the wire relaxes. On its way back, the wire pulls against the spring, thereby maintaining complete control over the motion of the corner cube at all times. The rest length of the spring was 4" and it could be stretched to more than 7". Its spring constant was 5 lb/inch. The vibrations on the corner cube slide were now below the detection limit of our accelerometer. To increase the sensitivity, a 14" long aluminum post was rigidly attached to the slide and the accelerometer was placed on top of it. This helped us measure vibrations at the slide much below the limit of the accelerometer. We tried coupling with different thickness wires and different materials (copper and steel). The steel wire reduced the vibrations in the 100 Hz region by two orders of magnitude. In a final attempt, we got rid of the ball screw slide completely and let the wire wind directly around the shaft of the motor. This worked the best. An ordinary steel or copper wire tends to curl up after winding and unwinding a few times around the shaft. To avoid this we used a nitinol wire that is known to retain its shape even after very sharp bends. We also loaded the crossed roller slide with 45 Kg of lead and mounted the corner cube on sorbothane for additional vibration isolation. The measured acceleration for the final setup was 50 mm/s^2 (0.005g, which is more than one order of magnitude below that measured by the MIT group in their first transport setup with a ball screw slide) at 100 Hz measured 14"

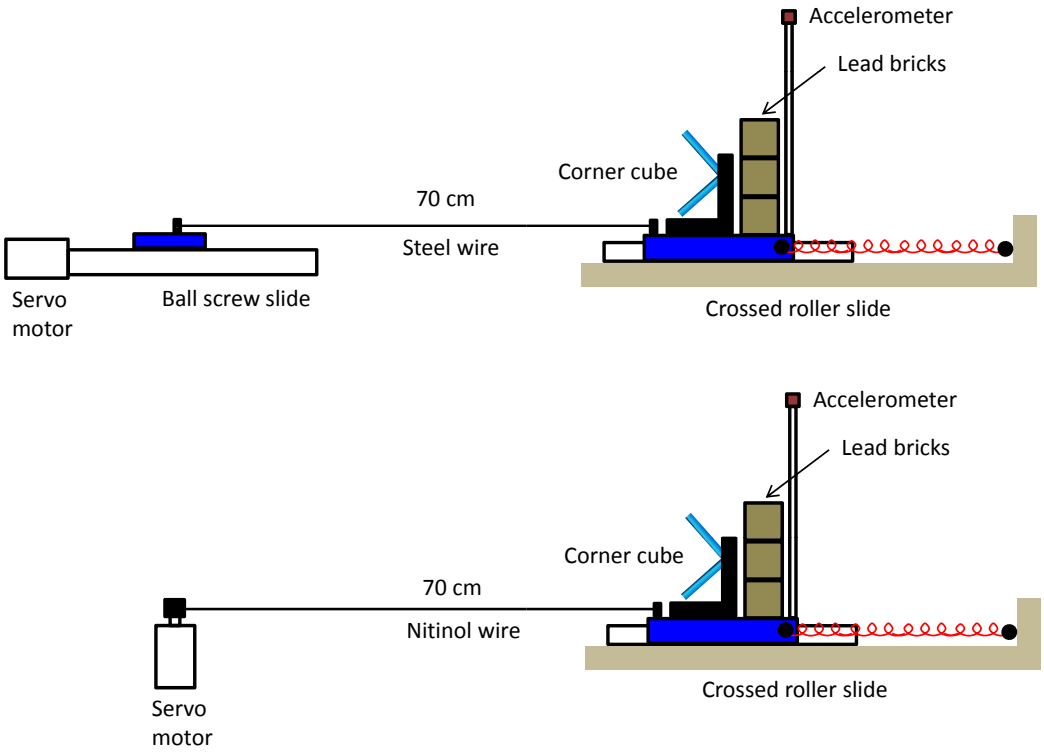

Figure 6.39: Wire coupling setups for vibration isolation (drawing not to scale). The lower setup worked the best.

above the corner cube slide. The estimated vibration amplitude was 50 nm at the slide. The corner cube reduced the final vibrations even more. Table 6.8 shows our estimate of vibration reduction for the complete system. Along the axial direction, the vibrations were reduced by the wire coupling and lead weights but the corner cube made those vibrations worse by a factor of 4. The reproducibility in position was 500 μm. To improve the initial position reproducibility of the slide, we used a position sensing variable resistor.

	Vibration reduction factor
Wire coupling	100
45 Kg weight	10
Corner cube	50-100

Table 6.8: Estimate of vibration reduction due to different methods.

All these improvements resulted in 7% transfer efficiency of the atoms and they were still being heated considerably (the exact amount was difficult to measure because of very low atom number and fast expansion). It was clear at this point that either the problem was something else or the vibrations were doing something we did not understand. We decided to eliminate the vibration problem completely by buying an air bearing stage similar to the one used in MIT since we knew its vibration specs were better than what is needed to transport a BEC.

6.10.3 Final configuration

After many failed attempts with the mechanical bearing stage, we bought an air bearing stage manufactured by Aerotech (Model: ABL20030) with a maximum travel of 300 mm. The slide used dry air at 85 psi for levitation and a linear motor for the drive. Since there are no mechanical contacts involved, there is basically no friction, the precision in positioning is 40 nm and the service life is practically infinite. The transverse vibrations during motion were quoted to be 5 nm. The slide was mounted on a granite block (Standridge granite corp, grade: AA, overall accuracy 0.000037) and held in place by stoppers. The manufacturer recommends tapping holes in granite and securing the slide with screws but we did not do that since were were going to

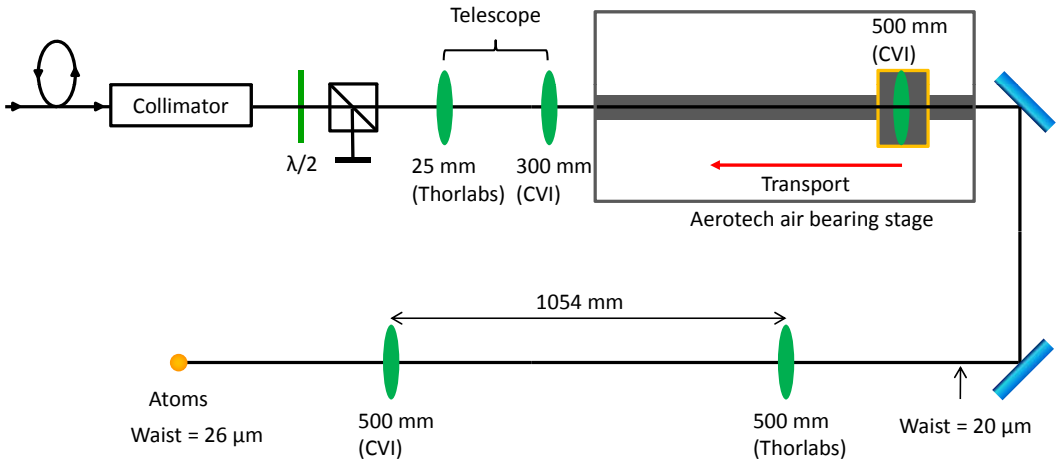

Figure 6.40: Final transport setup.

use it in the horizontal orientation. The dry nitrogen for the slide came from a industrial grade nitrogen tank. With the new slide, we decided to abandon the corner cube idea and go with the simpler setup of translating a lens. The setup is shown in Fig. 6.40. The lens on the translation stage focuses the beam to a waist of 20 μm. Since the air bearing setup is very bulky, we had to set it up far away from the atoms and then relay the focus to the atoms using a 500:500 telescope. This unit magnification telescope reproduces the exact wavefront at its object focal plane on to the atoms by double Fourier transforming it. As the position of the first focus is moved, the focus at the atoms moves by the same amount. In reality, the distance between the lenses was not exactly 1000 mm but it does not have a big effect on the final result; only that the translation between the focii is not 1:1. It is important that the last lens before the atoms be of a very good quality to achieve a small focal spot. Once the new setup was in place, we tried transporting the atoms and got exactly

the same results as before! It was clear that the problem was something else. We looked more closely at the beam profile and suspecting that the mode was bad, we replaced the old pinhole spatial filter to a fiber. The real problem turned out to be our plug beam that was distorting the tweezer beam. The setup of the optics close to the glass cell is shown in Fig. 6.41. There are a number of beams that need to be mixed together. First, the MOT beam at 589 nm, 1" in diameter and carrying 15 mW. Second, the plug beam at 532 nm, 1 mm in diameter and carrying 3.5 W. Lastly, the tweezer beam at 1064 nm, 1.5 cm diameter and carrying 350 mW. The MOT beam was too weak to cause any problems. The plug beam is the most intense. After the evaporation stage, the tweezer beam is turned on to transfer atoms into it and then the plug beam and the magnetic trap are turned off simultaneously. Prior to this, the plug beam is on for 30 seconds during evaporation. During this time, it heats up the last dichroic beam splitter that mixes the tweezer and the plug beams. After the plug beam is turned off, this dichroic begins to cool, distorting the tweezer beam (we believe) in the form of moving fringes across the beam profile. If this modulation is deep and slow, it can scoop the atoms out of the tweezer. To avoid the problem, we physically separated the plug and the tweezer beams on the optics as much as we could. The inset on figure 6.41 shows the tweezer and plug beams as seen on the cell window before and after this change. As an additional precaution, we replaced the last dichroic beam splitter (which was made of BK7) to fused silica one which is knows to have a smaller thermal expansion coefficient. This immediately solved our problem. Firstly, it increased the lifetime of atoms in the tweezer from 12 seconds to

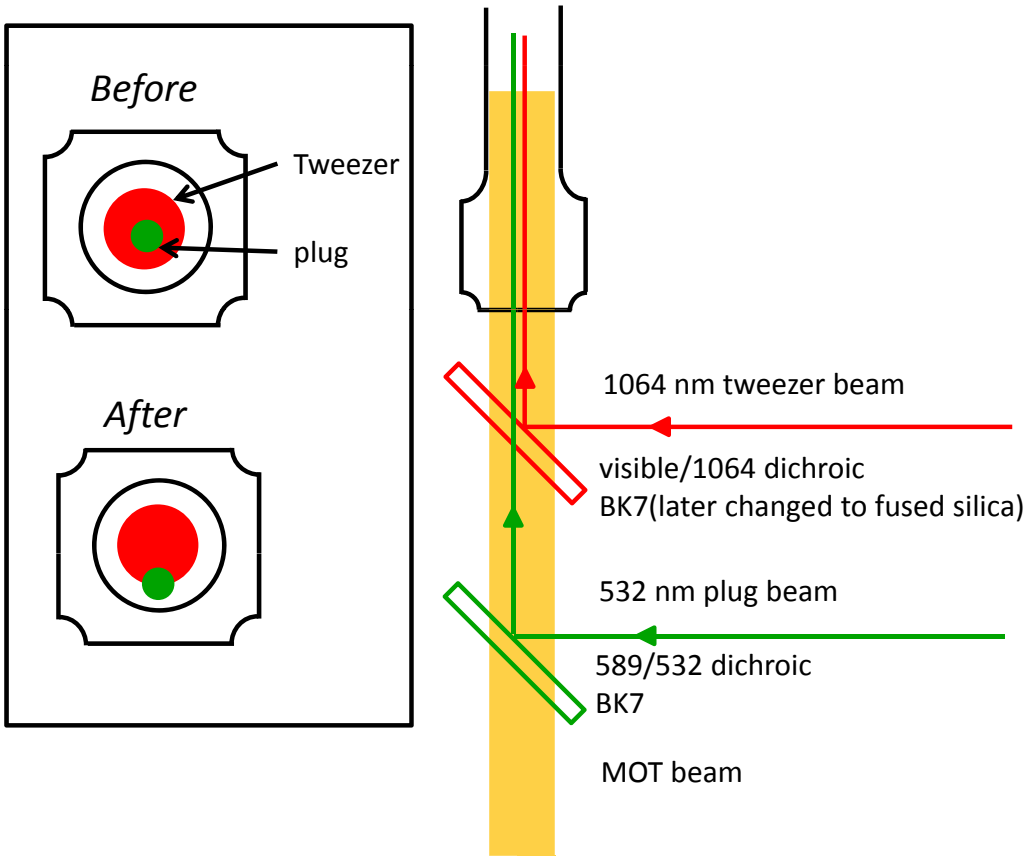

Figure 6.41: Mixing of different beams before entering the chamber.

over 40 seconds. Second, the transport efficiency went from 7% to 50%. The plug now comes at an angle and falls far off axis on a lens which causes the cloud to be split into two in the OPT. This reduced our transfer efficiency from the OPT to the tweezer to only 50%. Fig. 6.42 shows the motion profile of the slide. The transport works over a wide range of acceleration and velocity values and turned out to be relatively insensitive, except, higher the speed better is the transport efficieny. This is completely counter intuitive since a slower

speed would mean better adiabaticity during transport. We believe that even this effect is related to distortion of the beam during transport. There could still be spatial intensity modulation in the beam profile which tends to move, as the focus is moved. If this happens slowly, the atoms are able to follow it and be pushed out of the beam. On the other hand, if the transport is done fast, these modulation move too fast for the atoms to follow them and all they see is an average attractive potential due to the tweezer. This is one way we can explain what we see but we did not investigate this throughly to see if this was indeed true. Fig. 6.43 shows the image of atoms in the glass cell. We are able to transport 50% of atoms through 23 cm in 1 second. After a round trip journey (going to the glass cell, waiting for 1 second and coming back) the atoms get heated by 600 nK. This is large enough to just cross the critical temerature of a BEC so we ended up moving mostly thermal atoms and try to condense them in the cell. We could not directly measure the temperature of atoms in the glass cell using the imaging system we had at the time since the cloud was too spread out.

It took many months, since our first try, to move atoms with enough efficiency to proceed to the next step in the experiment. It was unfortunate that we could not tell whether all our efforts to reduce vibrations were fruitful. Since the eventual problem was not vibrations, we could have possibly been below the vibration threshold to transport a BEC but would not be able to find that out (at least in this setup). However, the whole exercise was a very valuable learning experience. Reducing mechanical vibrations has been a notorious problem in many experiments and hopefully our experience will

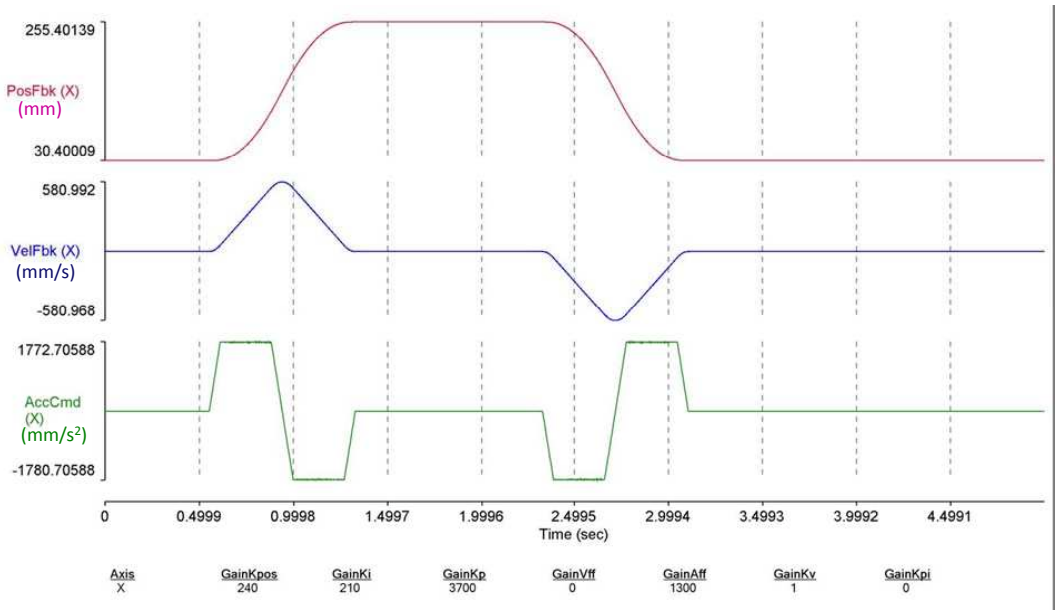

Figure 6.42: Distance, velocity and acceleration profile during transport.

be helpful in solving problems of this nature. It has already helped us when designing a setup to dynamically change the lattice spacing of an optical lattice with high mechanical stability. Details of this setup are discussed in a chapter 7.

6.11 High Frequency Optical Trap

The transverse motion of atoms in a highly elongated, cylindrically symmetric trap can be described by the Hamiltonian:

$$H_\perp = \frac{p_x^2 + p_y^2}{2m} + \frac{m\omega_\perp^2(x^2 + y^2)}{2} \tag{6.8}$$

This trap can be considered one dimensional if the thermal energy and interaction energy of the atoms is much smaller than the transverse energy spacing

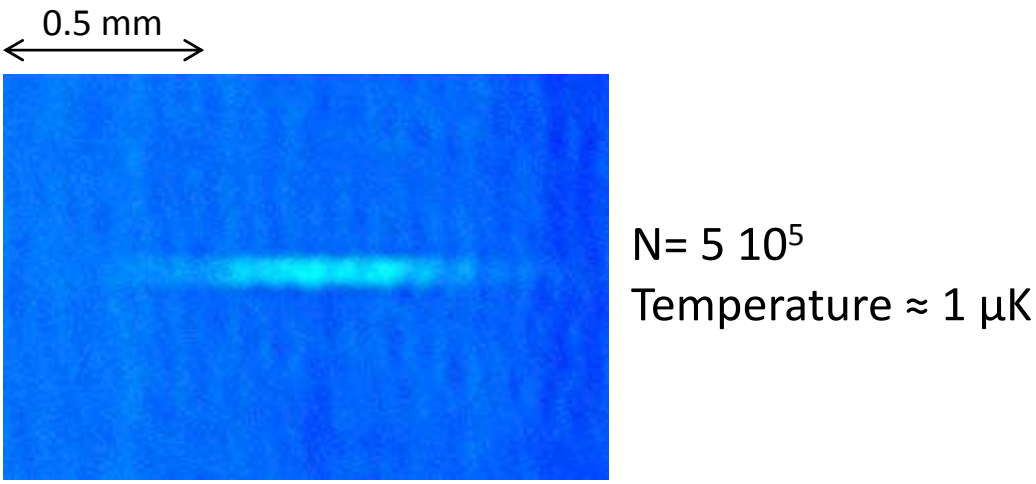

Figure 6.43: Image of atoms in the glass cell after transport.

$\hbar\omega_\perp$. In this regime, the atoms stay in the ground state in the transverse dimensions. The simplest method to get into this regime is to load atoms in a 2D optical lattice with high transverse trapping frequency [61, 62]. One problem with this method is that it creates many 2D traps in parallel. We would like to create only one trap. Our method for the 1D box is based on [63] where they load a BEC in a 1D box created by crossing two TEM_{01} mode laser beams. This creates a 1D tube whose ends are plugged with laser sheets. Their experience helped us in developing the next generation of such a trap where the two beams copropagate with their symmetry axes perpendicular to each other. The TEM_{01} mode is created from the TEM_{00} mode of the laser using a phase plate. We took extreme care in manufacturing the phase plate and is described in the next subsection. This section describes the creation of the 1D optical box.

6.11.1 1D tube

A TEM_{01} mode can be created by a number of techniques including a cavity locked to the TEM_{01} mode, optical fiber mode converters or by splitting a gaussian beam into two and recombining them with a π phase difference. Our method is illustrated in Fig. 6.44. A 532 nm laser beam is incident on a phase plate made out of a glass window. Half of the window is coated with silicon dioxide of the right thickness (620 nm for λ=532 nm) to add an extra phase of π relative to the uncoated half. The beam passes through the center of the phase plate. After the phase plate, the two halves of the beam interfere destructively along the line of intersection as shown in Fig. 6.44. This creates a plane of darkness in the center of the beam and aligned parallel to it. We similarly create another beam whose dark plane is rotated by 90° and overlap the two beams on top of each other on a polarizing beam splitter cube to create a dark tube. Since the laser wavelength is blue detuned with respect to the atomic transition, this creates a 2D trap where the atoms accumulate in the dark central region. After first few attempts it became clear to us that it was important to have the edge of the coating on the phase plate as smooth as possible to create a flat tube with low corrugation. We created a stainless steel mask which could hold a 1" diameter fused silica window (CVI, Part: PW-1025-UV) as shown in Fig. 6.45. The face of the mask covered half of the window and exposed the other half for coating. The edge between the two halves was machined with as smooth as possible. We then polished the edge using lapping sheets with different grain sizes. The sheet is similar to those used in polishing optical fibers. The smallest grain size that we used

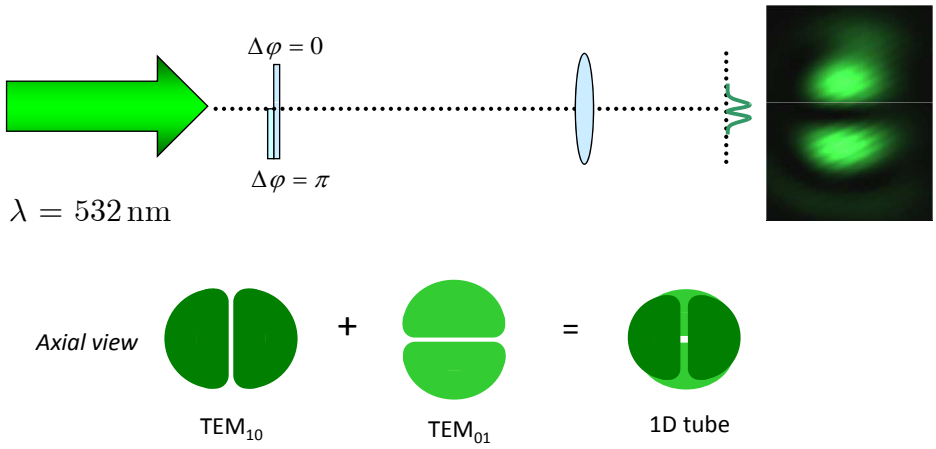

Figure 6.44: Creation of a 1D tube. A Hermite Gaussian TEM_{01} mode is creating using a phase plate. Two such beam oriented perpendicular to each other can be used to create a 1D tube. (Picture rendered by David Medellin)

was 0.05 μm. Fig. 6.46 shows the scanning electron microscope image of a polished mask edge and an ordinary razor blade for comparison. The steel mask was created such that the coating face of the window did not actually touch the steel edge but was separated by about 0.25 mm. We were concerned about the coating peeling off along with the steel mask when separating the window from the mask. The coating was done using ion beam sputtering by Precision Photonics. The coating results were very good and the picture in Fig. 6.44 shows the mode of the laser after the phase plate. To get high trapping frequencies, the beam needs to be focused down to a few microns. Focusing the beam to such a small waist can affect its mode quality so we measured the profile of the focused beam by scanning a 0.5 μm pinhole across it to check if the contrast of mode was retained. Fig. 6.47 shows the measured profile of the mode for a beam focused down to a waist of 3.4 μm. An ideal

Figure 6.45: Picture of the steel mask used to create the phase plate for the TEM_{01} mode.

TEM_{01} mode (oriented with the nodal line along y axis) is described by the equation:

$$I(x,y) = \frac{P}{\pi w_x w_y}\frac{8x^2}{w_x^2}exp(-\frac{2x^2}{w_x^2} - \frac{2y^2}{w_y^2}) \tag{6.9}$$

where, P is the total power in the beam and w_x and w_y are beam waists along the x and y directions respectively. The red curve is a fit to the observed profile assuming $y = 0$ in Eq. 6.47.

The measured contrast of the mode was 96 % and was limited by the size of the pinhole since it averages over 0.5 μm of the beam. It can be seen that the two peaks are unequal in height which is due to the finite transition width between the coated and uncoated half of the phase plate. We can also see some weak fringes along the edges of the beam. In order to minimize these fringes we had to tilt the phase plate by about 45° with respect to the direction of the laser beam. We could change the strength of these fringes and the relative heights of the two main peaks by changing this angle. 1 W

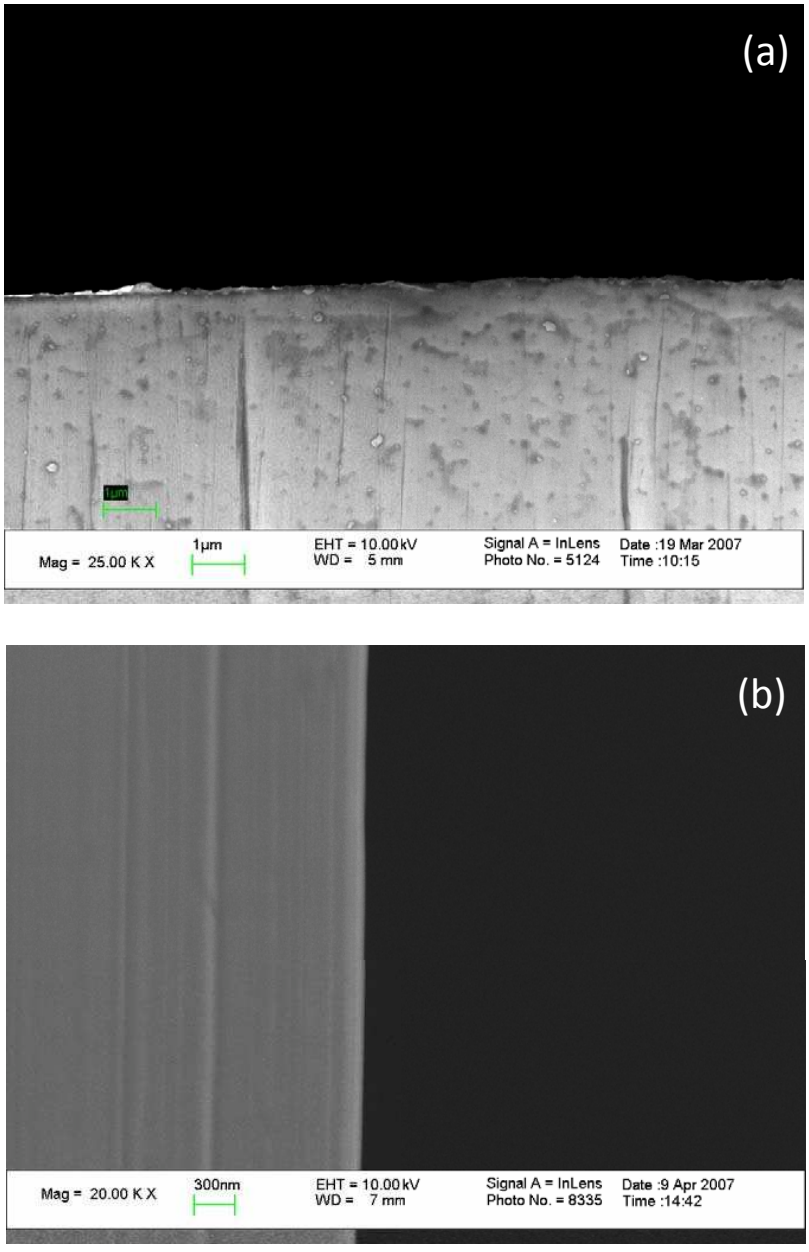

Figure 6.46: Transmission electron microscope images of the edge of a commercial razor blade (a) and the edge of our home made steel mask (b) manufactured by us to create the phase plate for the TEM_{01} mode. The surface irregularity for a razor blade is 200 nm while that for our mask is 15 nm.

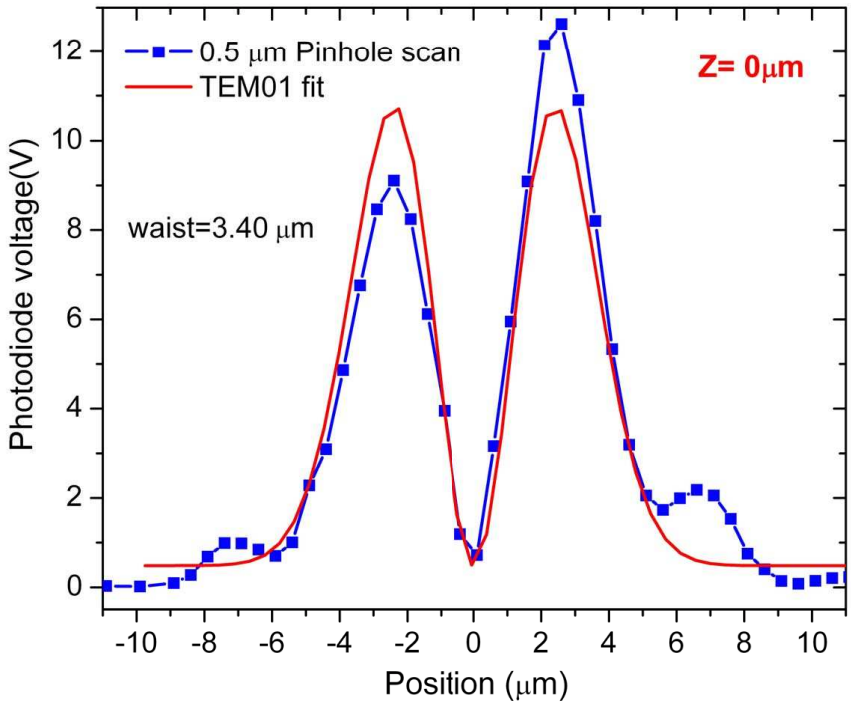

Figure 6.47: Profile of the TEM_{01} beams obtained by scanning a 0.5 μm pinhole.

of power in the beam would give a the well depth of 5 mK and a transverse trapping frequency $\omega_\perp = 2\pi$ 170 KHz for the tube. The optical setup used to create the 1D tube is shown in Fig. 6.48. A 0.66 mm beam (λ=532 nm) is split using a beam splitter. Each beam passes through an 80 MHz AOM that shifts the frequencies of the two beams so that the total difference in their frequencies is 160 MHz. This prevents the two beams from interfering with each on recombination. Each beam goes through a TEM_{01} phase plate. One of the phase plates is aligned horizontally while the other one is aligned vertically.

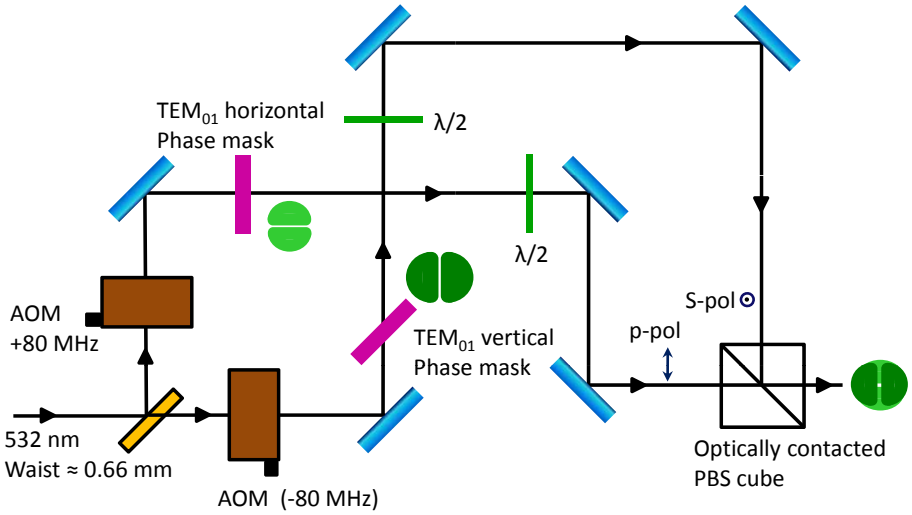

Figure 6.48: Optical setup to produce crossed TEM_{01} beams.

Each beam then passes through a half waveplate that is used to combine the two beams with orthogonal polarizations at a polarizing beam splitter cube (CVI, part: PBSO-532-100). This cube is optically contacted and does not use any cement. This is necessary to avoid distortion of the beam due to thermal effects since we pass 3 W of total power through it. Fig. 6.49 shows the image of the 1D tube and the beam profile before being focused.

The beam with the dark tube profile is focused at the atoms using a 100 mm achromatic lens (Coherent). The size at the atoms can be changed from 15 μm to 5 μm by introducing a telescope before the final focusing lens.

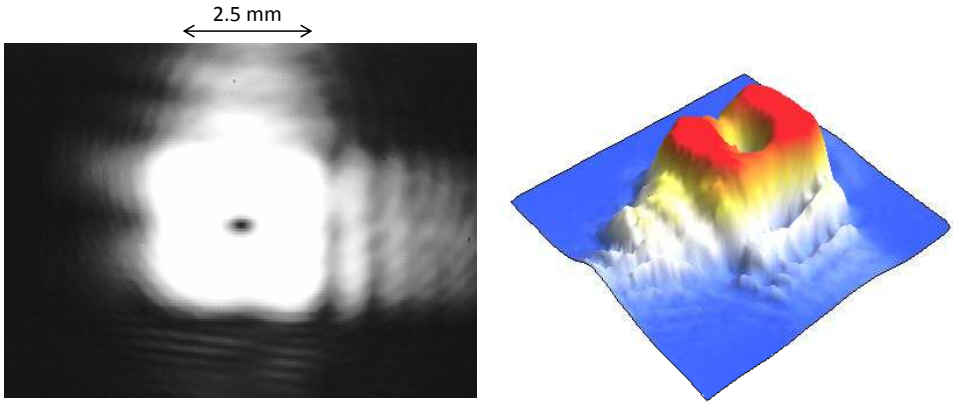

Figure 6.49: Picture of the TEM01 tube.

6.11.2 Endcaps

The 1D tube provides 2D confinement. To complete the box, we need to add endcaps which are created using two 532 nm laser beam sheets derived from a single AOM. The zeroth order of the AOM, that is used to switch the plug beam, is used to create the endcap beams. After the evaporation stage is completed, the plug beam AOM is turned off which eliminates any distortion of the zeroth order beam, which is now be used for the endcaps. Fig. 6.50 shows the setup for the endcap beams. The beam passes through an Acousto Optic Deflector and then through a 25:200 telescope to create a big enough beam to be focused down to a small spot size. To create the elliptical shape of the beam, we insert a 1000 mm focal length cylindrical lens inside the telescope. This makes the telescope imperfect along one of the transverse directions. On focusing this beam, we find that the focii along the x and y directions are located at different positions. This creates two possible locations for light sheets, one oriented along the x and the other along the y

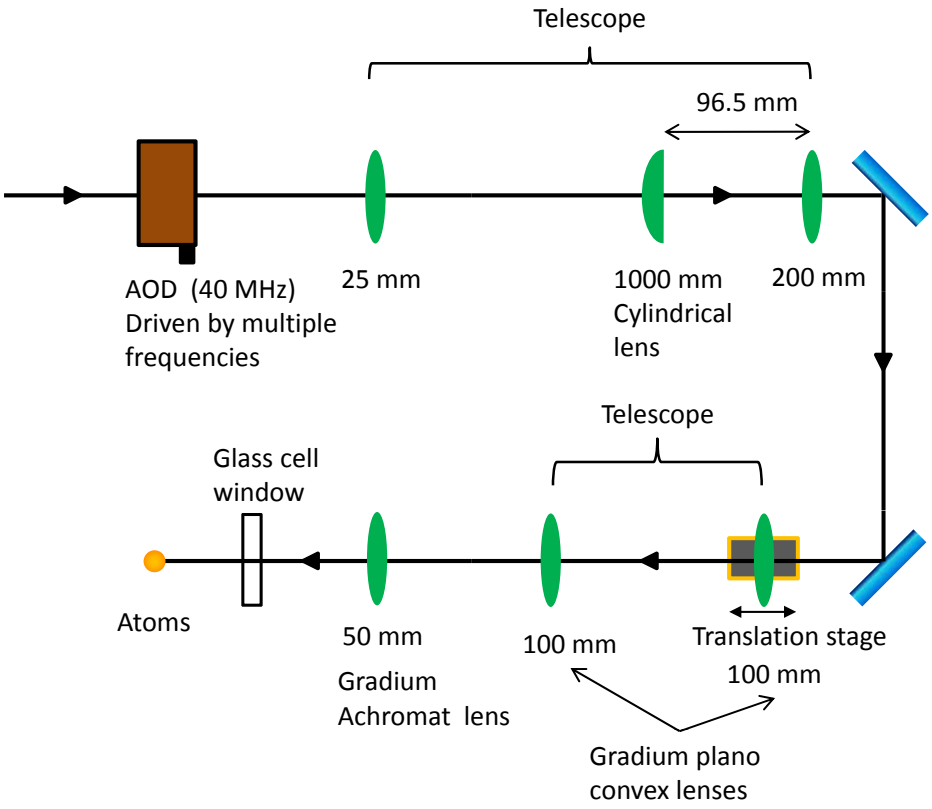

Figure 6.50: Setup of the Endcap beams.

direction. The focal length of the cylindrical lens is chosen by trial and error to create the desired aspect ratio for the sheets. This setup creates a beam that acts like a sheet because the change in the beam size along the major axis is insignificant over the Rayleigh length along the minor axis. This method to create a light sheet by introducing astigmatism is much easier than creating an elliptical beam of the desired aspect ratio and then focusing it down with a spherical lens. The beam then passes through a 100:100 telescope made of 100 mm Gradium plano convex lenses (lightpath technologies, Part: GPX30-

100). The first lens of the telescope is on a translation stage which is used to align the position of the focus of the beam to the atoms. The beam is finally focused at the atoms by a 50 mm focal length Gradium achromatic lens manufactured by Lightpath Technologies (Part: GAD25-50). This lens has a superior performance compared to ordinary achromats when focusing a beam down to a small size. The smallest waist of the endcap achieved with our setup is 3 μm. The light sheet has an aspect ration of 1:15 giving a 45 μm waist along the major axis.

In order to create the two endcaps, the AOD is driven simultaneously by two RF frequencies. Each frequency creates a beam whose angle (and hence its position after focusing at the atoms) can be controlled independently by changing the frequency while the powers in two two beams are coupled due to the fact that the diffraction efficiency of the AOD depends both on the RF frequency and power. For our parameters, two frequencies separated by 10 MHz create two spots separated by 5 μm at the atoms. The bandwidth of the AOD is 40 MHz which limits us to a maximum box size of 20 μm.

6.12 Loading atoms in a 1D Box

The size of the atomic cloud when held in the tweezer is almost 1 mm. As described in the last section, the maximum size of our 1D box can only be 20 μm. Transferring atoms from one trap to another with such large disparity in size would mean we would have to take a very big hit in the atom number (more than factor of 50). To increase the transfer efficiency, we would want

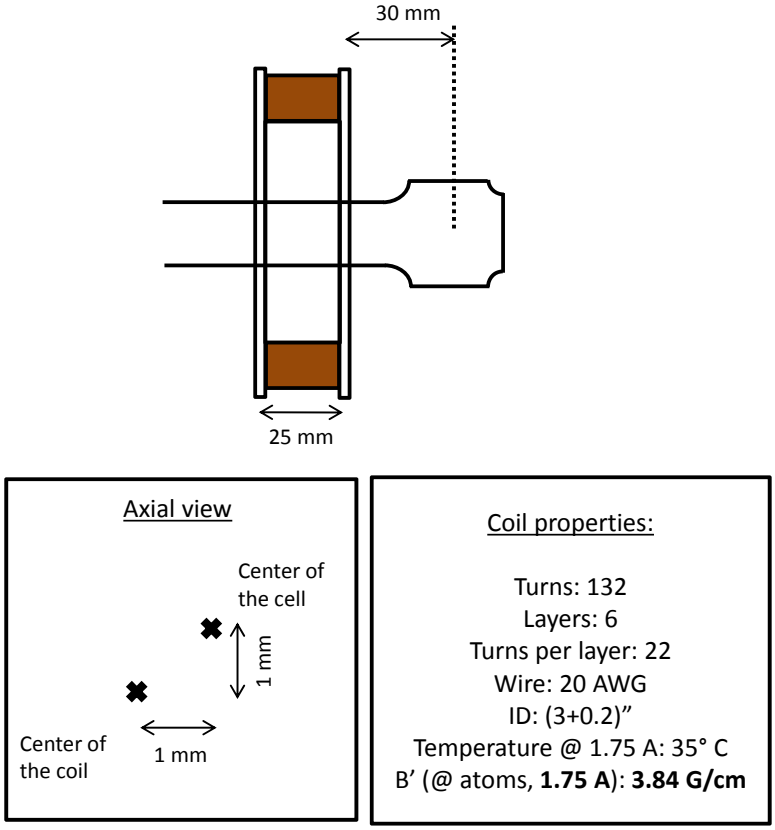

Figure 6.51: Setup of the coil on the glass cell for magnetic compression of the cloud.

to compress the cloud. We were able to do this with the help of one endcap and a magnetic field gradient. Fig. 6.51 shows the location and parameters of the coil used to compress the cloud in the cell. The sequence for loading the atoms from the tweezer into the 1D box would be as follows:

1. Align the first endcap to the tweezer and turn it on even before the transport starts so the atoms are held against that endcap on one side when they reach the cell.

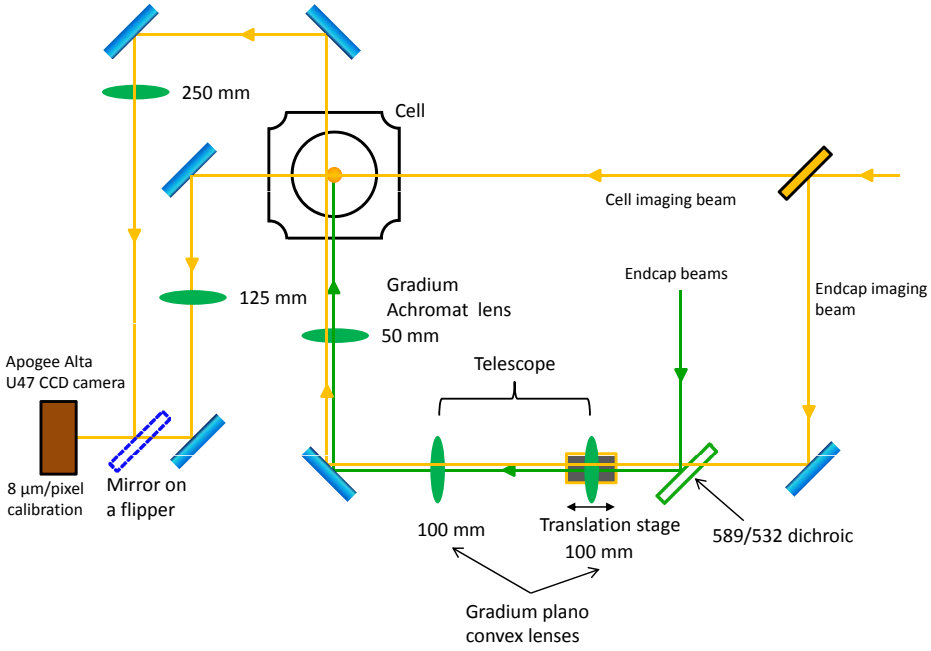

Figure 6.52: Optics setup at the cell for imaging the atoms and aligning the endcaps.

2. Compress the cloud against the endcap using a magnetic field gradient. Evaporate the atoms at this stage to get a BEC.

3. Turn on the second endcap so the atoms are now held by the two endcaps along the axial direction and the tweezer in the transverse direction.

4. Turn on the 1D tube and turn off the tweezer.

We learned many things from our experience in aligning the optical plug beam. An important lesson was to have the imaging system such that we can see the atoms and the beam on the CCD camera simultaneously. Fig. 6.52 shows the optics setup of for endcaps and imaging beams in the glass cell. Usually, the

cell imaging beam is used to detect atoms. The endcap imaging beam was used only for aligning the endcaps. This was a very useful tool that allowed us quick alignment of a beam as small as the endcap beam. During initial alignment, we put maximum power in a single endcap beam and turn it on even before the transport began. We transported the atoms through enough distance so as to be sure that they were definitely moving past the endcap beam. The first signal of the endcap was a reduction in the atom number since the atoms get swept away by the endcap beam as the tweezer moves. The Rayleigh length of a 3 μm beam is only 54 μm. After we saw first signs of the endcap beam, we started reducing the power and moving the focus by translating the 100 mm lens to see if the effect increases or decreases. The best focus position was when we saw the maximum effect on the atoms with minimum power. At this point we could actually see the atoms in the tweezer truncated by the presence of the endcap.

Once the atoms were held against the endcap, we turned on the cell coil to compress the cloud. The field gradient at the atoms for compression was 6 Gauss/cm. This compressed the cloud size to less than 200 μm. This increases the density and collision rate allowing for more efficient evaporation and will also improve the loading into the 1D box. In the next stage the second endcap beam is turned on to create a 20 μm size cloud. The loading sequence is summarized in Fig. 6.53.

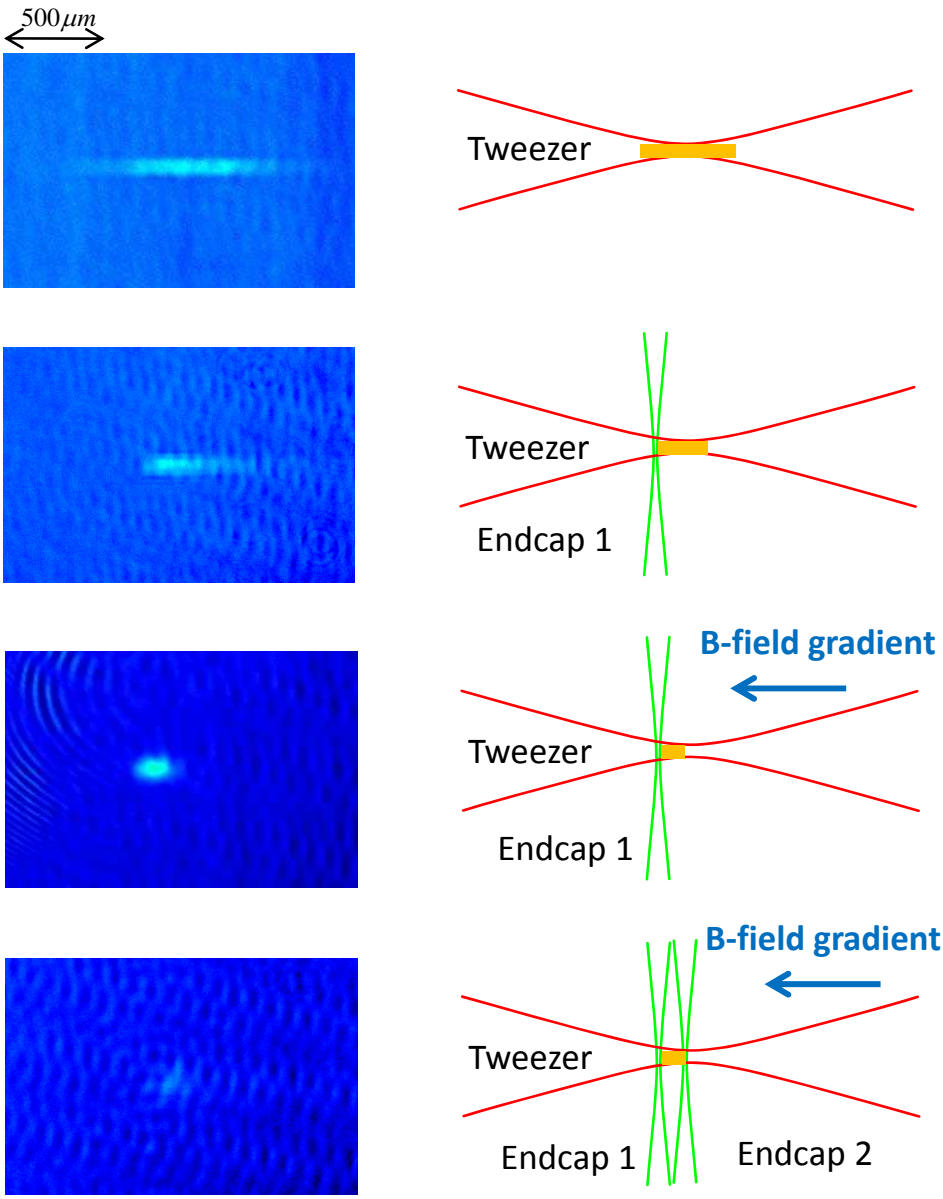

Figure 6.53: Sequence before loading atoms in the 1D box.

6.13 Fluorescence Detection

Counting small atom numbers could be done by fluorescence imaging. This method has a very high signal to noise ratio down to a single atom. Atoms that are exposed to near resonant light will scatter photons from the laser beam into all directions. These photons can be collected using a lens and counted. The rate of the scattered photons depends on the number of atoms that scatter light. For very small numbers this relationship is linear (ie: the number of photons scattered by 4 atoms is twice the number scattered by 2 atoms) and you can count atoms with very high accuracy. The method was first demonstrated in a MOT [64] and is now a widely used method to detect single atoms. A common method to count small numbers is by capturing it into a MOT and measuring the rate of fluorescence. However, it can also be done using 3D molasses in addition to a dipole potential strong enough to confine atoms at molasses temperature. We employ a lin $\perp$ lin molasses setup along two dimensions and a circ^+ - circ^- setup along the third direction (due to a large number of optics already occupying the third direction, the circ^+ - circ^- setup was easier to implement). After laser culling, the dipole potential in all directions of the box would be raised to a maximum during the detection stage. We estimate the minimum well depth in all direction to be 700 μK which would be enough to confine atoms at molasses temperature (under 100 μK).

The beam for creating the cell molasses beams is picked off from the imaging beam setup and coupled into a fiber. At the output of the fiber, the

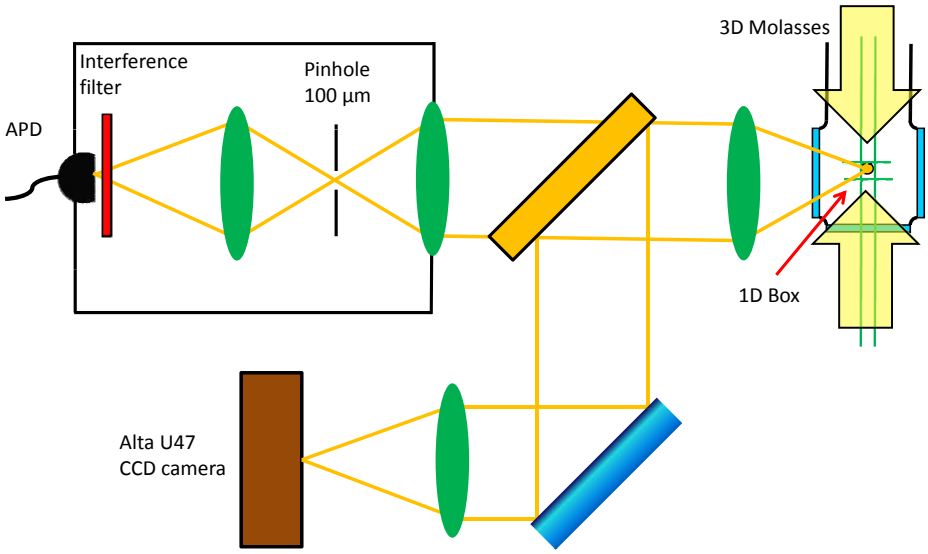

Figure 6.54: APD setup for fluorescence detection.

beam is split into three beams for the molasses. The repump is mixed into the fiber at orthogonal polarization to the cooling beam. The molasses beams perpendicular to the 1D tube are brought close to the cell by two additional fibers. Both beams are retro reflected and pass twice through a quarterwave plate that rotates their polarization by 90°. The beam along the 1D tube is circularly polarized and is retro reflected as well. The frequency of the molasses beams is detuned 3 MHz below the $|F = 2\rangle \rightarrow |F' = 3\rangle$ transition and can be changed using an AOM (this would also change the coupling efficiency into the fiber which would have to be tweaked). The beam waist is 700 μm at the atoms. For a total power of 100 μW in the cooling and repump beams, the peak intensity is twice the saturation intensity resulting in a scattering rate about 3 MHz. Fig. 6.54 shows the detector setup. The fluorescence signal from

the atoms is collected using a biconvex lens (Lightpath Technologies, part: GBX30-40) with F/# = 1.5. The solid angle is of the setup is 0.33 Steradians (2.6% collection efficiency) which corresponds to 80,000 photons per second per atom for the above parameters. The collected photons are focused by a 100 mm lens and pass through a 100 μm pinhole placed at the focus of the lens. This eliminates most of the stray light giving minimal background counts. The light passes through two interference filters (CVI, Part: F10-589.6) before falling on the avalanche photodiode (APD) (Perkin and Elmer, Model: SPCM-AQR-14). The APD is a single photon counting module with a photon counting efficiency of 65% at 589 nm. The TTL pulses from the APD are counted using a high speed counter (National Instruments, Model: PCI-6733) which is interfaced with the control computer.

6.14 Conclusions

All the critical aspects for the experiment were in place when our oven chamber gave serious problems and we could not align the atomic beam to get a big enough MOT. In addition, our dye laser was misbehaving and was given the much needed servicing. We are currently in the process of modifying our oven design and implementing one that is similar to the MIT and Georgia Tech groups. After the system is up and running again there are a few more steps to be completed before we can try to observe Fock states:

1. Evaporating atoms in the cell to confirm that we have a BEC.

2. Transferring from the hybrid tweezer-endcap trap to the 1D tube-endcap

trap.

3. Testing (and calibrating) the single atom detection setup with atoms.

6.15 Outlook

The method of laser culling is a very promising technique to create atomic Fock states. An important consideration in future experiments is whether to choose fermions or bosons for the experiment. The efforts described in this chapter were to get bosons to interact strongly with each other. Bosons interact strongest in 1D and hence we have to go to 1D in a regime where they undergo fermionization. It should be obvious from this that a lot of trouble would be saved if once directly started with fermions. It seems that laser culling with fermions might indeed be simpler than bosons due to Pauli's exclusion principle. If fermions are loaded into a trap and cooled to the ground state, they naturally occupy only two atom per energy state (due to spin degree of freedom) in an optical potential. If the trap is harmonic, then the energy spacing between N fermions in a trap and N-1 Fermions in a trap is given by the trapping frequency and is independent of N. If we make the trapping frequency high enough, we should be able to see phenomenon like number squeezing and Fock states without necessarily having to go to low dimensions (which is difficult). A scheme to produce fermionic qubits with high fidelity using laser culling has been proposed recently [65] which is a promising candidate for quantum computation. This method provides a different and promising direction towards quantum information processing and

quantum computation.

Chapter 7

Optical Accordion

Atom number statistics is an interesting problem in many systems. One such system is the Mott insulator. The Mott insulator was created in cold atom systems by loading a BEC in a 3D optical lattice. For low lattice depths, the BEC is free to move around like a superfluid. Beyond a certain well depth, the coherence between adjacent sites is lost and the system makes a phase transition from a superfluid (easy transport) to a Mott insulator (lack of transport). The experiments so far have created a 3D Mott insulator. In order to create a 1D Mott insulator, we need to isolate one lattice site from a 2D optical lattice (like our 1D box) and then add a lattice along the axial direction. If we create Fock states in a box, we could adiabatically increase the size of the box so it can accommodate enough sites of an optical lattice along its axis and thus create a 1D Mott insulator. Such a system would allow us to study interesting transport in a Mott insulator of N atoms in M sites. In order to make a measurement, we would like to directly count the number of atoms in each lattice site after some evolution time to see how the atoms distribute themselves among the sites. This would require us to have spatially resolved single atom detection capability. This can be done [66], but only for lattice spacings of a few microns which are directly resolvable by far field

optics. To study tunneling dynamics, however, we would need smaller lattice spacings which would mean being able to resolve submicron spacings. This chapter describes a scheme that would allow us to achieve this [3].

7.1 Principle

An optical lattice can be created using two counter propagating laser beams creating a stationary sinusoidal interference pattern. The lattice spacing in this case is $\lambda_L/2$ where λ_L is the laser wavelength. An optical lattice can also be created by interfering two laser beams at an angle. The lattice spacing in that case is given by $d = \lambda_L/(2\sin(\theta/2))$. In order to change the lattice spacing, we can change the angle θ between the beams. One can come up with a number of ways to do it, for example, having an arrangement of mirrors that could be moved on an arc so as to change the relative angle between the reflected beams. One disadvantage of this kind of approach is the sensitivity to mechanical vibrations. From our experience with moving cold atoms, we learned that for a robust system it is important to eliminate vibrations altogether or have a setup that minimizes the effects of vibration. It is especially important in this case since the interference pattern is sensitive to relative phase changes between the beams. The basic idea of our method is shown in Fig. 7.1. Instead of two beams coming at an angle, we have two parallel beams focused by a lens. The two beams intersect at the focus with some angle θ between them. This angle depends on the distance between the two beams (D) and the focal length of the lens (f). Since the beams focus in the interference region, the waist of the incoming beams decides the spatial

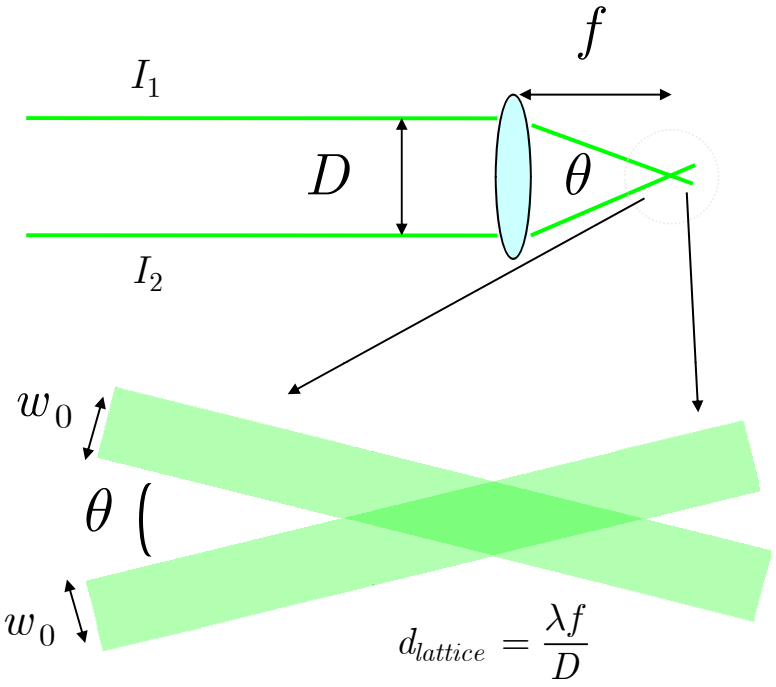

Figure 7.1: Principle of the optical accordion.

extent of the optical lattice. The lattice spacing can be calculated using two approaches. The geometrical optics approach gives, for a thin lens, the angle between the beams to be $\theta \approx 2\ \tan^{-1}(D/2f)$ when θ is small. This gives the lattice spacing to be:

$$d_{lattice} \approx \lambda \frac{(D^2/4 + f^2)^{1/2}}{D} \tag{7.1}$$

As θ increases, this equation becomes inaccurate. Another way to calculate the spacing is to use Fourier analysis which is much more accurate and takes

into account the complete transformation that a lens does on an object. The lattice spacing using Fourier analysis is given by [3]:

$$d_{lattice} = \frac{\lambda f}{D} \tag{7.2}$$

This equation for lattice spacing is valid even for large beams or diverging beams. In order to change the lattice spacing, we could change D whose maximum value is determined by the diameter of the lens. In addition, the value of the focal length f gives the range over which the lattice spacing can be changed. The first step was to confirm that the interference pattern was of good quality. We tested this by focusing two beams with an achromatic lens and observing the resulting interference pattern. The contrast of the pattern was almost 100% and possible aberrations of the wavefront, due to beams falling so far off axis on the lens, did not seem to cause a problem. The next challenge was to devise a setup to change the spacing between the beams in a way that is fairly insensitive to mechanical vibrations.

7.2 Setup and Results

The optics setup is shown in Fig. 7.2. It uses a laser beam derived from the verdi laser at 532 nm. the beam diameter is about 1 mm. The beam passes through a half wave plate and is reflected by a mirror placed on a translation stage. The waveplate is set so that half of the beam is reflected from the first polarization beam splitter cube (1" square). The transmitted beam is p-polarized that goes undeviated through the second cube and is reflected back onto itself with a mirror. The beam passes twice through a quarter wave

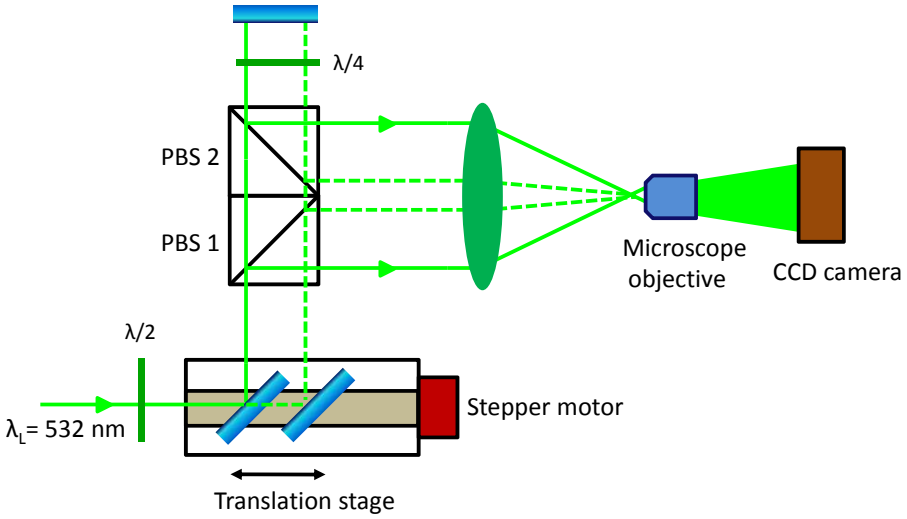

Figure 7.2: Setup of the optical accordion.

plate that rotates its polarization by 90° causing it to be reflected by the second cube on its way back. The two beams are then focused by a lens to create an interference pattern at the focal plane. The pattern is imaged on a CCD camera after being magnified by a microscope objective. To change the distance between the beams, the mirror on the translation stage is moved as shown by the dotted lines. The translation stage is a Velmex ball screw stage with a 2 mm pitch screw. The stage is driven by a Velmex stepper motor with 400 steps per turn.

The lattice will vibrate if there is a changing phase difference between the two beams and is thus similar in stability to a Michaelson interferometer of similar size ($\sim$ 10 cm). The stepper motor has inherent vibrations, but the setup is less sensitive to those since they are along the direction of translation

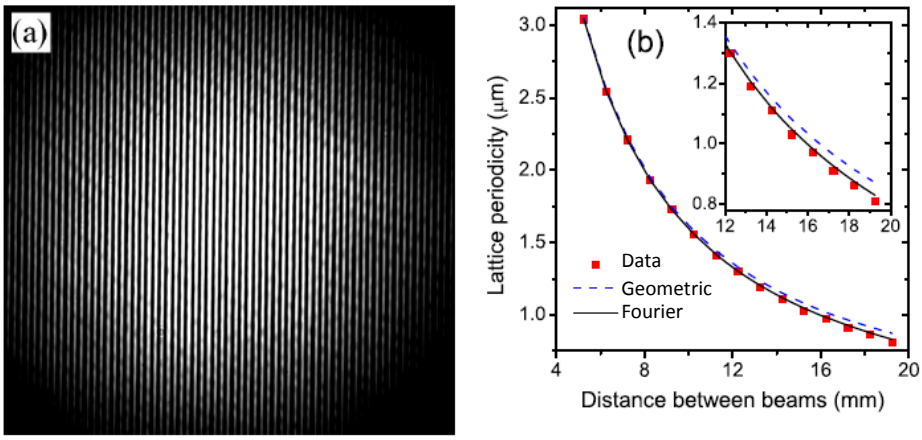

Figure 7.3: Variation of lattice spacing.

which causes a jittering in the lattice spacing (breathing) rather than vibration. In order to prevent a drift of the center fringe after motion, the setup is aligned so that the retro reflected beam is precisely overlapping the incoming beam. The quarter wave plate can be rotated slightly to let some light leak through the two cubes for this alignment. Fig. 7.3 (a) after a 30 mm lens. The waists of the two beams at the focus are 36 μm and 40 μm which were measured using a scanning knife edge. The imaging system was calibrated using this measurement to be 0.0853$\pm$0.0053 μm/pixel. The periodicity of the lattice is 0.81 μm. shows the observed interference pattern and the variation of lattice spacing with the distance between the beams (b). It can be seen that the data fits very well with the black curve, which is the prediction using Fourier analysis, over the complete measurement range. The dotted blue curve is the geometrical optics prediction which is inaccurate for large angles (inset). Fig. 7.4 shows the lattice with different spacings. The focal length of the lens used

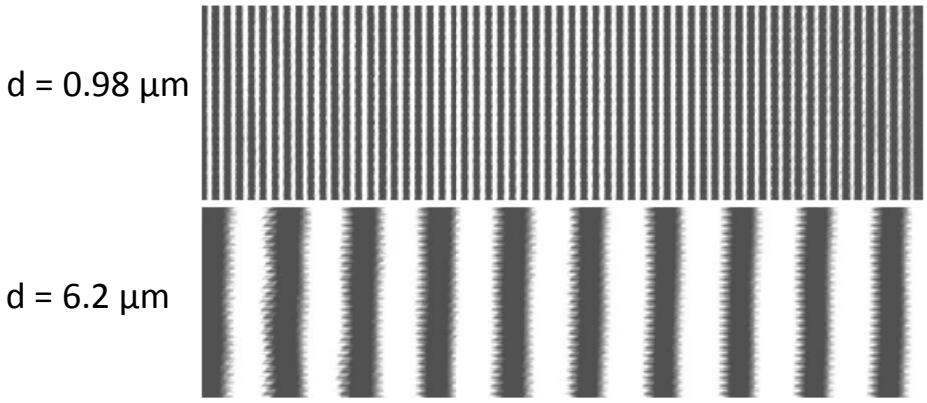

Figure 7.4: DifferentLattSpacing.

is 80 mm. The rough edges of the fringes are artifacts from the camera.

The dynamical performance of the setup was studied by moving the translation stage and recording the fringes with the camera in video mode (30 frames/sec). The image strips at different times during the motion were put together in a single image as shown in Fig. 7.5. The focal length of the lens is 80 mm. The translation stage was moved by 20 mm to change D from 43.8 mm to 3.8 mm. The lattice spacing changes from 0.96 μm to 11.2 μm. The lattice was first expanded, held there for some time and then contracted again. The red line tracks the position of the center fringe during the process. The center fringe moves less than 2.7 μm during the whole process. This measurement, however, is unable to resolve the 'breathing' of the lattice due to vibrations from the slide, as noted earlier. In Fig. 7.5(b) the lattice was changed over the same range but in 1 second, wait for 0.5 seconds and change the spacing back to the original. The speed of the process is limited only by the stepper motor

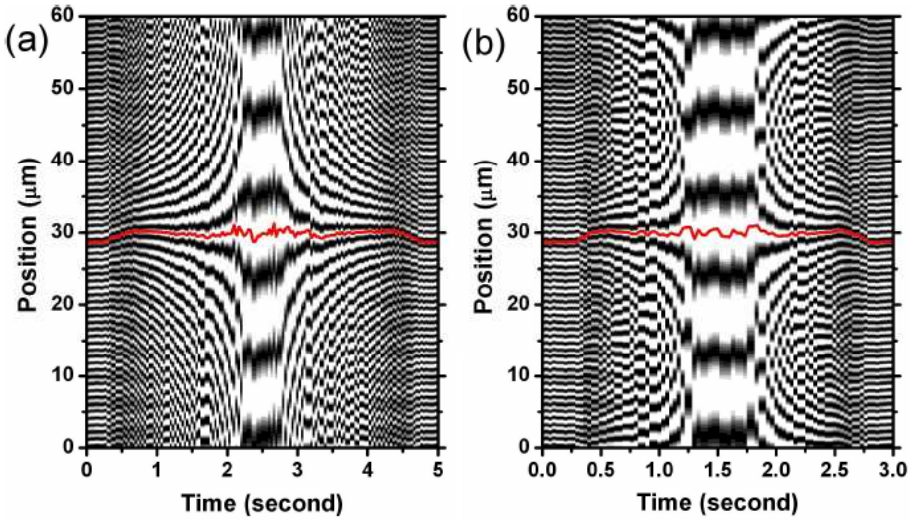

Figure 7.5: DynamicTuning.

and a faster and smoother translation stage would allow much faster change.

7.3 Applications

We envision using this setup by loading atoms in a 1D box and turning on the lattice with a small spacing to allow tunneling. After some evolution time, the atom number at each site will be measured. To do this, the power in the lattice beams will be raised suddenly and the lattice expanded as fast as possible to prevent tunneling between the sites. This will ensure that the atoms do not have time to redistribute among the sites during this process. This process is non adiabatic, the atoms in each site would change their quantum state. However, since we are interested only in the number measurement, this would not cause any problems. Once the sites are spread out far enough to

be resolved, one could do fluorescence imaging using a 3D molasses (assuming the well depth in all directions is large enough to confine atoms at molasses temperature). The setup could be useful even in other experiments that require real time control over lattice spacing. A similar method has been used to successfully rotate a 2D optical lattice giving full control over its spacing and orientation [67].

Appendices

Appendix A

Alignment of laser beams

Aligning beams of small size is always a challenge. The problem is worse if the effect of the beam on the atoms is supposed to be small. We used a number of methods to carry out such an alignment, depending on the situation.

A.1 Using a resonant beam

If one wants to align a beam that is a few hundred microns but its effect on the atoms is very small (either because the beam cannot have more power or because the temperature of the atoms is too high), then this method is very useful. A resonant beam is introduced in the path of the main beam using a polarizing beam splitter cube. The resonant beam is aligned to copropagate with the main beam by picking off the beams before they enter the chamber and making sure the two spots overlap at the focus. Once this alignment is done, the main beam is turned off and the resonant beam is used in its place in the experimental sequence. The mirrors after the cube are used to align the resonant beam. Since the beam is close to resonance, it has a huge effect on the atoms even if they are as hot as MOT temperature. If the beam is aligned, it kicks out all the atoms from the trap. As the beam is misaligned, more and

more atoms are retained in the trap. Once the resonant beam is aligned, it is turned off and the main beam turned on to see the effect. The polarization beam splitter cube is on a easily removable mount for quick switching between the beams.

The accuracy of this method depends on the overlap between the main beam and the resonant beam. Since the beamsplitter cube has to be removed before introducing the main beam, it can deflect the beam which can be as high as 100 μm. This method is good for alignment but not to ensure that the focus of the beam is at the same position as the atoms. That has to be done manually by moving the last focusing lens and running the experiment to see if the signal improves. This method was used to align the billiard beams (10 μm $\times$ 160 μm) for the kicked rotor experiment and the plug beam (40 μm).

A.2 Pulsed beam

This method was inspired by our kicked rotor experiment. It is easy to implement if the beam passes through an AOM before reaching the atoms. The beam by itself is very weak to have any effect on the atoms. The effect can be amplified by periodically switching the beam on and off with the AOM while the atoms are held in the trap. The system behaves like a kicked rotor where the atoms begin to heat up if the beam is aligned. This heating can be measured by time of flight expansion of the atoms. The kick strength is kept to a maximum by having full power in the beam. The signal can be amplified by kicking for a longer time or increasing the frequency of kicks. Fig. A.1

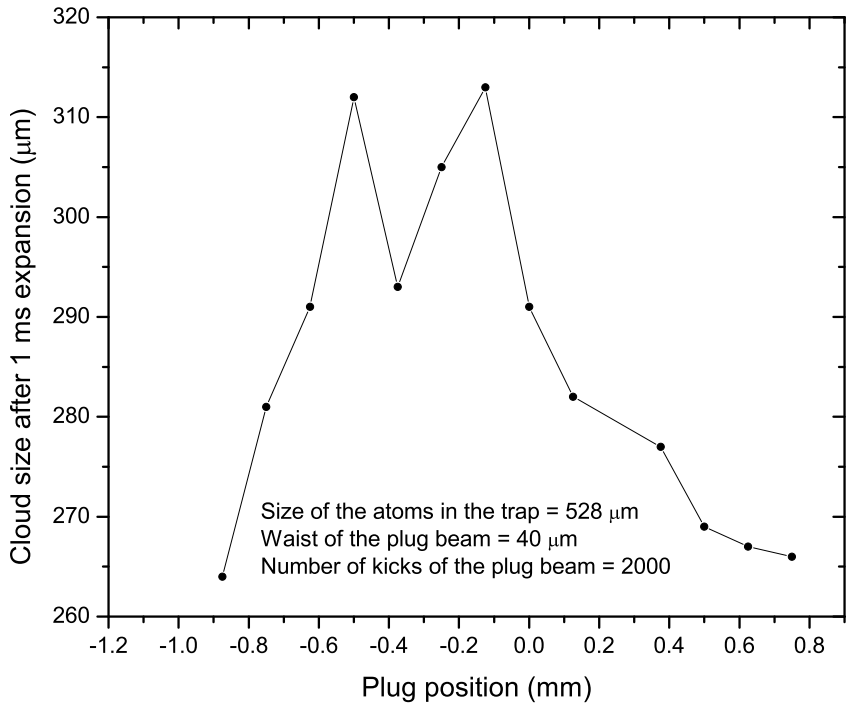

Figure A.1: Aligning a beam by pulsing it (see text).

shows the measured size of the cloud after 1 ms of expansion time as the beam is moved around. The beat alignment is where is heating is maximum.

The accuracy of this method is within the waist of the beam itself. This method can be used to align even the focus of the beam but not very accurately. It was used to align the plug beam (40 μm) in the initial configuration.

A.3 Imaging on the camera

This is the fastest and most reliable of all methods for doing the alignment from scratch. Here the imaging is done along a direction such that the beam to be aligned can be imaged on the camera along with the atoms. The image of the atoms and the beam are overlapped on the camera. The focus of the beam can be aligned by looking at the size of the beam on the camera. The beam should be smallest when its focus is at the atoms.

The accuracy of this alignment depends on the imaging optics. If the beam is passing through the center of all the imaging optics, the accuracy is very good (tens of μm). The worst we have seen is > 100 μm when the plug beam was off axis on the imaging optics. The focus alignment depends on whether the atoms are in focus on the camera. We found that the focus had to be tweaked by a few millimeters from the initial position. The optics for imaging is typically coated for near resonant light. If the beam is further away from the AR coating bandwidth of the optics, it can affect the beam quality and the focusing.

This method was used to align the final plug beam (40 μm) and the billiard beams (3 μm $\times$ 45 μm)

Bibliography

[1] K.C. Henderson, H. Kelkar, B. Gutiérrez-Medina, T.C. Li, and M.G. Raizen, "Experimental study of the role of atomic interactions on quantum transport," *Phys. Rev. Lett.* **96**, 150401 (2006).

[2] K.C. Henderson, H. Kelkar, T.C. Li, B. Gutiérrez-Medina, and M.G. Raizen, "A bose-einstein condensate driven by a kicked rotor in a finite box," *Europhys. Lett.* **75**, 392 (2006).

[3] T.C. Li, H. Kelkar, D. Medellin, and M.G. Raizen, "Real-time control of the periodicity of a standing wave: an optical accordion," *Optics Express* **16**, 5465 (2008).

[4] Harold J. Metcalf and Peter van der Straten, *Laser Cooling and Trapping* (Springer, New York, 1999).

[5] K. L. Corwin, S. J. M. Kuppens, D. Cho, and C. E. Wieman, "Spin-polarized atoms in a circularly polarized optical dipole trap," *Phys. Rev. Lett.* **83**, 1311 (1999).

[6] W. H. Wing, "On neutral particle trapping in quasistatic electromagnetic fields," *Prog. Quant. Elect.* **8**, 181 (1984).

[7] Anderson M. H., Ensher J. R., Matthews M. R., Wieman C. E., and Cornell E. A., "Observation of bose einstein condensation in a dilute

atomic vapor," *Science* **269**, 198 (1995).

[8] B. DeMarco and D. S. Jin, "Onset of fermi degeneracy in a trapped atomic gas," *Science* **285**, 1703 (1999).

[9] Markus Greiner, Cindy A. Regal, and Deborah S. Jin, "Emergence of a molecular boseeinstein condensate from a fermi gas," *Nature* **426**, 537 (2003).

[10] Florian Schreck (Private communication) .

[11] Umakant D. Rapol, Ajay Wasan, and Vasant Natarajan, "Loading of a rb magneto-optic trap from a getter source," *Phys. Rev. A* **64**, 023402 (2001).

[12] B. P. Anderson and M. A. Kasevich, "Loading a vapor-cell magneto-optic trap using light-induced atom desorption," *Phys. Rev. A* **63**, 023404 (2001).

[13] J. Prodan, W. Phillips, and H. Metcalf, "Laser production of a very slow monoenergetic atomic beam," *Phys. Rev. Lett.* **49**, 1149 (1982).

[14] J. Prodan and W. Phillips, "Chirping the light fantastic: Recent nbs atomic cooling experiments," *Prog. Quant. Elect.* **8**, 231 (1984).

[15] R. Gaggl, L. Windholz, C. Umfer, and C. Neureiter, "Laser cooling of a sodium atomic beam using the stark effect," *Phys. Rev. A* **49**, 1119 (1994).

[16] J. Dalibard and C. Cohen-Tannoudji, "Laser cooling below the doppler limit by polarization gradients: simple theoretical models," *J. Opt. Soc. Am. B* **6**, 2020 (1989).

[17] Mark Kasevich and Steven Chu, "Laser cooling below a photon recoil with three-level atoms," *Phys. Rev. Lett.* **69**, 1741 (1992).

[18] J. Lawall, S. Kulin, B. Saubamea, N. Bigelow, M. Leduc, and C. Cohen Tannoudji, "Laser cooling below a photon recoil with three-level atoms," *Phys. Rev. Lett.* **75**, 4194 (1995).

[19] H. Mabuchi, Q. A. Turchette, M. S. Chapman, and H. J. Kimble, "Real-time detection of individual atoms falling through a high-finesse optical cavity," *Opt. Lett.* **21**, 1393 (1996).

[20] Braulio Gutiérrez-Medina, *Quantum Transport and Control of Atomic Motion with Light*, Ph.D. thesis, The University of Texas at Austin (2004).

[21] Kevin Henderson, *Experiments with a Bose-Einstein Condensate in a Quasi-1D Magnetic Waveguide*, Ph.D. thesis, The University of Texas at Austin (2006).

[22] Mark Raizen, Qian Niu, and Christophe Salomon, "New light on quantum transport," *Physics Today* **50**, 30 (1997).

[23] M. Ben Dahan, E. Peik, J. Reichel, Y. Castin, and C. Salomon, "Bloch oscillations of atoms in an optical potential," *Phys. Rev. Lett.* **76**, 4508 (1996).

[24] S. R. Wilkinson, C. F. Bharucha, K. W. Madison, Q. Niu, and M. G. Raizen, "Observation of atomic wannier-stark ladders in an accelerating optical potential," *Phys. Rev. Lett.* **76**, 4512 (1996).

[25] Milton Abramowitz and eds Irene A. Stegun, *Handbook of Mathematical Functions: with Formulas, Graphs, and Mathematical Tables* (Dover, New York, 1965).

[26] M.-O. Mewes, M.R. Andrews, N.J. van Druten, D.M. Kurn, D.S. Durfee, and W. Ketterle, "Bose einstein condensation in a tightly confining dc magnetic trap," *Phys. Rev. Lett.* **77**, 416 (1996).

[27] M.-O. Mewes, M.R. Andrews, N.J. van Druten, D.M. Kurn, D.S. Durfee, and W. Ketterle, "Nonlinear self-trapping of matter waves in periodic potentials," *Phys. Rev. Lett.* **94**, 020403 (2005).

[28] F. G. Casati and Eds J. Ford, *Stochastic Behavior in Classical and Quantum Hamiltonian Systems. Lecture Notes in Physics Vol. 93* (Springer Verlag, Berlin, 1979).

[29] F.L. Moore, J.C. Robinson, C.F. Bharucha, B. Sundaram, and M.G. Raizen, "An atom optics realization of the quantum delta-kicked rotor," *Phys. Rev. Lett.* **75**, 4598 (1995).

[30] B.G. Klappauf, W.H. Oskay, D.A. Steck, and M.G. Raizen, "Observation of noise and dissipation effects on dynamical localization," *Phys. Rev. Lett.* **81**, 1203 (1998).

[31] Cyrus F. Bharucha, *Experiments In Dynamical Localization Of Ultra-Cold Sodium Atoms Using Time-Dependent Optical Potentials*, Ph.D. thesis, The University of Texas at Austin (1997).

[32] Daniel A. Steck, *Quantum Chaos, Transport, And Decoherence In Atom Optics*, Ph.D. thesis, The University of Texas at Austin (2001).

[33] F.L Moore, J.C. Robinson, C. Bharucha, P.E. Williams, , and M.G. Raizen, "Observation of dynamical localization in atomic momentum transfer: A new testing ground for quantum chaos," *Phys. Rev. Lett.* **73**, 2974 (1994).

[34] D. R. Grempel, R. E. Prange, and Shmuel Fishman, "Quantum dynamics of a nonintegrable system," *Phys. Rev. A* **29**, 1639 (1984).

[35] B. T. H. Varcoe, S. Brattke, M. Weidinger, and H. Walther, "Preparing pure photon number states of the radiation field," *Nature* **403**, 743 (2000).

[36] P. Grangier, G. Roger, and A. Aspect, "Experimental evidence for a photon anticorrelation effect on a beam splitter: A new light on single-photon interferences," *Europhys. Lett.* **1**, 173 (2000).

[37] Philippe Tamarat Christian Brunel, Brahim Lounis and Michel Orrit, "Triggered source of single photons based on controlled single molecule fluorescence," *Phys. Rev. Lett.* **83**, 2722 (1999).

[38] Philippe Grangier, Juan Ariel Levenson, and Jean-Philippe Poizat, "Quantum non-demolition measurements in optics," *Nature* **396**, 537 (1998).

[39] Stephen R. Friberg, Susumu Machida, and Yoshihisa Yamamoto, "Quantum-nondemolition measurement of the photon number of an optical soliton," *Phys. Rev. Lett.* **69**, 3165 (1992).

[40] G. Nogues, A. Rauschenbeutel, S. Osnaghi, P. Bertet, M. Brune, J. M. Raimond, S. Haroche, L. G. Lutterbach, and L. Davidovich, "Measurement of a negative value for the wigner function of radiation," *Phys. Rev. A* **62**, 054101 (2000).

[41] A. I. Lvovsky, H. Hansen, T. Aichele, O. Benson, J. Mlynek, and S. Schiller, "Quantum state reconstruction of the single-photon fock state," *Phys. Rev. Lett.* **87**, 050402 (2001).

[42] Thomas Jennewein, Christoph Simon, Gregor Weihs, Harald Weinfurter, and Anton Zeilinger, "Quantum cryptography with entangled photons," *Phys. Rev. Lett.* **84**, 4729 (2000).

[43] D. S. Naik, C. G. Peterson, A. G. White, A. J. Berglund, and P. G. Kwiat, "Entangled state quantum cryptography: Eavesdropping on the ekert protocol," *Phys. Rev. Lett.* **84**, 4733 (2000).

[44] W. Tittel, J. Brendel, H. Zbinden, and N. Gisin, "Quantum cryptography using entangled photons in energy-time bell states," *Phys. Rev. Lett.* **84**, 4737 (2000).

[45] A.M. Dudarev, Q. Niu, and M.G. Raizen, "Quantum many-body culling: Production of a definite number of ground-state atoms in a bose-einstein condensate," *Phys. Rev. Lett.* **98**, 063001 (2007).

[46] C.-S. Chuu, F. Schreck, T.P. Meyrath, J.L. Hanssen, G.N. Price, and M.G. Raizen, "Direct observation of sub-poissonian number statistics in a degenerate bose gas," *Phys. Rev. Lett.* **59**, 260403 (2005).

[47] M. Girardeau, "Relationship between systems of impenetrable bosons and fermions in one dimension," *J. Math. Phys.* **1**, 516 (1960).

[48] A. del Campo and J. G. Muga, "Atom fock-state preparation by trap reduction," *Phys. Rev. A* **78**, 023412 (2008).

[49] John C. Robinson, *Atom Optics: A New Testing Ground For Quantum Chaos*, Ph.D. thesis, The University of Texas at Austin (1995).

[50] Artur Widera, *Design and construction of a modular Spin-Flip Zeeman slower*, Master's thesis, The University of Texas at Austin (2001).

[51] Carl Wieman, Gwenn Flowers, and Sarah Gilbert, "Inexpensive laser cooling and trapping experiment for undergraduate laboratories," *Am. J. Phys.* **63**, 317 (1995).

[52] Wolfgang Ketterle, Kendall B. Davis, Michael A. Joffe, Alex Martin, and David E. Pritchard, "High densities of cold atoms in a dark spontaneous-force optical trap," *Phys. Rev. Lett.* **70**, 2253 (1993).

[53] K.B. Davis, M.-O. Mewes, M.R. Andrews, N.J. van Druten, D.S. Durfee, D.S. Kurn, and W. Ketterle, "Bose-einstein condensation in a gas of sodium atoms," *Phys. Rev. Lett.* **75**, 3969 (1995).

[54] D. S. Naik and C. Raman, "Optically plugged quadrupole trap for bose-einstein condensates," *Phys. Rev. A* **71**, 033617 (2005).

[55] C. C. Bradley, C. A. Sackett, , and R. G. Hulet, "Bose-einstein condensation of lithium: Observation of limited condensate number," *Phys. Rev. Lett.* **78**, 985 (1997).

[56] F. Dalfovo, S. Giorgini, L. P. Pitaevskii, , and S. Stringari, "Theory of bose einstein condensation in trapped gases," *Rev. Mod. Phys.* **71**, 463 (1999).

[57] C. J. Pethick and H. Smith, *Bose Einstein condensation in dilute gases* (Cambridge University Press, Cambridge, 2002).

[58] Y. Castin and R. Dum, "Bose einstein condensates in time dependent traps," *Phys. Rev. Lett.* **77**, 5315 (1996).

[59] A. Görlitz, T. L. Gustavson, A. E. Leanhardt, R. Löw, A. P. Chikkatur, S. Gupta, S. Inouye, D. E. Pritchard, and W. Ketterle, "Sodium bose-einstein condensates in the f=2 state in a large-volume optical trap," *Phys. Rev. Lett.* **90**, 90401 (2003).

[60] T.L.Gustavson, A.P.Chikkatur, A.E.Leanhardt, A.Görlitz, S.Gupta, D.E.Pritchard, and W.Ketterle, "Transport of bose-einstein condensates with optical

tweezers," *Phys. Rev. Lett.* **88**, 020401 (2002).

[61] Belén Paredes, Artur Widera, Valentin Murg, Olaf Mandel, Simon Fölling, Ignacio Cirac, Gora V. Shlyapnikov, Theodor W. Hnsch, and Immanuel Bloch, "Tonksgirardeau gas of ultracold atoms in an optical lattice," *Nature* **429**, 277 (2004).

[62] Toshiya Kinoshita, Trevor Wenger, and David S. Weiss, "Observation of a one-dimensional tonks-girardeau gas," *Science* **305**, 5687 (2004).

[63] T. P. Meyrath, F. Schreck, J. L. Hanssen, C.-S. Chuu, and M. G. Raizen, "Bose-einstein condensate in a box," *Phys. Rev. A* **71**, 041604(R) (2005).

[64] Z. Hu and H. J. Kimble, "Observation of a single atom in a magneto-optical trap," *Opt. Lett.* **19**, 1888 (1994).

[65] Mark G. Raizen, Shou-Pu Wan, Chuanwei Zhang, and Qian Niu, "Ultra-high fidelity qubits for quantum computing," *Submitted for publication, arXiv:0906.2114* (2008).

[66] Karl D. Nelson, Xiao Li, and David S. Weiss, "Imaging single atoms in a three-dimensional array," *Nature Phys.* **3**, 556 (2007).

[67] R. A.Williams, J. D. Pillet, S. Al-Assam, B. Fletcher, M. Shotter, and C. J. Foot, "Dynamic optical lattices: two-dimensional rotating and accordion lattices for ultracold atoms," *Optics Express* **16**, 16977 (2008).

[68] J.C. Robinson, C. Bharucha, F.L. Moore, R. Jahnke, G.A. Georgakis, Q. Niu, B. Sundaram, and M.G. Raizen, "Study of quantum dynamics in

the transition from classical stability to chaos," *Phys. Rev. Lett.* **74**, 3963 (1995).

[69] R. Diener, Q. Niu, and M.G. Raizen, "Quantum tweezer for atoms," *Phys. Rev. Lett.* **89**, 070401 (2002).

[70] A. Migdall, J. Prodan, W. Phillips, T. Bergeman, and H. Metcalf, "First observation of magnetically trapped neutral atoms," *Phys. Rev. Lett.* **54**, 2596 (1985).